Assessment of Pumped Heat Electricity Storage Systems through Exergoeconomic Analyses

Bewertung von Strom-Wärme-Strom Speichersystemen mittels exergoökonomischer Analysen

Vom Fachbereich Maschinenbau der Technischen Universität Darmstadt
zur Erlangung des akademischen Grades Doktor-Ingenieur (Dr.-Ing.)
genehmigte Dissertation von M.Sc. Axel Dietrich aus Berlin
Tag der Einreichung: 6. Juni 2017, Tag der Prüfung: 21. August 2017
Darmstadt 2017 — D 17

1. Gutachten: Prof. Dr.-Ing. Peter Stephan
2. Gutachten: Prof. Dr. rer. nat. habil. André Thess

TECHNISCHE
UNIVERSITÄT
DARMSTADT

TTD
Technische Thermodynamik

Assessment of Pumped Heat Electricity Storage Systems through Exergoeconomic Analyses
Bewertung von Strom-Wärme-Strom Speichersystemen mittels exergoökonomischer Analysen

Genehmigte Dissertation von M.Sc. Axel Dietrich aus Berlin

1. Gutachten: Prof. Dr.-Ing. Peter Stephan
2. Gutachten: Prof. Dr. rer. nat. habil. André Thess

Tag der Einreichung: 6. Juni 2017
Tag der Prüfung: 21. August 2017

Darmstadt 2017 — D 17

Bitte zitieren Sie dieses Dokument als:
URN: urn:nbn:de:tuda-tuprints-67520
URL: http://tuprints.ulb.tu-darmstadt.de/6752

Dieses Dokument wird bereitgestellt von tuprints,
E-Publishing-Service der TU Darmstadt
http://tuprints.ulb.tu-darmstadt.de
tuprints@ulb.tu-darmstadt.de

This publication is available at the following Creative Commons license:
Attribution – Non-commercial – No-derivatives 4.0 International
http://creativecommons.org/licenses/by-nc-nd/4.0/

Erklärung zur Dissertation

Hiermit versichere ich, die vorliegende Dissertation ohne Hilfe Dritter nur mit den angegebenen Quellen und Hilfsmitteln angefertigt zu haben. Alle Stellen, die aus Quellen entnommen wurden, sind als solche kenntlich gemacht. Diese Arbeit hat in gleicher oder ähnlicher Form noch keiner Prüfungsbehörde vorgelegen.

Darmstadt, den 6. Juni 2017

Axel Dietrich

Vorwort

Diese Arbeit entstand während meiner Zeit als wissenschaftlicher Mitarbeiter des Instituts für Technische Thermodynamik (TTD) an der TU Darmstadt. Dem Institutsleiter Prof. Dr.-Ing. Peter Stephan danke ich für das mir entgegengebrachte Vertrauen, die inhaltlichen Freiräume, die ich während der Bearbeitung dieser Arbeit genießen konnte, und die hervorragenden Arbeitsbedingungen am Institut. Außerdem bin ich Herrn Stephan dankbar für den hohen Stellenwert, den er der Lehre beigemessen hat, einem Arbeitsinhalt, der auch mir sehr wichtig war.

Prof. Dr. rer. nat. habil. André Thess danke ich für die Übernahme des Koreferats und für die Begeisterung, die er für das Thema dieser Arbeit aufbringt. Vor dem Hintergrund seiner Verpflichtungen als Professor für Energiespeicherung an der Universität Stuttgart und Direktor des Instituts für Technische Thermodynamik am Deutschen Zentrum für Luft- und Raumfahrt ist beides keine Selbstverständlichkeit.

Bei Frank Dammel, dem akademischen Direktor des TTD, möchte ich mich für die sehr gute Betreuung dieser Arbeit kombiniert mit der Schaffung breiter inhaltlicher Freiräume bedanken. Er war stets ein kompetenter Ansprechpartner und hat mich ermutigt, auch Themen abseits vom geraden Weg zum Ziel zu bearbeiten.

Meinen Kolleginnen und Kollegen, insbesondere denen, die mich auch freundschaftlich begleitet haben, danke ich für die tolle Arbeitszeit, die motivierende Arbeitsatmosphäre und die große Hilfsbereitschaft, die mir entgegengebracht wurde. Durch dieses Kollegium habe ich die Zeit am TTD sehr genießen können.

Durch die stetigen Motivationen und die außerordentlich gründliche sowie zeitlich sehr flexible Korrektur meiner Ausarbeitung haben Christiane Schlawitschek, Jochen Dietl und Valerie Bensch großen Anteil am Gelingen dieser Arbeit und ihrer finalen Erscheinungsform. Für diese Hilfe bin ich sehr dankbar.

Meiner Abschlussarbeiterin und allen meinen Abschlussarbeitern bin ich dankbar für die fachlichen und fachfremden Erkenntnisse, die ich durch das Betreuen ihrer Arbeiten gewinnen konnte. Wegen der inhaltlichen Nähe zu dieser Arbeit danke ich besonders Orkan Akpinar, Christoph Fraunholz, Michele Profumo und Jella Winterling für ihre fundierten Beiträge.

Hans-Peter Wolf und dem gesamten EBSILON®*Professional*-Team aus Zwingenberg danke ich für die schnelle, kompetente und sehr freundliche Bearbeitung all meiner Anfragen sowie die Bereitstellung von Lizenzen für studentische Arbeiten.

Der Fritz und Margot Faudi-Stiftung sowie der Darmstädter Exzellenz-Graduiertenschule für Energiewissenschaft und Energietechnik (GSC 1070, Teil der Exzellenzinitiative der Deutschen Forschungsgemeinschaft) danke ich für die finanzielle Unterstützung dieser Arbeit.

Bei meiner Familie, ganz besonders bei meinen Eltern, möchte ich mich für die Unterstützung bedanken, die ich von ihnen in allen Lebenslagen erfahren durfte. Sie haben mir den Weg geebnet, den ich ohne diese Unterstützung nicht bis zur Promotion hätte beschreiten können.

Abstract

Within the last 25 years, the share of renewable energy sources in German electrical energy production has been rising considerably and is expected to increase further in the coming years. The volatility of renewable energy sources results in an increasing mismatch between supply and demand of electrical energy, creating the need for storage capacities. The storage of electrical energy in the form of thermal energy can be realized by Pumped Heat Electricity Storage (PHES) systems, a location-independent alternative to established storage technologies. Detailed analyses, considering the transient operation of PHES systems based on commercially available or state-of-the-art technology, are currently not publicly accessible.

In this work, numerical models that enable a transient simulation of PHES systems are created using the process simulation software EBSILON®*Professional*. For that purpose, numerical models of packed bed sensible heat TES systems as well as latent heat TES systems are developed and validated. While the model of the packed bed sensible heat TES systems is based on modifications of a built-in component, the model of the latent heat TES systems was independently modeled and implemented as supplementary component.

For the analysis of PHES systems, a characteristic operation scenario is deduced from the European market for electrical energy. Based on the day-ahead market for Germany and Austria, which shows a high predictability regarding daily electricity price distributions, the PHES systems accomplish a complete charging, storage and discharging

Kurzzusammenfassung

In den letzten 25 Jahren ist der Anteil erneuerbarer Energiequellen an der Erzeugung elektrischer Energie stark angestiegen und es ist zu erwarten, dass diese Entwicklung in den nächsten Jahren weiter anhält. Die Volatilität der erneuerbaren Energiequellen führt verstärkt zu einem Ungleichgewicht zwischen Angebot und Nachfrage von elektrischer Energie, was in einen steigenden Bedarf an Speicherkapazitäten mündet. Zur Speicherung elektrischer Energie in Form von thermischer Energie können Strom-Wärme-Strom (SWS) Systeme, eine ortsungebundene Alternative zu etablierten Speichertechnologien, eingesetzt werden. Detaillierte Analysen, die das transiente Betriebsverhalten von SWS Systemen bestehend aus kommerziell verfügbaren oder dem Stand der Technik entsprechenden Komponenten berücksichtigen, sind gegenwärtig nicht öffentlich verfügbar.

In der vorliegenden Arbeit werden numerische Modelle zur transienten Berechnung von SWS Systemen basierend auf der Prozesssimulationssoftware EBSILON®*Professional* erstellt. Dafür werden Modelle zur Simulation von sensiblen thermischen Energiespeichern für Schüttgüter und latenten thermischen Energiespeichern entwickelt und validiert. Während das Modell des sensiblen thermischen Energiespeichers für Schüttgüter auf Modifikationen einer existierenden Standardkomponente beruht, wurde das Modell des latenten thermischen Energiespeichers unabhängig modelliert und als Zusatzkomponente implementiert.

Zur Analyse von SWS Systemen wird ein charakteristisches Einsatzszenario vom Europäischen Energiemarkt abgeleitet. Basierend auf dem Day-Ahead Markt für Deutschland und Österreich, der sich durch eine hohe Vorhersagbarkeit der tageszeitlichen Preisverteilung auszeichnet, absolvieren die SWS Systeme einen kompletten Belade-, Speicher- und Entladezyklus pro Tag. Für einen möglichst wirtschaftlichen

period per day. For a high economic feasibility, an electrical input power in the order of 10 MW is combined with charging and discharging durations of 4 h.

PHES systems based on Joule and Rankine cycles are designed, focusing on commercially available and state-of-the-art technology. Design parameters are optimized in order to reach high round-trip efficiencies. Employing the models developed in this work, the transient operation of the PHES systems is simulated in accordance with the characteristic operation scenario. A detailed exergoeconomic analysis, which combines an exergy and an economic analysis, is conducted for the PHES systems based on Joule cycles. A simplified sensitivity analysis is employed to evaluate the influence of uncertainties in economic input parameters on the results.

Depending on design parameters, the analyzed PHES systems reach round-trip efficiencies between 36 % and 43 %. Having lower efficiencies than established storage technologies, PHES systems have the advantage of being location independent. The exergoeconomic analysis reveals that an economic operation of PHES systems is currently not possible. This, however, is at least partly caused by the conditions at the German market for electrical energy, which are unfavorable for the operation of electrical energy storage systems.

In summary, the PHES systems designed and the numerical models developed in this work enable the exergoeconomic analysis and assessment of these electrical energy storage systems, based on available technology and a realistic operation scenario.

Betrieb werden Beladeleistungen in der Größenordnung von 10 MW mit Be- und Entladezeiten von 4 h kombiniert.

Aufbauend auf Joule und Rankine Prozessen werden SWS Systeme bestehend aus kommerziell verfügbaren oder dem Stand der Technik entsprechenden Komponenten konzipiert. Außerdem werden Design-Parameter optimiert, um hohe Strom-zu-Strom Gesamtwirkungsgrade zu erzielen. Unter Verwendung der im Zuge dieser Arbeit entwickelten Modelle wird der transiente Betrieb entsprechend der charakteristischen Einsatzszenarien simuliert. Eine detaillierte exergoökonomische Analyse, die Kombination aus exergetischer und ökonomischer Analyse, wird für die auf Joule Prozessen aufbauenden SWS Systeme durchgeführt. Mit einer vereinfachten Sensitivitätsanalyse wird der Einfluss der ökonomischen Eingangsparameter auf die Ergebnisse abgeschätzt.

Abhängig von Design-Parametern erzielen die analysierten SWS Systeme Strom-zu-Strom Gesamtwirkungsgrade zwischen 36 % und 43 %. Bei geringeren Wirkungsgraden als etablierte Speichertechnologien haben SWS Systeme den Vorteil der lokalen Unabhängigkeit. Die exergoökonomische Analyse zeigt, dass ein wirtschaftlicher Betrieb von SWS Systemen derzeit nicht möglich ist. Dies liegt jedoch zumindest teilweise an den derzeitigen Bedingungen am Deutschen Energiemarkt, welche keine guten Voraussetzungen für den Betrieb von elektrischen Energiespeichern schaffen.

Die im Zuge dieser Arbeit konzipierten SWS Systeme und entwickelten numerischen Modelle erlauben die exergoökonomische Analyse und Bewertung dieser Speichersysteme. Dabei wurden insbesondere verfügbare Technologien und ein realistisches Einsatzszenario berücksichtigt.

Contents

Nomenclature

Latin letters	Unit	Description
A	m^2	Area
A	*miscellaneous*	Capacity/size parameter for costing
C	€	Costs
$CEPCI$	-	Chemical Engineering Plant Cost Index
c	$€\,J^{-1}$	Exergy-specific costs
c	$J\,(kg\,K)^{-1}$	Mass-specific heat capacity
d	m	Diameter
E	J	Exergy
En	J	Energy
e	$J\,(kg)^{-1}$	Mass-specific exergy
en	$J\,(kg)^{-1}$	Mass-specific energy
f	-	Form factor for Nusselt number of packed bed
g	-	Geometry factor for increased PCM thermal conductivity
h	$J\,(kg)^{-1}$	Mass-specific enthalpy
Δh_f	$J\,(kg)^{-1}$	Mass-specific enthalpy of fusion
Δh_v	$J\,(kg)^{-1}$	Mass-specific enthalpy of vaporization
i	-	Interest rate
K	-	Fitting parameter for costing
K	-	Scaling exponent for costing
k	-	Absolute roughness
l	m	Length, longitudinal position
M	kg	Mass
N^{an}	-	Number of operation periods per year
n	-	Time step counter
n^{an}	a	Projected operating time
P	W	Power
p	Pa	Pressure
p	-	Iteration loop counter
Q	J	Heat
R	$K\,W^{-1}$	Thermal resistance
r	m	Radius, radial position
$r_{€\$}$	$€\,\$^{-1}$	Euro-Dollar exchange rate
s	$J\,(kg\,K)^{-1}$	Mass-specific entropy
T	°C	Temperature
$\Delta T_{out,max}$	°C	TES maximum outlet temperature difference
u	$m\,s^{-1}$	Velocity
V	m^3	Volume
X	-	Steam quality

Latin letters	Unit	Description
Z^{an}	€	Component costs per year
Z^{OP}	€	Component costs per operation period
Z^{PEC}	€	Purchased equipment costs

Greek letters	Unit	Description
α	$\mathrm{W\,(m^2\,K)^{-1}}$	Convective heat transfer coefficient
γ	-	Annual operation and maintenance cost factor
ϵ	-	Volume-specific void fraction of a packed bed
η	-	Efficiency
θ	-	Parameter specifying an intermediate time step
λ	$\mathrm{W\,(m\,K)^{-1}}$	Thermal conductivity
ν	$\mathrm{m^2\,s^{-1}}$	Kinematic viscosity
ξ_p	-	Drag coefficient
Π	-	Pressure ratio
ρ	$\mathrm{kg\,m^{-3}}$	Density
τ	s	Time
ω	-	Relaxation factor

Characteristic numbers	Definition	Description
Bi	$\alpha\, r\, \lambda^{-1}$	Biot number
Nu	$\alpha\, l\, \lambda^{-1}$	Nusselt number
Pr	$\nu\, \rho\, c\, \lambda^{-1}$	Prandtl number
Re	$u\, d\, \nu^{-1}$	Reynolds number
St	$c\, \Delta T\, h_{\mathrm{PC}}^{-1}$	Stefan number

Subscripts	Description
amb	Ambient
C	Component
ch	Chemical
D	Destruction
eff	Effective
el	Electrical
en	Energetic
ex	Exergetic
F	Fuel
fluid	Working fluid
free	Undisturbed free stream
i	Inner
in	Inlet
init	Initial
kin	Kinetic

Subscripts	Description
L	Loss
l	Liquid
M	Model of thermal energy storage module
max	Maximal, maximum
mech	Mechanical
min	Minimal, minimum
N	Nominal
o	Outer
out	Outlet
P	Product
Pa	Particle
pot	Potential
phy	Physical
R	Real thermal energy storage module
ref	At reference conditions
s	Solid
sys	System
th	Thermal
v	Vapor

Superscripts	Description
OP	Operation period
PEC	Purchased equipment costs

Abbreviations	Description
C	Compressor
CAES	Compressed air energy storage
DLL	Dynamic link library
DLR	German Aerospace Center (Deutsches Zentrum für Luft- und Raumfahrt)
EEG	Act on the Development of Renewable Energy Sources (Gesetz für den Ausbau Erneuerbarer Energien)
EEX	European Energy Exchange
EPEX Spot	European Power Exchange
G	Generator
GWP	Global warming potential
HE	Heat engine
HP	Heat pump
HT	High temperature
JH	Joule/resistive heating
LT	Low temperature
M	Motor
ODP	Ozone depletion potential

Abbreviations	Description
ORC	Organic Rankine cycle
OTC	Over-the-counter
PC	Phase change
PCM	Phase change material
PHES	Pumped heat electricity storage
PEC	Purchased equipment costs
SOR	Successive overrelaxation
T	Turbine
TES	Thermal energy storage

1 Introduction

Within the last 25 years, the share of renewable energy sources in the German gross electrical energy production has been rising up to 30 % in 2015 [1]. Based on the trend shown in Figure 1.1, higher shares of renewable energy sources can be expected in the future. Adopted in July 2016, the newest version of the *Act on the Development of Renewable Energy Sources* (*Gesetz für den Ausbau Erneuerbarer Energien, EEG 2016*) targets to rise the share of renewable energy sources in gross electrical energy consumption to 40 % in 2025, 55 % in 2035, and 80 % in 2050 [20, § 1]. The higher the share of renewables, the stronger is the impact of the volatility of renewable energy sources on the production of electrical energy. More and more frequently, this results in a mismatch between the electrical energy supply and its demand. To maintain stability in the grid, supply and demand of electrical energy have to be balanced, because the grid itself cannot store electrical energy. Up to a certain degree, balancing of supply and demand can be achieved by flexible operation of power plants and load balancing. However, to reach the targets of the *EEG 2016*, medium to large scale storage systems for electrical energy are required.

Electrochemical accumulators have limitations in cyclic stability and require relatively large amounts of rare elements, which complicates their application as large scale storage for electrical energy. Non-chemical storage systems such as pumped hydro storage and compressed air energy storage can provide sufficient storage capacity but require special geological and geographical conditions [139] which limits their application as large scale storage for electrical energy. A location-independent alternative is the relatively new technology known as pumped heat electricity storage (PHES) systems which stores electrical energy via the detour of thermal energy in thermal energy storage (TES) systems.

Referring to the most common setup (Figure 1.2) PHES systems consist of the four subsystems heat pump, heat engine, high temperature TES, and low temperature TES. Usually, the high and low temper-

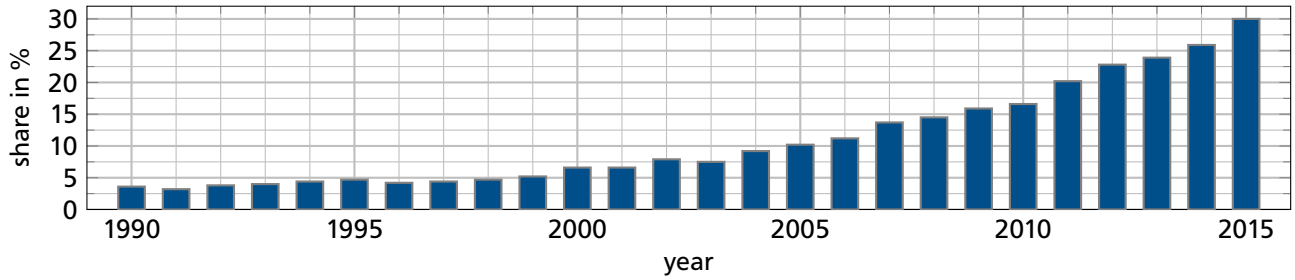

Figure 1.1: Share of renewable energy sources in the German gross electrical energy production (data by [1]).

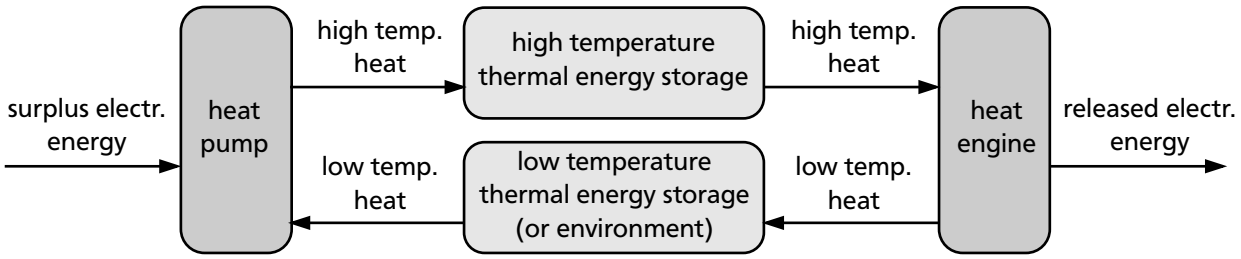

Figure 1.2: Common setup of a PHES system (boxes), including energy flows (arrows).

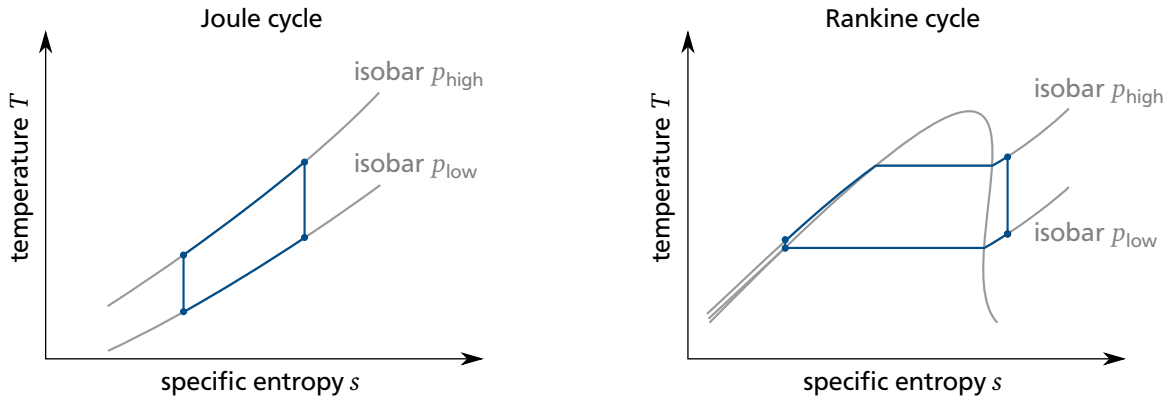

Figure 1.3: T,s-diagrams depicting the ideal changes of state of Joule and Rankine cycles.

ature TES systems are each composed of but not limited to a single storage module. Simple setups do not contain a low temperature TES, the environment is employed as heat sink and heat source instead.

PHES systems can be operated to stabilize the electrical grid by acting either as consumer or as supplier. In times of high supply and low demand the heat pump uses surplus electrical energy to pump heat taken from a low temperature TES (or from the environment) to a higher temperature level. This high temperature heat is forwarded to the high temperature TES, where it is stored as thermal energy until the demand for electrical energy exceeds its supply. At those times the TES supplies heat to the heat engine which converts the thermal energy back into electrical energy. The low temperature heat released by the heat engine is absorbed by the low temperature TES (or by the environment).

An important performance indicator of PHES systems is their round-trip efficiency, which describes the ratio of electrical energy supplied to the grid during heat engine operation (discharging) to electrical energy received from the grid during heat pump operation (charging). To evaluate the energy conversion within the PHES system and its subsystems with respect to the thermodynamic optimum, an exergy analysis is applied. To further consider the economic constraints of energy conversion, an exergoeconomic analysis is performed.

Heat pump, heat engine and TES systems can be based on various technologies. In the current work, Rankine and Joule cycles are considered for the heat pump and the heat engine. Being also known as Brayton cycle, the term Joule cycle is employed in this work. For both types of thermodynamic cycles, the ideal changes of state consist of two isentropic compression and expansion processes that connect two isobaric heat transfers at different pressure levels. As major difference, Joule cycles are based on gases as working fluids, whereas Rankine cycles are based on two-phase mixtures of liquid and vapor (Figure 1.3). Consequently, Joule cycles transfer heat at varying temperature, which favors a combination with sensible heat TES systems. Rankine cycles favor a combination with latent heat TES systems due to the liquid-vapor phase change of the working fluid, which results in a heat transfer at constant temperature.

In this work, numerical models for a transient simulation of PHES systems are developed and applied to the exergoeconomic analysis of PHES systems based on Joule and Rankine cycles. Chapter 2 summarizes the state of the art of PHES systems, from which the research questions and the objectives of this work are deduced and presented in Chapter 3. The modeling of PHES systems and their analysis method is introduced in Chapter 4, supplemented with preliminary considerations for the exergoeconomic analysis in Chapter 5. Chapters 6 and 7 are devoted to the design as well as the analysis of PHES systems based on Joule and Rankine cycles, respectively. Finally, Chapter 8 provides a summary and outlook of this work.

2 State of the Art

A literature review on the storage of electrical energy in general as well as pumped heat electricity storage systems and thermal energy storage systems in detail is presented in this chapter. Research gaps are identified, from which the research questions and objectives of this work are deduced and summarized in the following chapter.

2.1 Storage of electrical energy - current technology and research activities

To store electrical energy, different technologies are commercially available. Relating storage capacity and start up time to full load, an overview of the different technologies is depicted in Figure 2.1. Electrochemical capacitors, superconducting magnetic energy storage systems, and flywheels provide short start up times but have only small storage capacities. Pumped hydro storage systems and compressed air energy storage systems have longer start up times but provide large storage capacities. Electrochemical accumulators take an intermediate position.[102, Chapter 3.1]

Electrical energy storage systems with small capacities and small start up times can be used to enhance the quality of the electrical energy grid by damping small fluctuations in frequency and voltage. Because this application is not the objective of the present work the corresponding storage technologies are not considered further. By introducing a mismatch between supply and demand of electrical energy in the electrical grid, high shares of renewable energy sources compromise grid stability. To secure grid stability along the ambitioned development targets of the *EEG 2016* [20, § 1], medium to high capacity storage systems for electrical energy are required. Presently, the only commercially available high capacity storage technologies for electrical energy are pumped hydro storage systems and compressed air energy storage systems.

Pumped hydro storage systems use electrical energy to pump water from a low elevation basin to a high elevation basin during charge. During discharge the water from the high elevation basin flows back into the low elevation basin, powering a turbine-generator set that generates electrical energy.

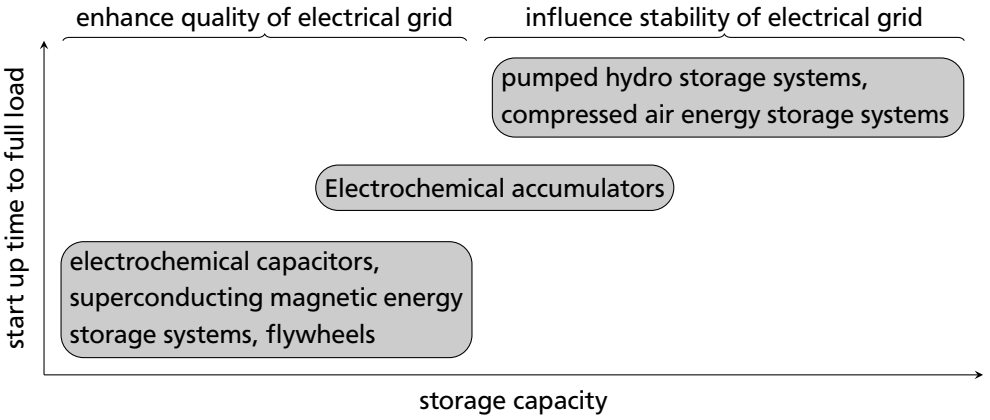

Figure 2.1: Overview of commercially available technology to store electrical energy in relation to capacity and start up time (data by [102, Chapter 3.1]).

Table 2.1: Overview of terminologies used in literature for pumped heat electricity storage (PHES).

terminology	reference
compressed heat energy storage (CHEST)	[132]
electrothermal energy storage	[89]
pumped heat electricity storage	[55; 104; 139]
pumped thermal electricity storage	[87; 132]
thermo-electric energy storage	[65; 96]
thermo-electrical energy storage	[93–95]

Consequently, electrical energy is stored in the form of potential energy which results in negligible self-discharge and almost unlimited storage durations. At specific investment costs between 470 € $(kW)^{-1}$ and 2170 € $(kW)^{-1}$, the round-trip efficiencies reach high values of 70 % to 80 % [18; 102, Chapter 2.4.2]. In contrast, pumped hydro storage systems demand for suitable topological conditions and seal large areas with their basins [102, Chapter 2.4.2]. For Germany, the development potential for new pumped hydro storage systems is very small [102, Chapter 2.4.2].

Compressed air energy storage (CAES) systems use electrical energy to power high temperature air compressors. For safety reasons the compressed hot air is cooled before being stored in an underground cavern. During discharge, the compressed air is heated by natural gas combustion before expanding in turbine-generator sets that generate electrical energy. Heating the compressed air is necessary to prevent the turbines from freezing. Two CAES systems are currently in operation. The system in Huntorf (Germany) has a storage output capacity of 580 MWh_{el} [102, Chapter 2.4.1] and reaches a round-trip efficiency of 46 % [41]. Due to internal heat recovery during discharge, the system in McIntosh (USA) reaches a round-trip efficiency of 54 % [41] having a storage output capacity of 2860 MWh_{el} [102, Chapter 2.4.1].

Adiabatic CAES systems are subject to current research. These systems employ a thermal energy storage to store the heat released by the compressed air before entering the underground cavern. During discharge, the stored heat is transferred back to the compressed air before entering the turbine. Consequently, adiabatic CAES do not combust natural gas. Due to similarities in working principle and required components to the storage technology examined in this work, the state of the art of adiabatic CAES systems is presented in detail in Chapter 2.3. As all CAES systems require consolidated underground caverns of several hundred thousand cubic meters, installation sites and storage capacities are limited.

An alternative and relatively new technology are pumped heat electricity storage (PHES) systems, which store electrical energy via the detour of thermal energy in thermal energy storage (TES) systems. A brief description of the working principle is given in Chapter 1. Consequently, pumped heat electricity storage systems are not reliant on special topological or geological constraints. While several different terminologies are used for this storage technology in literature (Table 2.1), the term pumped heat electricity storage (PHES) will be employed in this work. Until now, PHES systems have not been installed to support supply and demand in the electrical energy grid. The state of the art related to the development and analysis of PHES systems is presented in the following section.

2.2 Pumped heat electricity storage systems

The first concept of storing electrical energy via the detour of thermal energy dates back to as early as 1924. Marguerre [82] introduced a system consisting of two TESs filled with wet steam. During the

discharging operation, steam flows from the high pressure, high temperature TES to the low pressure, low temperature TES powering a turbine-generator-set. During the charging operation, a motor driven compressor conveys steam from the low pressure, low temperature TES back to the high pressure, high temperature TES. Fully charged, the high and low pressure TESs reach maximum temperatures of 170 °C and 70 °C, respectively. The maximum temperature change during discharge operation amounts to 30 °C for the high pressure and 15 °C for the low pressure TES. Additional performance measures are summarized in Table 2.3. Marguerre stated that all components required for building the storage system are commercially available. Additionally, he presented a calculation indicating that the proposed storage system delivers electrical energy more economically than peak load power plants or battery storage systems. Marguerre patented this storage concept as well as several modifications [83; 84].

An analytical approach to evaluate the round-trip efficiency of PHES systems was presented by Thess [139]. Thess focused on systems that either have a high temperature or a low temperature TES in combination with the environment as second TES. Based on the framework of finite-time thermodynamics, the PHES systems were modeled as ideal Carnot cycles subject to heat transfer across finite temperature differences as only irreversibility. The relation of heat transfer coefficients between heat engine and storage, as well as between heat engine and environment, was chosen in a way which maximizes the power of the heat engine. The relation of heat transfer coefficients between heat pump and storage, as well as between heat pump and environment, was chosen in a way which maximizes the overall PHES round-trip efficiency. Under these simplifications, Thess derived the PHES round-trip efficiency as a function of storage temperature and environmental temperature only. The round-trip efficiency increases with increasing storage temperature.Thess pointed out that more detailed energetic and economic analyses are necessary to assess PHES concepts.

Steinmann [133] presented an extensive review of concepts for bulk energy storage. Basic concepts as well as current developments of PHES systems and related technology are summarized.

In the following sections, theoretical and experimental studies on PHES systems are introduced, divided into Joule and Rankine cycle based concepts. For an overview, the introduced concepts based on Joule cycles are listed in Table 2.2, the introduced concepts based on Rankine and Rankine related cycles are listed in Table 2.3. Subsequently, the state of the art of heat pump and heat engine technology is presented, focusing on technology that has the potential of being employed in PHES systems.

2.2.1 Joule cycle based PHES concepts

The research group around Desrues and Ruer [19], mainly associated with SAIPEM-SA, a company being active in the oil-producing industry as equipment manufacturer, installer, and operator, is working on PHES systems. They presented a PHES concept consisting of two TESs being connected by two compressor-turbine-pairs using argon as working fluid [19]. The high and low temperature TESs contain refractory material, similar to conventional regenerators, and reach maximum and minimum temperatures of 1000 °C and −70 °C, respectively. The PHES system comprises two additional heat exchangers, which can be used to add electrically generated heat or release heat to the environment. Releasing heat and entropy to the environment is necessary to enable a cyclic steady-state operation. The responsible heat exchanger is not placed at the coldest position in the circle, but at a position which enables a temperature driven heat release to the environment. After verifying that the spatial temperature distribution normal to the flow direction of the working fluid is homogeneous in each TES, they derived a transient model of the PHES system. The model is based on a one-dimensional finite volume approach being implemented in Matlab and compiled C-code. In the cyclic steady state, the system reaches a round-trip efficiency of 66.7 % providing 600 MWh electrical energy output based on charging and discharging

Table 2.2: Overview of research activities in the field of PHES systems based on Joule cycles.

group (company), references, year	working fluid	thermal energy storage	additional information, system and analysis shortcomings
Desrues, Ruer et al. (SAIPEM-SA), [19; 118], 2010	argon	two sensible TESs, refractory material (solid media), $T_{\max} = 1000\,^{\circ}\mathrm{C}$, $T_{\min} = -70\,^{\circ}\mathrm{C}$	simulation with Matlab and compiled C-code, compressor pressure ratio approximately 2, $E_{\mathrm{el,out}} = 600\,\mathrm{MWh}$, $E_{\mathrm{el,in}} = 900\,\mathrm{MWh}$, round-trip efficiency 66.7 %, compressors and TES systems for high storage temperatures commercially not available
Ni, Caram, [104], 2015	argon	usage of configuration presented by Desrues and Ruer	transient simulation described with exponential matrix solution techniques, compressor pressure ratio considered between 2 and 5, round-trip efficiency between 60 % and 100 %, depending on chosen parameters, components for high storage temperatures are commercially not available
Howes (Isentropic), [55–57], 2012	prototype: air, large scale machine: argon	two sensible packed bed TESs: particulate granite, $T_{\max} = 500\,^{\circ}\mathrm{C}$, $T_{\min} = -166\,^{\circ}\mathrm{C}$	only performance extrapolation for hypothetical machine presented, $P = 2\,\mathrm{MW}$, $COP = 2.19$, round-trip efficiency 72 %, high efficiencies of the envisioned reciprocating compressor and expander are currently not state-of-the-art
McTigue et al., [87], 2015	argon (utilization of large scale machine invented by Howes)	two sensible packed bed TESs: $T_{\max} = 500\,^{\circ}\mathrm{C}$, $T_{\min} = -166\,^{\circ}\mathrm{C}$	simulation in quasi-steady-state, optimization based on stochastic algorithms, round-trip efficiency between 50 % and 70 %, depending on the compression and expansion efficiencies
White et al., [154], 2013	argon (utilization of PHES concepts invented by Howes and Desrues)	utilization of storage concepts invented by Howes and Desrues	simplified analytical analysis omitting transient effects in order to identify trends of efficiencies and losses, round-trip efficiencies up to 90 %
Morandin et al., [93], 2011	air	two pairs of direct TESs for sensible heat storage: molten salt ($350\,^{\circ}\mathrm{C} < T < 700\,^{\circ}\mathrm{C}$) and synthetic oil ($100\,^{\circ}\mathrm{C} < 250\,^{\circ}\mathrm{C}$)	preliminary performance estimation yields round-trip efficiency of 55 %, high isentropic turbomachinery efficiency of 0.9 assumed

times of 6 h. However, TES systems and especially compressors that are able to handle temperatures of 1000 °C, are commercially not available. To enable a cyclic steady-state operation, the additional heat exchangers keep the storage inlet temperatures constant during charging operation. The authors identify the increase in heat transfer between working fluid and TES as key factor to increase the round-trip efficiency. The described concept was patented by Ruer [118].

Ni and Caram [104] performed simulations based on exponential matrix solution techniques of PHES systems having the same setup as introduced by Desrues et al. [19]. Just as in [19], two additional heat exchangers were used to add and discharge heat, resulting in constant storage inlet temperatures

of the working fluid. Turbomachinery efficiency and TES efficiency were the only loss effects considered. Turbomachinery was identified to be the limiting factor of the round-trip efficiency ranging between 60 % and 100 %, depending on the parameters chosen. For high temperatures in the order of 1000 °C, the required PHES components are commercially not available. Changing the working fluid from argon to air slightly reduced the round-trip efficiency due to the drop of the isentropic exponent. Additionally, Ni and Caram showed that round-trip efficiency and TES utilization ratio have reversed trends. Considering the storage and retrieval of a specific amount of thermal energy, round-trip and storage efficiency increase while storage utilization ratio decreases with increasing size of the TES.

Howes [55] introduced PHES prototypes based on Joule cycles with air as working fluid in combination with two latent heat packed bed TESs. Because research and prototype development has been taking place under the roof of the company Isentropic, detailed information on material and system performance was not published. Howes presented the characteristics of a hypothetical large scale machine using argon as working fluid and realizing hot and cold storage temperatures of 500 °C and −166 °C, respectively. With a nominal power of 2 MW, the round-trip efficiency was extrapolated to 72 %. The high efficiencies of the envisioned reciprocating compressor and expander are currently not state-of-the-art. Howes holds several patents related to the concept introduced [56; 57].

McTigue et al. [87] performed an optimization of the hypothetical large scale machine invented by Howes. Stochastic optimization algorithms were employed in combination with a simulation of the PHES systems in quasi-steady-state. Having a considerable energy storage density of 200 MJ/m^3 the optimized PHES system achieved an overall round-trip efficiency of almost 70 %. Such a high efficiency relies on the employment of highly efficient reciprocating compression and expansion devices, which are commercially not available yet. Their results showed that losses due to compression and expansion processes are dominating whereas losses due to pressure drop and heat transfer are rather small. Considering compression and expansion efficiencies typical for state-of-the-art turbomachinery, the overall round-trip efficiency dropped below 50 %.

White et al. [154] published an analysis of PHES systems based on the concepts presented by Howes and Desrues et al. In order to reveal general trends in efficiency, a simplified analytical model of PHES systems was developed omitting transient effects. The results showed that round-trip efficiency and energy storage density increase with compressor pressure ratio. They conclude that satisfactory round-trip efficiencies require highly efficient compression and expansion processes.

A research group around Morandin (École Polytechnique Fédérale de Lausanne) and Mercangöz (ABB Corporate Research) is working on PHES systems referring to those systems as thermo-electrical energy storage. Based on theoretical considerations Morandin et al. [93] drew the following conclusions about PHES systems: the higher the difference between the temperature levels of the high and low temperature TES, the higher is the efficiency of the heat engine, the smaller are the capacities of both TESs with respect to a specific output of electrical energy, the less important become irreversibilities due to temperature differences, and the more important become turbomachinery losses. Taking costs into consideration, less complex systems were expected to be economically more promising. Morandin et al. [93] presented the theoretical analysis of a closed Joule cycle based PHES system with air as working fluid. Having a maximum cycle temperature of 700 °C, a minimum cycle temperature of 60 °C, a minimum temperature difference of 10 °C and a high isentropic turbomachinery efficiency of 90 %, the round-trip efficiency became 55 %. Morandin et al. concluded that compressors reaching outlet temperatures higher than 650 °C are currently not state-of-the-art. However, more conservative assumptions on turbomachinery efficiency and outlet conditions were expected to lead to a significant decrease of performance. Morandin et al. identified the combination of transcritical Rankine cycle and water storage as more promising PHES concept, which is introduced in the following section.

2.2.2 Rankine cycle based PHES concepts

The research group around Morandin (École Polytechnique Fédérale de Lausanne) and Mercangöz (ABB Corporate Research) introduced a transcritical Rankine cycle based PHES concept with CO_2 as working fluid [94]. Several TES modules were considered, consisting of two tanks each, between which the storage material is pumped back and forth through a heat exchanger. For the high temperature TES, pressurized water with a maximum storage temperature of 176.6 °C was used as storage material. As material for the low temperature TES an eutectic water salt mixture with a phase change temperature of −21.2 °C and a maximum ice concentration of 20 % by mass was employed. The system was modeled and simulated at steady state using BELSIM Vali. A Matlab based optimization of the system with respect to the round-trip efficiency was performed. The optimized system contained eight high temperature and one low temperature storage pairs, producing an electrical energy output of 13 kWh at a round-trip efficiency of 60 %.

Table 2.3: Overview of research activities in the field of PHES systems based on Rankine and related cycles.

group (company), references, year	working fluid	thermal energy storage	additional information, system and analysis shortcomings
Marguerre, [82–84], 1924	water	two direct TESs with water and steam as working and storage fluid, high temperature storage $T_{max} = 170\,°C$, low temperature storage $T_{max} = 70\,°C$	estimation of round-trip efficiency between 40 and 50 % with $E_{el,out} = 15$ MWh and P_{max} between 8 MW and 10 MW
Morandin et al., [94–96], 2012, 2013	transcritical CO_2, additional ammonia Rankine cycle to cool low temperature TES	eight pairs of direct TESs: water (sensible heat, $T_{max} = 177\,°C$), one pair of direct TESs for salt-water/ice storage (latent heat, $T = -21.2\,°C$)	modeling and simulation at steady state with Belsim VALI, round-trip efficiency of 60 % (without superheating) and 62 % (with superheating), $E_{el,out} = 13$ kWh, large scale hydraulic expander is not state-of-the-art yet
Mercangöz et al. (ABB Corporate Research), [89], 2012	transcritical CO_2, ammonia Rankine cycle to cool low temperature TES	a pair of tanks as direct TES: water (sensible heat, $T_{max} = 123\,°C$), a single tank for the water-ice mixture (latent heat, $T = -5\,°C$)	modeling and simulation at steady state with Aspen HYSYS, round-trip efficiency between 51 % (pilot plant, $P = 1$ MW) and 65 % (commercial plant, $P = 50$ MW), large scale hydraulic expander is not state-of-the-art yet
Kim et al., [65], 2013	transcritical CO_2	basic configuration as presented by Morandin et al. and Mercangöz et al. with modification for isothermal compression and expansion	incomplete description of numerical model, maximum round-trip efficiency 74.5 %, based on high isentropic efficiencies of 0.9 and components that are not state-of-the-art yet
Steinmann, [132], 2014	ammonia and water	high temperature: combination of sensible heat (molten salt) and latent heat (nitrate salts) TES, $T_{max} = 400\,°C$, low temperature source: environment	complex system design due to several intercooling stages, preliminary performance estimation yields round-trip efficiency of 70 % based on high turbomachinery efficiency of 0.9, without pressure and thermal losses

In a related publication Morandin et al. [95] presented a further optimization of the base case PHES system taking superheating before the heat pump compressor into consideration. While the round-trip efficiency of the base case with superheating augmented to 62.3 %, optimizations related to topology modification did not yield improved efficiencies. To maximize the round-trip efficiency, Morandin et al. [94] made two suggestions. First, hydraulic expanders should be used instead of throttle valves. Second, cycle internal heat recovery should be maximized before using the TES systems. In addition, they concluded that heat dissipation through storage boundaries can be neglected compared to all other sources of irreversibility.

In a subsequent study, Morandin et al. [96] evaluated the concepts presented in [94; 95] from a thermoeconomic point of view. The authors estimated the trade-off between efficiency and investment costs for a discharge capacity of 50 MW and discharge time of 2 h in order to achieve maximum performance at minimum costs. Again, performance evaluation was based on steady-state simulations. Cost functions relating a component-specific characteristic sizing parameter to the purchased equipment costs were developed based on vendor inquiries. Other significant cost items, such as engineering, piping, and construction, were not considered. However, these cost items were assumed to be proportional to the purchased equipment cost so their neglect did not influence the relative comparison between possible PHES topologies. The base case topology with superheating reached maximum performance at minimum relative cost, having a maximum round-trip efficiency of 64 % at purchased equipment costs of $\$\,34 \cdot 10^6$ (costs based on the year 2009). Morandin et al. found out that the amount of storage tanks and the selection of pressure levels have the largest effect on system performance and costs. Finally, the authors pointed out that the scale up of the technology might be an issue.

Morandin et al. [94; 95] calculated high PHES round-trip efficiencies (Table 2.3). Among the diverse reasons, the most important are the usage of hydraulic expanders instead of throttle valves and the modeling of constant turbomachinery efficiency throughout operation. However, large scale hydraulic expanders are not state-of-the-art yet. For the case that hydraulic expanders cannot be incorporated, Morandin et al. [95] suggested to split the throttling among two valves with vapor separation in between.

Mercangöz et al. [89] (ABB Corporate Research) presented a similar concept as Morandin et al. named electrothermal energy storage based on transcritical Rankine cycles with CO_2 as working fluid. Heat pump and heat engine have simple topologies without internal heat exchangers. Instead of a throttle, a hydraulic expander was used. Pressurized hot water pumped back and forth between two tanks, with a maximum storage temperature of 123 °C being employed as high temperature TES. A single tank water/ice TES was implemented as low temperature TES having a temperature level below environmental temperature. Mercangöz et al. pointed out that the usage of high and low temperature TES does not eliminate the need to reject heat to the environment. Nevertheless, it reduces the heat rejected to the environment to a minimum. Only the heat necessary to balance the entropy production has to be rejected. To release entropy produced in the system due to irreversibilities, the low temperature TES was cooled by an additional ammonia heat pump during heat pump operation. The system was modeled and simulated at steady state using the software Aspen HYSYS with thermodynamic data from REFPROP. A pilot system with a turbine nominal power of 1 MW reached a round-trip efficiency of 51 %; a larger scale commercial system with a turbine nominal power of 50 MW reached a round-trip efficiency of 65 %. The authors expected a further increase in efficiency if internal heat exchange (recuperation) would have been taken into consideration. However, the analyses based on large scale hydraulic expanders that are not state-of-the-art yet. ABB holds several patents regarding the concepts introduced [47–53].

Kim et al. [65] presented a concept of transcritical Rankine cycles with isothermal expansion and compression. The concept employed CO_2 as working fluid and was based on the main concept presented by Morandin et al. [94; 95] and Mercangöz et al. [89]. The isothermal expansion and compression relied

on heat transfer between turbomachinery and TESs using a liquid piston and water injection. From an industry perspective, this technology is not state-of-the-art yet. The mixture of CO_2 and water increases the risk of corrosion in pipes and components. The description of the numerical model is incomplete. Employed equations and presented graphs indicate a transient calculation of the TES systems and a calculation of the remaining components in quasi-steady-state. Considering maximum and minimum storage temperatures of 150 °C and 0 °C, respectively, and high isentropic efficiencies of 0.9, a maximum round-trip efficiency of 74.5 % was obtained.

Steinmann [132] presented a concept named Compressed Heat Energy STorage (CHEST), a combination of conventional Rankine cycles with medium temperature sensible and latent heat TES systems. Using the environment as TES, the heat pump consists of a three stage ammonia compression cycle in combination with a six stage water compression cycle, both with intercooling. The heat engine consists of a multi stage conventional Rankine cycle with water. The complex turbomachinery was combined with a set of sensible heat (molten salt) and latent heat ($NaNO_3$) TES systems having a maximum temperature of 400 °C. As low temperature TES the environment ($T = T_{amb} = 20\,°C$) was chosen. Selecting high isentropic efficiencies of 0.9 and neglecting transient effects, pressure losses and temperature losses, the round-trip efficiency was estimated to 70 %. As specific costs of turbomachinery increase significantly at powers below 1 MW while efficiency of turbomachinery increases with power, Steinmann identified the optimum system size in the range of 5 MW to 10 MW electrical output power. This concept was developed as an alternative to transcritical Rankine cycles with CO_2, because efficient CO_2 engines are not commercially available yet and the availability of efficient compressors for temperatures above 400°C is limited. Furthermore, at temperatures exceeding 600 °C, only packed bed sensible heat thermal energy storage units can be applied.

2.3 Related technology for the storage of electrical energy

An adiabatic compressed air energy storage system imposes similar demanding challenges regarding suitable turbomachinery and TES systems as PHES systems. The working principle of adiabatic CAES systems is similar to that of non-adiabatic CAES systems. Adiabatic CAES systems use electrical energy to power high temperature air compressors. The compressed hot air transfers heat to a TES before being stored in an underground cavern. During discharge, the compressed air is heated by passing through the high temperature TES before expanding in turbine-generator sets that generate electrical energy. Heating the air is necessary to prevent the turbines from freezing. Beginning in 2010, the project ADELE was engaged in concept development of all components and the complete system in order to build and operate a large scale prototype storage system [85; 159; 160]. Project members included the electricity supplier RWE Power, the construction company Züblin, the electrical engineering company General Electric, the grid operator 50Hertz Transmission, the German Aerospace Center (DLR), the university of Magdeburg, and the Fraunhofer Institute for Applied System Technology Ilmenau [85]. In early 2015, RWE Power announced that the plans to build a prototype have been canceled [116].

The development of suitable turbomachinery and TES systems issued the biggest challenge. High temperature compressors are not state-of-the-art yet, they have to be developed [85]. A multistage compressor with intercooling proved to be most suitable, reaching maximum outlet pressures of 55 bar to 70 bar and maximum outlet temperatures of 550 °C to 650 °C [85]. Turbine design was oriented towards existing steam and gas turbines [85] aiming at an electricity output power of 90 MW for each of three turbine strands [160].

Compared to two-tank TES systems using molten salt or thermal oil as storage media, solid media regenerators showed a better thermoeconomic performance leading to their selection as TES systems [85].

Solid media sensible heat TES systems can be applied in a large temperature and pressure range [85]. Other advantages include the absence of additional heat exchangers and the availability of large heat exchange areas. However, solid media sensible heat TES systems have to be constructed as pressure vessels requiring an efficient high temperature insulation between outer casing and storage inventory. As outer casing, prestressed concrete was selected, which is shielded from the hot inventory by insulation and active water cooling [159]. The inventory design is based on ceramic material in a cinder block or backed bed arrangement having a diameter of approximately 13 m, a total mass of 4000 kg to 5000 kg, and providing the thermal capacity for an output energy of 350 MWh_{el} [159].

Preliminary design calculations using 0.9 as isentropic efficiency of the turbomachinery resulted in round-trip efficiencies of up to 70 % [85]. Designed for a lifetime of 30 years [160] with the ability of providing maximum discharge power uniformly for 4 hours, the specific investment costs were estimated to be within 1500 € $(kW_{el})^{-1}$ and 2400 € $(kW_{el})^{-1}$ by the ADELE project members [85].

The German Aerospace Center (DLR) [66; 158] and RWE power [99] criticized the currently unfavorable and prospectively uncertain economic environment for large scale electrical energy storage systems. Consequently they suggested a down-sizing of the ADELE adiabatic CAES system to gain economic feasibility. Krüger et al. [66] identified potential economic and operational feasibility for small scale electrical energy storages being operated by municipal electricity suppliers or industry. They specified the small scale system with a charge/discharge power of 10 MW_{el} to 30 MW_{el} and charge/discharge times of 4 h to 6.5 h, resulting in storage capacities in the order of 50 MWh_{el} to 150 MWh_{el}.

2.4 Heat pump technology

According to a market analysis [108], almost all heat pumps installed in Germany are used for domestic heating and hot water generation. All heat pumps available on the market operate according to the Rankine cycle. As heat sources, the earth, the ambient air, and the groundwater are used [108]. At average heating powers between 10 kW_{th} and 20 kW_{th} [108] the available heat pump systems increase heat source temperatures between 0 °C and 10 °C to supply temperatures of 35 °C to 55 °C [128]. These power and temperature ranges are covered by standard heat pump technology. The manufacturers operate numerously on the market [36; 108] and literature for planning as well as dimensioning is extensively available [13; 105; 128].

Although considerably higher heat source temperatures in the form of waste heat are available in industry and trade, up to now heat pumps are rarely employed in these sectors [78]. One difficulty is the wide range of industrially required heating powers between 100 kW_{th} and 5000 kW_{th} which requires individual planning [58] and leads to high investment costs [78]. A crucial problem are the currently limited maximum supply temperatures of 80 °C to 100 °C [45; 58; 61; 62; 78] being too low for industrial requirements [78].

Joule cycle based heat pumps are currently hardly available on the market; only a few theoretical investigations are published [153]. For special applications, such as aircraft and train air conditioning [44], heat pumps working according to the Joule cycle are employed. Compared to Rankine cycle based technology, these heat pumps suffer from lower component efficiencies resulting in lower coefficients of performance [115]. For the supply of moderate heat flows, large working fluid mass flows have to be circulated because sensible heat only is transferred [115]. These disadvantages have to be considered in the design phase. However, Joule cycle based heat pumps can be advantageous if connected to sensible heat TES systems. Well matched temperature profiles in the form of small temperature differences between working fluid and TES system reduce exergy losses and increase efficiencies.

In summary, heat pump technology to supply heat at temperatures above 100 °C is not commercially available. New concepts combined with suitable working fluids have to be developed and identified [58; 62]. Nevertheless, single components required for heat pumps intended to supply heat at temperatures above 100 °C and powers in the megawatt range are commercially available.

2.5 Heat engine technology

To convert thermal energy into electrical energy, processes based on Rankine cycles as well as Joule cycles can be used. Process selection depends on the temperature level of the thermal energy supplied.

If the heat is mainly supplied as sensible heat, Joule cycles with external heat supply can be used to generate electrical energy. Considering closed cycles, the working fluid and its temperature range can be selected in order to minimize temperature differences and exergy losses due to heat transfer. However, series productions of machines operating according to the Joule cycle with maximum temperatures lower than 500 °C are currently commercially not available [32; 79]. To combine high efficiencies with small powers and flexible load management, micro gas turbines can be utilized [157]. Most of the research connected to Joule cycles focuses on increasing the turbine inlet temperature of the working fluid [32; 79].

If the heat is mainly supplied as latent heat, Rankine cycles are favored to generate electrical energy. During phase change of the working fluid, its temperature stays constant and can be matched to the constant temperature at which the latent heat is available. Consequently, heat transfer can be realized at small temperature differences and small exergy losses. If the temperature level of the supplied heat exceeds 450 °C, conventional Rankine processes with the working fluid water can be applied [113; 157]. For temperature levels of the supplied heat lower than 450 °C, Organic Rankine cycles (ORCs) should be applied to generate electrical energy [113; 157]. Instead of water, an organic working fluid is used, which can be selected matching the temperature level of the supplied heat [16]. Especially for low power processes, ORCs reach higher efficiencies [124] and better economic performance, due to a simpler plant layout [112], than comparable water cycles. Compared to water, organic working fluids have lower enthalpies of vaporization and lower density differences between liquid and vapor, which enables the employment of once-through evaporators [112]. ORC heat engines converting heat at source temperatures between 90 °C and 400 °C into electrical energy in the low kilowatt up to the low megawatt range are commercially available [112]. Currently, most commercial ORCs operate in the megawatt range and are based on a simple cycle architecture, sub-critical working conditions, and pure working fluids [112]. To increase efficiencies, working fluids [43; 147] and process design [43; 106] are current research areas.

Heat engine technology using Joule and Rankine cycles is well established and proved to be reliable in operation [157]. Within the required range of operation, standard Rankine/ORC processes can be selected for PHES systems. However, Joule processes can only be integrated in PHES systems in the form of adjusted concepts.

2.6 Thermal energy storage systems

Thermal energy is, next to chemical energy and nuclear energy, one part of the internal energy [7]. In many thermodynamic processes, including heating, cooling, and phase transition, only the thermal energy needs to be considered, because chemical and nuclear energy remain unchanged.

Thermal energy storage (TES) systems are essential components of PHES systems (Chapter 1, Figure 1.2) because they accomplish the energy storage between heat pump (charging) and heat engine

(discharging) operation. Besides the ability of suitable system integration, TES systems have to fulfill the following technical requirements [33]:

- high volume-specific energy density,
- high heat transfer rates between working fluid and TES material,
- thermal, mechanical, and chemical stability of storage material over the entire TES lifetime,
- and low exergy losses.

TES systems can be classified into three types, based on the principal mode of thermal energy storage [42; 67; 120]:

- sensible heat thermal energy storage,
- latent heat thermal energy storage,
- and thermochemical energy storage.

In the order of enumeration, energy density as well as technological challenges increase while the stage of development decreases [67]. The third storage type considers, in addition to thermal, also chemical energy storage.

2.6.1 Sensible heat thermal energy storage

Sensible heat TES systems belong to the most developed storage technologies [67], especially in the temperature range up to 150 °C, lots of commercial systems are available. Depending on temperature differences, the volume-specific energy density ranges between 20 $\mathrm{kWh\,m^{-3}}$ and 100 $\mathrm{kWh\,m^{-3}}$ [67]. Sensible heat TES systems subject to heat transfer experience a change in thermal energy of their storage material. In the designated temperature range of application, a phase change of the storage material is not intended. Consequently, the change in thermal energy results in a temperature change of the storage material. Especially for high temperature TES systems, large temperature differences between the storage material and the storage surroundings require proper storage insulation and a preferably small ratio between TES surface and TES volume [120]. If the space for the insulation is not limited, conventional insulation should be chosen, being more efficient than vacuum insulation [42]. Important characteristics of the storage material are the temperature range as well as the mass and volume-specific heat capacity. An overview of different storage materials is presented in Table 2.4 [29, Chapter 2.2].

Table 2.4: Overview of different storage materials for sensible heat TES systems [29, Chapter 2.2].

storage material	temperature range in °C	mass-specific heat capacity in kJ (kg K)$^{-1}$	volume-specific heat capacity in kJ (m^3 K)$^{-1}$	density in kg m^{-3}
water	0 - 100[1]	4.19	4175	998
gravel, sand	0 - 800	0.71	1278 - 1420	1800 - 2000
granite	0 - 800	0.75	2062	2750
concrete	0 - 500	0.88	1672 - 2074	1900 - 2300
brick	0 - 1000	0.84	1176 - 1596	1400 - 1900
iron	0 - 800	0.47	3655	7860
thermal oil	0 - 400	1.6 - 1.8	1360 - 1620	850 - 900
gravel-water bed[2]	0 - 100	1.32	2904	2200
molten salt[3]	150 - 450	1.3	1725 - 1970	2243 - 2561
molten sodium	100 - 800	1.3	750 - 925	975 - 1203

[1] Considering pressurized storage tanks, liquid water can reach storage temperatures above 100 °C [100].
[2] 37 percent water by volume
[3] $53\,\mathrm{KNO_3} + 40\,\mathrm{NaNO_2} + 7\,\mathrm{NaNO_3}$

Water has a very high mass and volume-specific heat capacity, is inexpensive, and environmentally friendly. However, considering the non-pressurized case the maximum storage temperature of 100 °C makes the usage of water as storage material not applicable for most PHES systems. Thermal oil is also not applicable for most PHES systems due to a relatively low maximum storage temperature of 400 °C. For solar thermal power plants, molten salts are investigated as high temperature materials in sensible heat TES systems. The most commonly used salt mixtures have solidification temperatures in the range of 140 °C to 550 °C [29, Chapter 2.2; 33; 120, Chapter 3.2.1]. Preventing solidification, which would destroy sensible heat TES systems, requires complex safety measures that disqualify the application of molten salts as sensible heat TES materials. Solid materials such as concrete, granite, gravel, bricks, and metal provide high temperature ranges that enable their application in PHES systems. However, their performance as storage media is limited by convective and conductive thermal resistances during heat transfer.

Massive block solid media thermal energy storage

Solid media TES can be constructed as massive blocks being traversed by heat exchanger channels conveying the working fluid. In several experimental studies, the DLR proved that concrete is a suitable material for storing sensible heat regarding storage performance and cyclic stability [68; 69; 73–76]. For a long lifetime of the storage unit, the material has to withstand cyclic stresses at temperatures up to 500 °C due to numerous consecutive charging and discharging periods.

High temperature concrete was identified to be the preferred TES material compared to castable ceramic due to lower purchased equipment costs, higher material strength and easier handling [75]. Concrete with different compositions regarding binder, aggregates, and auxiliary materials was tested. The best performance was achieved with a composition similar to conventional construction concrete (Table 2.5) [68]. A modular design of the TES system enables the scalability of the storage capacity from the kWh-range to the GWh-range [73; 74]. The economic integration of concrete TES into parabolic trough power plants [76] and the possibility of direct steam generation by combining concrete TES with a latent heat TES [69], was also investigated by the DLR.

Table 2.5: Properties of high temperature concrete usable in sensible heat TES systems [68].

temperature T in °C	density ρ in kg m^{-3}	specific heat capacity c in J (kg K)$^{-1}$	thermal conductivity λ in W (m K)$^{-1}$
25	2250	720	1.45
400	2250	1050	1.20

Packed bed solid media thermal energy storage

To enhance heat transfer between storage material and working fluid, the storage material can be integrated as packed bed instead of as massive block. The implementation of spherical or nearly spherical solid particles in cylindrical storage containers is often documented [40; 119; 120, Chapter 3.2.1.1]. During charging and discharging operation, the working fluid flows around the particles through the packed bed. The smaller the particles, the more favorable is the ratio of particle surface area to particle volume and the higher is the possibility for turbulent flow conditions to develop. Consequently, the packed bed arrangement increases heat transfer between working fluid and storage material at the ex-

pense of a higher pressure loss [25; 34; 40; 156]. Particle sizes in the range of $0.5\,\mathrm{mm} \leq d_{\mathrm{Pa}} \leq 100\,\mathrm{mm}$ have recently been investigated [46; 90].

The usage of solid material brings the advantages of high storage temperatures and low material costs [40; 120, Chapter 3.2.1.1]. However, suitable media must have a high volume-specific heat capacity combined with thermal and mechanical long term stability, which is the focus of recent studies [40; 119].

In a numerical study, Hänchen [40] showed that the volume-specific heat capacity of the storage media has a significant influence on the temperature distribution inside the storage, while the thermal conductivity has only a minor influence. This result is evident for particles having Biot numbers smaller than one, which indicates that the convective thermal resistance between particle and working fluid dominates the conductive thermal resistance inside the particle. Rundel et al. [119] experimentally investigated the thermal and mechanical long term stability of packed beds. Basalt chips best withstood the cyclic stresses coming from up to 7000 charging and discharging periods with working fluid inlet temperatures of 600 °C and 24 °C, respectively. Built by the DLR in Stuttgart, the test rig HOTREG is used to study the performance of packed bed solid media TES systems and validate theoretical models [77].

2.6.2 Latent heat thermal energy storage

Realizing volume-specific energy densities between $50\,\mathrm{kWh\,m^{-3}}$ and $150\,\mathrm{kWh\,m^{-3}}$ at minimal temperature differences, latent heat thermal energy storage systems reach higher volume-specific storage capacities than sensible heat thermal energy storage systems [67]. However, compared to the latter storage technology, latent heat TES systems are less established [67] and generate higher costs [120, Chapter 3.2.2]. During heat transfer within a suitable temperature range, the phase change material (PCM) experiences a solid-liquid or liquid-vapor phase change. Compared to the liquid-vapor phase change which is connected to a relatively large change in volume, the solid-liquid phase change is characterized by a relatively small volume change. Therefore, PCMs experiencing a solid-liquid phase change are usually employed, preventing large pressure changes within the storage module [42, Chapter 2]. As a consequence, latent heat TES systems based on a solid-liquid phase change are solely considered in this work. Heat transfer during phase change causes a rearrangement of the PCMs atomic lattice, resulting in a constant temperature of the PCM during charging and discharging of the TES [120, Chapter 3.2.2]. Especially beneficial during the discharging, latent heat TES systems are capable of supplying large amounts of heat at a constant temperature.

The main advantages of latent heat TES systems, high volume-specific storage capacity and constant phase change temperature, are faced by two disadvantages. The low thermal conductivity of solid PCMs requires constructional measures to enhance heat transfer [33; 120, Chapter 3.2.2]. Furthermore, the selection of appropriate phase change materials might be difficult, because thermodynamic properties are required that are suitable for the respective range of application.

According to the classification depicted in Figure 2.2 Sharma et al. [126] present an extensive review of potential PCMs, supplemented by a rating of their applicability. Hauer et al. [42, Chapter 4] classify PCMs into:

- water-ice mixtures, which are currently most often applied,
- salt hydrates, which are affected by segregation,
- paraffins, which are stable and ecologically friendly but are affected by low thermal conductivities,
- and composite materials, which combine a PCM with a material of high thermal conductivity.

Covering a melting temperature range between 0 °C and 767 °C, Agyenim et al. [3] summarize the most relevant thermodynamic properties of 33 PCMs that have been investigated for and employed in different TES systems.

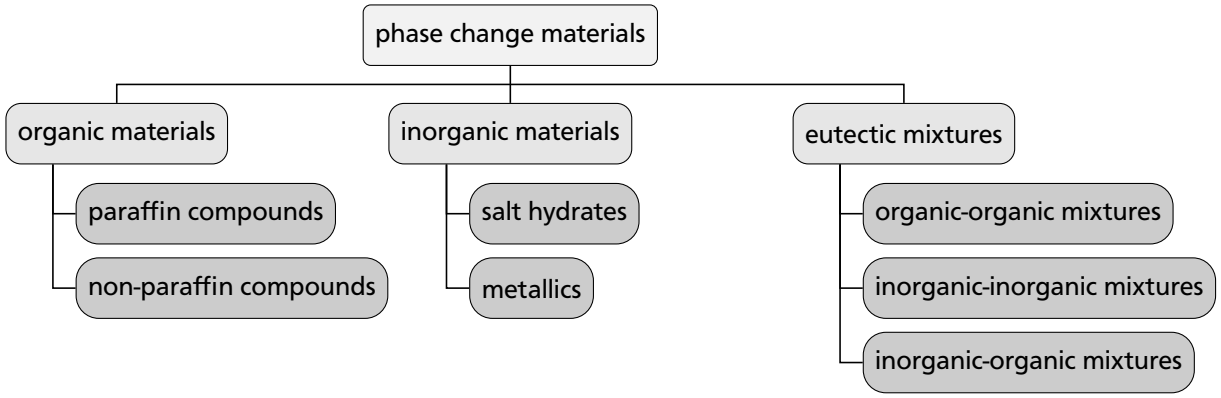

Figure 2.2: Classification of PCMs according to Sharma et al. [126].

Criteria for the slection of suitable PCMs are given in [3; 33; 120, Chapter 3.2.2], the most important of which are:

- phase change temperature in accordance with range of application,
- high mass-specific enthalpy of fusion,
- high mass-specific heat capacity for the storage of sensible heat,
- high thermal conductivity of liquid and solid PCM,
- and small density differences between solid and liquid PCM.

Geometry and construction of the PCM container influence the heat transfer during charging and discharging of the TES. Especially due to the low thermal conductivity of most phase change materials, heat transfer enhancement techniques are necessary. For the sake of simplicity, ease of fabrication, and low costs, finned tubes embedded in a shell and tube arrangement are most often applied [3]. Other enhancement techniques include the insertion of a metal or graphite matrix into the PCM, the dispersion with high conductivity particles, or the micro-encapsulation of the PCM [3; 33; 42, Chapter 4].

Latent heat TES systems are subject of complex research activities. As main research focus, high phase change enthalpy shall be combined with high thermal conductivity and at a suitable temperature range for the respective area of application [42, Chapter 6].

2.6.3 Thermochemical energy storage

Thermochemical energy storage systems use thermal and chemical energy to store heat as internal energy. The storage is based on sorption and desorption processes on the one hand, as well as endo- and exothermic reactions on the other hand [42; 67]. Processes and reactions can be chosen in order to match temperature levels of heat supply and demand [42]. With $100\,\mathrm{kWh\,m^{-3}}$ to $400\,\mathrm{kWh\,m^{-3}}$, this storage type reaches even higher volume-specific energy densities than latent heat TES systems [67]. However, thermochemical energy storage systems are the least developed among the presented TES technologies which results in high costs and high technological risks [67; 120]. For this reason, thermochemical energy storage systems are not considered as components for PHES systems in this work.

3 Research Questions and Objectives

Although far from abundance, the frequency of recent publications about PHES systems is rising, proving that this research subject becomes increasingly important. Most publications present efficiency estimations and performance extrapolations for PHES systems, whereas transient and steady-state simulations of PHES systems are rare. Especially the detailed analysis of transient system operation is necessary to evaluate the performance of storage systems in general and PHES systems in particular. The lack of transient analyses constitutes a research gap from which the first objective of this work is deduced.

Objective 1: Development of numerical models that enable a transient simulation and analysis of PHES systems of different types.

The majority of performance estimations and simulations of PHES systems is based on efficiencies, temperatures, or temperature and pressure ranges, that cannot be realized by employing state-of-the-art technology. In some concepts, entire components are far from technical realization (Tables 2.2 and 2.3). Evaluations and comparisons of PHES systems built of commercially procurable components at best, but at least based on state-of-the-art technology are currently not available. Consequently, identifying the system design that yields the highest round-trip efficiency and/or lowest storage costs constitutes another research gap from which the second objective of this work is deduced.

Objective 2: Evaluate the energetic and economic performance of PHES systems based on commercially procurable and state-of-the-art technology.

An exergoeconomic analysis is chosen as evaluation method, because it assesses both, the thermodynamic quality as well as the economic constraints of energy conversion. The operation of the PHES systems is simulated transiently employing the numerical models developed in this work. Based on design constraints deduced from the literature review, concepts for PHES systems are developed. Because Joule systems with sensible heat thermal energy storage on the one hand, and Rankine systems with latent heat thermal energy storage on the other hand, are the concepts predominantly covered in literature, these concepts are analyzed in detail in this work.

4 System Modeling and Analysis Procedures

The process simulation software EBSILON®*Professional* [130] is used as platform to model and simulate the PHES systems. All components of the thermodynamic cycles are simulated in quasi-steady-state, whereas the TES systems are simulated transiently. Further details on modeling and simulation are presented in the following sections.

4.1 Modeling of thermodynamic cycles

To model and simulate the thermodynamic cycles of heat pump and heat engine, the built-in components of EBSILON®*Professional* are used. First, the design point of the thermodynamic cycle has to be modeled and simulated. Afterwards, the off-design performance can be simulated. All off-design simulations are based on the component-specific off-design performance characteristics implemented in EBSILON®*Professional* and accessible via the PHES models. The pipes connecting the different components are modeled adiabatic and isobaric.

4.2 Modeling of sensible heat thermal energy storage systems

With the component 119 (Indirect Storage) EBSILON®*Professional* provides a model for a sensible heat thermal energy storage system. The model consists of a single pipe conducting the working fluid encased by a cylindrical shell containing the storage material (Figure 4.1). The dimensions of pipe and shell can be adapted but the basic topology cannot be changed.

Within the storage material, heat conduction is the only means of energy transport. Density ρ, mass-specific heat capacity c, and thermal conductivity λ of the storage material can be defined as constants or variables, linearly depending on temperature. Thermal resistances due to convection between storage

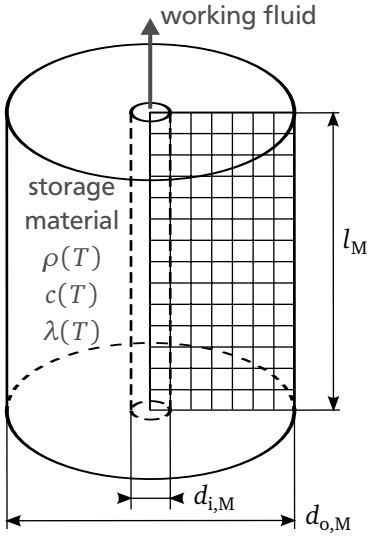

Figure 4.1: Layout of the sensible heat TES model implemented in EBSILON®*Professional*.

material and working fluid as well as between storage material and surroundings have to be provided to the model.

The differential equation describing heat conduction within the storage material is discretized on a rectangular grid which is equidistantly spaced in radial, as well as longitudinal direction (Figure 4.1). In general, however, the constant spacing does not have to be equal in both directions. Starting at the centerline of the pipe, the first longitudinal row of grid cells is used to discretize the working fluid while all other grid cells are used to discretize the storage material. The solver is based on a cylindrically symmetrical finite differences approach using the implicit Crank-Nicolson method.

The adaptions made on the basic model to simulate a sensible heat TES in the form of a massive block traversed by multiple pipes are described in [23]. To enhance heat transfer between working fluid and storage material, the storage material can be integrated in the form of a packed bed instead of a massive block (Chapter 2.6.1). The packed bed sensible heat TES shall be considered in this work. The necessary adaptions to the basic model are described in the following section.

4.2.1 Modeling approach of packed bed sensible heat thermal energy storage system

Ismail and Stuginsky [60] present an extensive overview and comparison of modeling approaches for packed bed TES systems. More condensed reviews are provided by Hänchen et al. [40] and Gil et al. [33]. The selected modeling approach needs to be integrated into the framework of the EBSILON®*Professional* sensible heat TES model described at the beginning of Chapter 4.2. Therefore, a modeling approach similar to the one-dimensional, two-phase approach by Hänchen et al. [40] is developed. The modeling approach is based on the following assumptions:

- uniformly packed bed,
- turbulent flow conditions of the working fluid, which are homogeneous when temporally averaged over the flow cross section,
- the thermal energy storage capacity of the working fluid can be neglected,
- heat losses to the environment can be neglected,
- and temperature distribution within particles can be neglected.

Based on homogeneously sized particles, the first two assumptions are valid as long as wall effects at the inner side of the outer packed bed boundary d_{R} can be neglected. This holds true if the particle diameter d_{Pa} is selected according to the inequality $d_{\mathrm{R}}/d_{\mathrm{Pa}} > 40$ [88]. The third assumption is justified by the volume-specific heat capacity of the fluid which is at least three orders of magnitude smaller than the volume-specific heat capacity of the storage material. The neglect of heat losses to the environment is valid for large TES units with small surface-to-volume ratios [88] and was confirmed by own calculations [31, Chapter 5.1.3], determining the exergy loss resulting from heat losses to the environment to be less than $0.3\,\%\,(24\,\mathrm{h})^{-1}$. Since the thermal resistance due to conduction within the particle is approximately one order of magnitude smaller than the thermal resistance due to convection between particle and working fluid, the Biot number drops below unity ($Bi < 1$) which justifies the assumption of a constant temperature distribution within each particle. These assumptions implicate a vanishing temperature gradient in radial direction. As a temperature gradient can only develop in longitudinal direction a one-dimensional modeling approach is possible.

The topologies of the real storage module and its model are compared in Figure 4.2. The indices Pa, R, and M refer to quantities of the particle, the real storage module, and the storage model, respectively. The length of the model l_M (measured along the flow direction of the working fluid) shall be equal to the length of the real storage module l_R

$$l_\mathrm{M} = l_\mathrm{R}. \tag{4.1}$$

The real storage module is filled with the packed bed having voids characterized by the void fraction ϵ, defined by the volumes V of storage module and particles as [34]

$$\epsilon = \frac{V_{\text{of storage module}} - V_{\text{of all particles in the storage module}}}{V_{\text{of storage module}}}. \tag{4.2}$$

Without voids, the model shell is entirely filled with the solid particle material having the particle density ρ_Pa. The mass-specific heat capacity of the model shell c_M shall be equal to the mass-specific heat capacity of the particles c_Pa

$$c_\mathrm{M} = c_\mathrm{Pa}. \tag{4.3}$$

The equality of particle mass in model M_M and reality M_R can be expressed in the first modeling equation

$$\begin{aligned} M_\mathrm{M} &= M_\mathrm{R} \\ \frac{\pi}{4}\left(d_{\mathrm{o,M}}^2 - d_{\mathrm{i,M}}^2\right) l_\mathrm{R}\rho_\mathrm{Pa} &= \frac{\pi}{4} d_\mathrm{R}^2 l_\mathrm{R}(1-\epsilon)\rho_\mathrm{Pa}. \end{aligned} \tag{4.4}$$

The diameter of the real storage module and the inner as well as outer diameter of the storage model are denoted by d_R, $d_{\mathrm{i,M}}$, and $d_{\mathrm{o,M}}$, respectively.

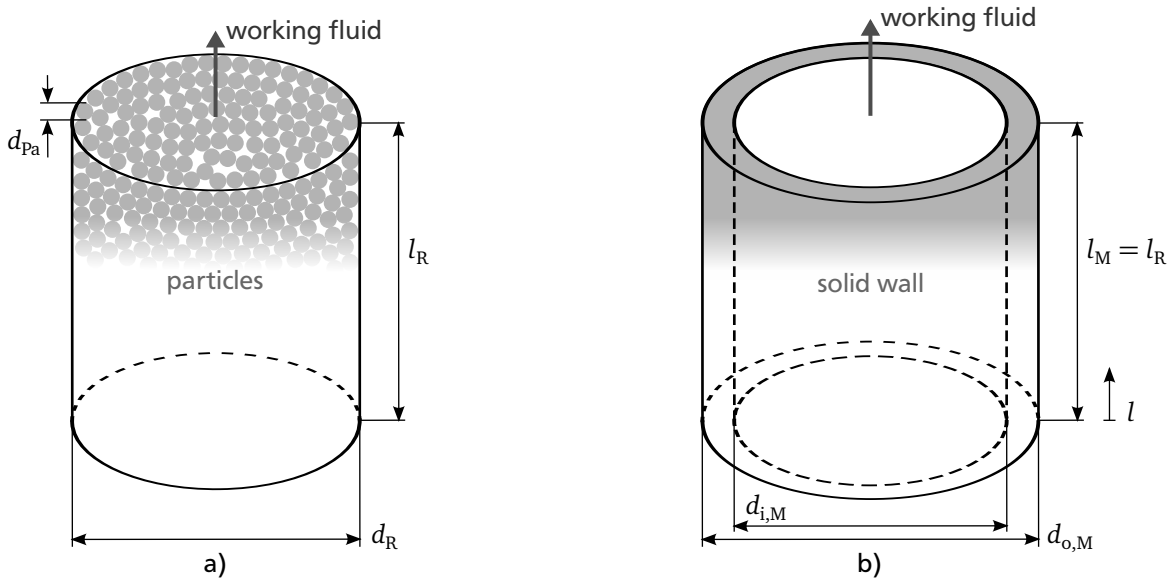

Figure 4.2: Topologies of the packed bed sensible heat TES a) and its model implemented in EBSILON® *Professional* b).

In order to correctly model the ratio of thermal resistances due to convection and conduction, a Biot number Bi equality is expressed in the second modeling equation

$$\begin{aligned} Bi_{\mathrm{M}} &= Bi_{\mathrm{Pa}} \\ \frac{\alpha_{\mathrm{M}} \left(d_{\mathrm{o,M}} - d_{\mathrm{i,M}} \right)}{2\,\lambda_{\mathrm{M}}} &= \frac{\alpha_{\mathrm{R}} d_{\mathrm{Pa}}}{2\,\lambda_{\mathrm{Pa}}}, \end{aligned} \tag{4.5}$$

with d_{Pa}, λ_{Pa}, and λ_{M} being the particle diameter, the thermal conductivity of a single particle, and the thermal conductivity of the model shell, respectively. The convective heat transfer coefficients between working fluid and particles, as well as between working fluid and solid wall are denoted by α_{R} and α_{M}, respectively. The model is limited to an isotropic thermal conductivity λ_{M} being equal in radial and longitudinal direction. When fluid flows through the sensible heat TES, the effective thermal conductivity in longitudinal direction exceeds the effective thermal conductivity in radial direction. As temperature gradients in radial direction can be neglected, the effective thermal conductivity in longitudinal direction is considered for λ_{M}.

The thermal resistance R due to convection between the working fluid and the solid particles shall be equal in model and reality, which is expressed in the third modeling equation

$$\begin{aligned} R_{\mathrm{convection,M}} &= R_{\mathrm{convection,R}} \\ \alpha_{\mathrm{M}} A_{\mathrm{surface,M}} &= \alpha_{\mathrm{R}} A_{\mathrm{surface,R}}. \end{aligned} \tag{4.6}$$

$A_{\mathrm{surface,M}}$ denotes the inner surface area of the storage shell that is in contact with the working fluid and $A_{\mathrm{surface,R}}$ denotes the surface area of all particles in the real storage module, which are given by

$$A_{\mathrm{surface,M}} = \pi d_{\mathrm{i,M}} l_{\mathrm{R}}, \tag{4.7}$$

$$A_{\mathrm{surface,R}} = \frac{\sum_{\text{all particles}} V_{\mathrm{Pa}}}{V_{\mathrm{Pa}}} A_{\mathrm{surface,Pa}} = \frac{3\,(1-\epsilon)\pi d_{\mathrm{R}}^2 l_{\mathrm{R}}}{2\,d_{\mathrm{Pa}}}. \tag{4.8}$$

Using the three modeling equations 4.4 to 4.6, the three unknown model parameters of the packed bed sensible heat TES can be determined to

$$d_{\mathrm{i,M}} = \sqrt{(1-\epsilon) d_{\mathrm{R}}^2 \cdot \frac{1}{K^2 - 1}} \tag{4.9}$$

$$d_{\mathrm{o,M}} = \sqrt{(1-\epsilon) d_{\mathrm{R}}^2 \cdot \frac{K^2}{K^2 - 1}} \tag{4.10}$$

$$\alpha_{\mathrm{M}} = \alpha_{\mathrm{R}} \cdot \frac{3\,d_{\mathrm{R}}^2 (1-\epsilon)}{2\,d_{\mathrm{Pa}} d_{\mathrm{i,M}}} \tag{4.11}$$

using the dimensionless parameter

$$K = \frac{2\,d_{\mathrm{Pa}}^2 \lambda_{\mathrm{M}}}{3\,d_{\mathrm{R}}^2 \lambda_{\mathrm{Pa}} (1-\epsilon)} + 1. \tag{4.12}$$

For the real storage module, the global convective heat transfer coefficient α_{R} between working fluid and packed bed is calculated based on an approach suggested by Gnielinski [34].

$$\alpha_{\mathrm{R}} = \frac{\lambda_{\mathrm{fluid}} Nu_{\mathrm{R}}}{d_{\mathrm{Pa}}} \tag{4.13}$$

$$Nu_{\mathrm{R}} = f\, Nu_{\mathrm{sphere}} = f\, \sqrt{Nu_{\mathrm{lam}}^2 + Nu_{\mathrm{turb}}^2} \tag{4.14}$$

The thermal conductivity of the working fluid is denoted by λ_{fluid}. Depending on the laminar Nu_{lam} and turbulent Nu_{turb} Nusselt numbers, the Nusselt number Nu_{sphere} applicable to flows around a single sphere is corrected by a form factor f resulting in the Nusselt number Nu_{R} for flows through a packed bed.

$$Nu_{\mathrm{lam}} = 0.664\, Re_{\epsilon}^{1/2} Pr_{\mathrm{fluid}}^{1/3} \tag{4.15}$$

$$Nu_{\mathrm{turb}} = \frac{0.037\, Re_{\epsilon}^{0.8} Pr_{\mathrm{fluid}}}{1 + 2.443\, Re_{\epsilon}^{-0.1} \left(Pr_{\mathrm{fluid}}^{2/3} - 1 \right)} \tag{4.16}$$

$$Re_{\epsilon} = \frac{u_{\mathrm{free}} d_{\mathrm{Pa}}}{\nu_{\mathrm{fluid}} \epsilon} = \frac{4\, \dot{M}_{\mathrm{fluid}} d_{\mathrm{Pa}}}{\pi d_{\mathrm{R}}^2 \rho_{\mathrm{fluid}} \nu_{\mathrm{fluid}} \epsilon} \tag{4.17}$$

The Reynolds number and the Prandtl number of the working fluid passing through the packed bed are denoted by Re_{ϵ} and Pr_{fluid}, respectively. u_{free} describes the undisturbed free stream velocity of the working fluid that would develop in the storage module, if the packed bed was not present. Mass flow, density and kinematic viscosity of the working fluid are given by $\dot{M}_{\mathrm{fluid}}$, ρ_{fluid}, and ν_{fluid}, respectively. All properties of the working fluid have to be evaluated at its mean temperature within the packed bed. For a packed bed consisting of equally sized spherical particles of diameter d_{Pa} the form factor can be approximated to [34]

$$f = 1 + 1.5\,(1 - \epsilon). \tag{4.18}$$

The effective thermal conductivity $\lambda_{\mathrm{M,still}}$ of the packed bed for the non-flown-through case is calculated according to an approach developed by Zehner et al. and described by Tsotsas [143]

$$\lambda_{\mathrm{M,still}} = \left(1 + (k_{\mathrm{c}} - 1) \sqrt{1 - \epsilon} \right) \lambda_{\mathrm{fluid}}. \tag{4.19}$$

The dimensionless parameters required to evaluate Equation (4.19) are defined as

$$k_{\mathrm{c}} = \frac{2}{N} \left(\frac{B}{N^2} \frac{k_{\mathrm{Pa}} - 1}{k_{\mathrm{Pa}}} \ln \frac{k_{\mathrm{Pa}}}{B} - \frac{B+1}{2} - \frac{B-1}{N} \right) \tag{4.20}$$

$$N = 1 - \frac{B}{k_{\mathrm{Pa}}} \tag{4.21}$$

$$k_{\mathrm{Pa}} = \frac{\lambda_{\mathrm{Pa}}}{\lambda_{\mathrm{fluid}}} \tag{4.22}$$

$$B = 1.25 \left(\frac{1 - \epsilon}{\epsilon} \right)^{\frac{10}{9}}. \tag{4.23}$$

For the flown-through case, the effective thermal conductivity in longitudinal direction λ_{M} is determined based on Tsotsas [142]

$$\lambda_{\mathrm{M}} = \lambda_{\mathrm{M,still}} + 0.5\, u_{\mathrm{free}} \rho_{\mathrm{fluid}} c_{p,\mathrm{fluid}} d_{\mathrm{Pa}}, \tag{4.24}$$

with $c_{p,\mathrm{fluid}}$ denoting the working fluid mass-specific heat capacity at constant pressure.

The nominal pressure drop $\Delta p_{\mathrm{TES,N}}$ allocated to the working fluid due to its passage through the packed bed is calculated according to the measurement-based, empirical equation deduced by Ergun [25; 156]

$$\Delta p_{\mathrm{TES,N}} = \left(150 \frac{(1-\epsilon)^2}{\epsilon^3} \frac{\nu_{\mathrm{fluid}} \rho_{\mathrm{fluid}} u_{\mathrm{free}}}{d_{\mathrm{Pa}}^2} + 1.75 \frac{1-\epsilon}{\epsilon^3} \frac{\rho_{\mathrm{fluid}} u_{\mathrm{free}}^2}{d_{\mathrm{Pa}}} \right) l_{\mathrm{R}}. \tag{4.25}$$

The convective heat transfer coefficient, the thermal conductivities, and the nominal pressure drop are determined separately for each TES system in each operation mode. The fluid properties required for the determination are evaluated based on mean values of temperature and pressure of the working fluid entering and leaving the TES system. Originating from the modeling approach of the packed bed sensible heat TES, the convective heat transfer coefficient and the thermal conductivities determine the geometrical model parameters (Equations (4.9) to (4.12)). For the model parameters to remain constant during each operation mode, the convective heat transfer coefficient and the thermal conductivities are considered as constants.

The actual pressure drop Δp_{TES} experienced by the working fluid when flowing through the packed bed TES depends on the actual and the nominal working fluid mass flow, $\dot{M}_{\mathrm{fluid}}$ and $\dot{M}_{\mathrm{fluid,N}}$, respectively, and is calculated according to [130]

$$\Delta p_{\mathrm{TES}} = \Delta p_{\mathrm{TES,N}} \left(\frac{\dot{M}_{\mathrm{fluid}}}{\dot{M}_{\mathrm{fluid,N}}} \right)^2. \tag{4.26}$$

For Equation (4.26) the nominal mass flow is given by the mean mass flow passing each TES system during each operation mode bounded by the operation times τ_{begin} and τ_{end}.

$$\dot{M}_{\mathrm{fluid,N}} = \overline{\dot{M}}_{\mathrm{fluid}} = \frac{\int_{\tau_{\mathrm{begin}}}^{\tau_{\mathrm{end}}} \dot{M}_{\mathrm{fluid}}\, \mathrm{d}\tau}{\tau_{\mathrm{end}} - \tau_{\mathrm{begin}}}. \tag{4.27}$$

4.2.2 Validation

For the packed bed sensible heat TES, the simulation of working fluid and storage temperatures is validated through comparisons with experimental data by Meier et al. [88] as well as simulation results by Hänchen et al. [40]. Compared to the modeling approach chosen in this work, the model of Hänchen et al. is also based on a one-dimensional, two-phase approach but additionally considers heat losses to the environment.

The charging operation of a cylindrical TES module filled with a packed bed of spherical steatite (magnesium silicate rock) particles is considered (Table 4.1). Initially being at ambient temperature of $T_{\mathrm{init}} = T_{\mathrm{amb}} = 20\,^{\circ}\mathrm{C}$ the TES system is subject to a charging air mass flow of $\dot{M}_{\mathrm{fluid,0}} = 3.87 \cdot 10^{-3}\,\mathrm{kg\,s^{-1}}$ at a temperature of $T_{\mathrm{fluid,in}} = 550\,^{\circ}\mathrm{C}$. Compared to the experimental setup, Hänchen et al. reduced the working fluid mass flow entering the model by 15 % to compensate wall effects introduced by the

Table 4.1: Dimensions of the storage module and material properties of the packed bed (steatite, magnesium silicate rock) [40].

d_R	l_R	d_{Pa}	ϵ	ρ_{Pa}	c_{Pa}	λ_{Pa}
0.148 m	1.2 m	0.02 m	0.4	2680 kg m^{-3}	1068 J (kg K)$^{-1}$	2.5 W (m K)$^{-1}$

Table 4.2: Packed bed sensible heat TES input parameters and corresponding Biot numbers.

Calculation	$\dot{M}_{fluid}$	α_R in W (m^2 K)$^{-1}$	λ_M in W (m K)$^{-1}$	Bi
Hänchen et al. [40]	$0.85\,\dot{M}_{fluid,0}$	24.47	0.1060	0.098
packed bed latent heat TES, calculation 1	$0.85\,\dot{M}_{fluid,0}$	24.47	0.1060	0.098
packed bed latent heat TES, calculation 2	$0.83\,\dot{M}_{fluid,0}$	17.00	0.1060	0.068

small ratio of $d_R/d_{Pa} = 7.4 < 40$ ([88]). The input parameters chosen by Hänchen et al. and the input parameters used for two different validation calculations are summarized in Table 4.2. All simulations are performed with 100 grid elements in longitudinal direction (flow direction).

For calculation 1, the same input parameters as used by Hänchen are selected. At different times the temperature distributions along the longitudinal position of the TES show good agreement with the experimental data as well as with the reference simulation (Figure 4.3 a)). For calculation 2, the input parameters have been slightly adjusted to achieve an even better agreement with the experimental data as well as with the reference simulation (Figure 4.3 b)).

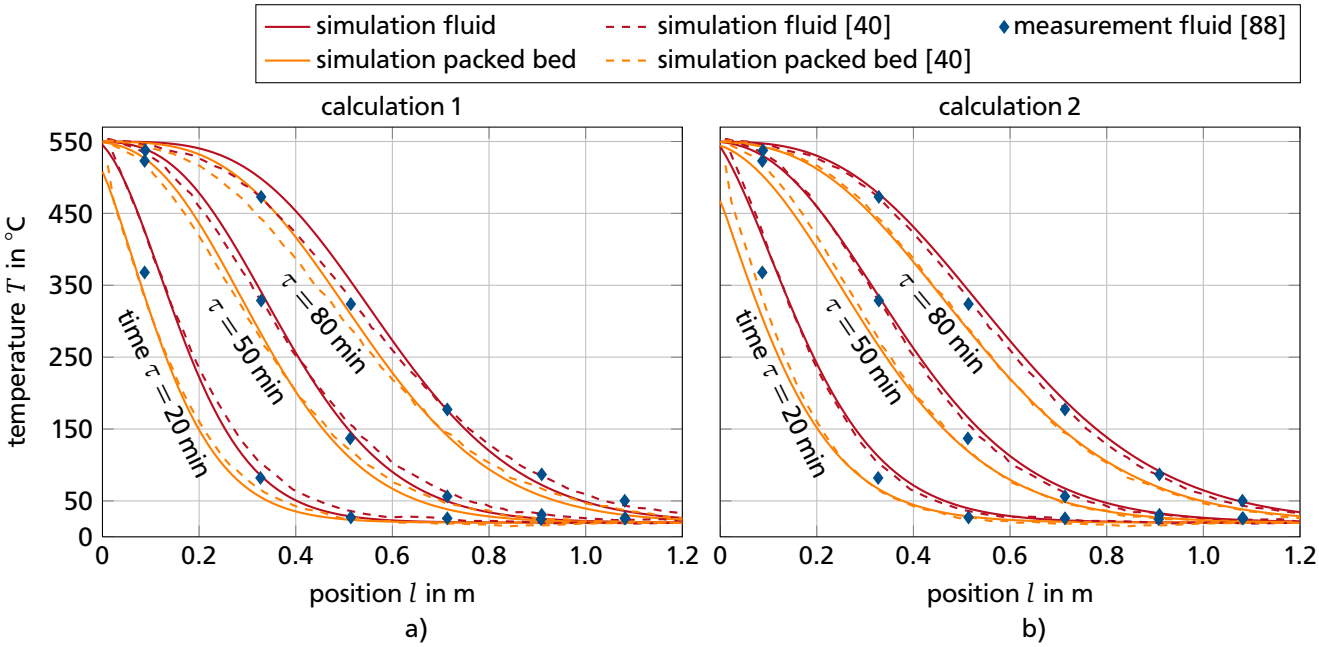

Figure 4.3: Temperature distribution during charging operation of a packed bed sensible heat TES at fixed times along the longitudinal position l. Comparison of sensible heat TES simulation results with experimental data by Meier et al. [88] and simulation results by Hänchen et al. [40]. The simulation input parameters of the storage model are: a) chosen to be identical with the input parameters of Hänchen et al. [40]; b) adjusted to match the experimental data and the reference simulation closely.

Hänchen et al. determine the convective heat transfer coefficient between working fluid and packed bed α_R using an approach of Coutier and Farber [17]. The thermal conductivity of the flown-through packed bed λ_M is based on a rather simple series arrangement of particle and working fluid thermal resistances. The applicability of these approaches in a wide range of operational parameters was not shown. Therefore, the approaches listed in the VDI Heat Atlas and introduced at the end of Chapter 4.2.1 are used throughout this work to calculate α_R [34] and λ_M [142; 143].

In summary, the calculated temperatures of working fluid and packed bed are in good agreement with reference data which successfully concludes the validation of the model for the packed bed sensible heat TES. If experimental data of the TES is available, the model parameters can be adjusted so that the simulation results closely resemble real storage performance. If experimental data is not available, empirical calculations have to be deployed to determine the global convective heat transfer coefficient α_R between storage particles and working fluid, the thermal conductivity of the packed bed λ_M and the pressure drop of the working fluid Δp_{TES}. This procedure might introduce deviations between simulation results and real storage performance, but represents the most reliable approach available.

4.3 Modeling of latent heat thermal energy storage systems

Because EBSILON®*Professional* does not contain a component that can be used to model and simulate a latent heat TES, a suitable component was developed and implemented. EBSILON®*Professional* provides two interfaces to connect user-defined components to the rest of the thermodynamic cycle: a programmable DLL component and a programmable Kernel Scripting component.

Using the former approach, third party software can be utilized to implement the TES system and generate a TES DLL. The DLL is then loaded into EBSILON®*Professional* as individual component. This enables the employment of third party software that facilitates the discretization and solution of differential equations by providing efficient and robust algorithms. However, the program stored in the DLL cannot access the working fluid databases implemented in EBSILON®*Professional*. As access to the working fluid databases is crucial to calculate the heat transfer between working fluid and latent heat TES, the programmable DLL approach is not applicable in the context of this work.

As a consequence, a programmable Kernel Scripting component has to be used to implement the latent heat TES. Using a Pascal based programming language, the program simulating the TES is directly written in EBSILON®*Professional*, which enables the access to the working fluid databases. When the thermodynamic cycle is solved, the program stored in the Kernel Scripting component is solved simultaneously. As drawback of this approach, EBSILON®*Professional* does not provide functions that facilitate the discretization and solution of differential equations. Therefore all numerical methods have to be implemented by hand, which limits the level of complexity of the feasible methods.

4.3.1 Possible modeling approaches

Phase transition in melting and solidification processes can be described as boundary value problem for partial differential equations, in which the phase boundary can move with time [24]. Such a problem is known as Stefan problem, named after a Slovene physicist who introduced the general class of such problems in 1889 [24; 131].

Belmonte et al. [12] proposed a generic modeling approach which does not solve the Stefan problem and assumes that the entire storage volume has a uniform temperature. For the entire storage volume, a single equation based on the first law of thermodynamics was solved. The model accuracy was considerably affected by the selected phase change material (PCM) and the operation mode (charging or

discharging) and therefore is acceptable for preliminary design purposes only. Because Belmontes approach does neither provide reliable accuracy nor a resolution of the temperature and energy fields in the PCM, it is not selected as modeling approach.

Dutil et al. [24] and Verma et al. [150] presented extensive reviews on mathematical modeling and simulation of phase-change materials. A frequently adopted approach is the enthalpy method, in which an enthalpy based heat conduction equation is solved for the PCM. To solve the heat conduction equation, the PCM domain can be discretized by finite differences, finite elements or finite volume approaches. Due to its simplicity and widespread use, a finite differences enthalpy method is implemented in the programmable Kernel Scripting component of EBSILON®*Professional*. At sufficiently fine discretization, the chosen approach combines acceptable computational effort with reliable results.

More complex solution procedures to the Stefan problem, as front tracking methods in the form of adaptive mesh or moving mesh methods, are not considered. The higher computational effort hinders the integration into entire PHES system models.

4.3.2 Finite differences enthalpy method

The model of the latent heat thermal energy storage is implemented as Kernel Scripting component in EBSILON®*Professional*. The model is based on the finite differences enthalpy method described by Alexiades and Solomon [5] and builds on the following simplifications [5, Chapter 1]:

- isotropic heat conduction as only mode of heat transfer in the PCM,
- constant latent heat, which is released or absorbed at a fixed phase-change temperature,
- no nucleation difficulties, no supercooling effects,
- sharp phase-change interface,
- neglect of surface tension and curvature effects (at the interface),
- phase-wise constant thermophysical properties (specific heat capacity, thermal conductivity),
- and constant density across both phases.

The first simplification results in a neglect of convective movement of liquid PCM, which reduces the heat transfer in the liquid phase of the PCM. In addition, the constraint of isotropic heat conduction prevents the modeling of fins to enhance heat transfer. To compensate for these simplifications, the thermal conductivities of the liquid and solid PCM can be increased. Details on estimating the increased thermal conductivities are presented in Chapter 4.3.3.

Model set-up and computational domain

The basic model of Alexiades and Solomon [5, Chapter 4] is extended to the two-dimensional, cylindrically symmetrical case. Additionally, convective heat transfer between the working fluid and the PCM is implemented. The geometrical layout of the model (Figure 4.4) is similar to the layout of the model of the sensible heat thermal energy storage presented in Chapter 4.2. The pipe containing the working fluid is surrounded by a cylindrical shell of PCM. For a cylindrically symmetrical calculation a rectangular grid is applied which is equidistantly spaced in radial as well as longitudinal direction. However, the constant spacing does not have to be equal in both directions. Starting at $r = 0$, the first longitudinal row of grid cells is used for calculating the working fluid while all other grid cells are used for calculating the PCM.

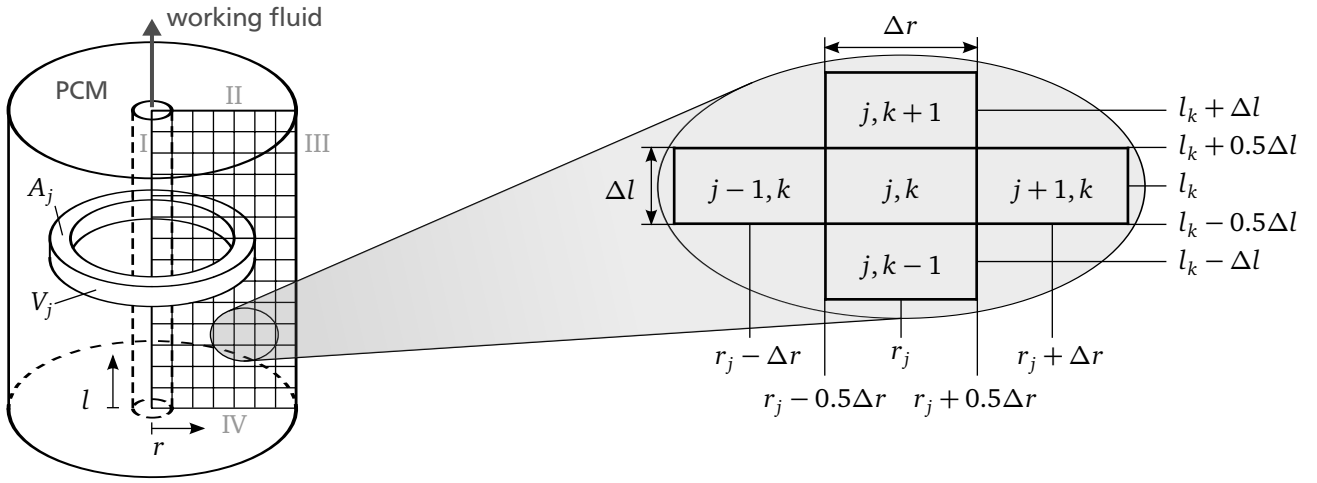

Figure 4.4: Layout of the latent heat TES model: the pipe conducting the working fluid is surrounded by a cylindrical coating of PCM. A representation of the rectangular grid for a cylindrically symmetrical calculation is depicted, including an enlarged sample section of grid cells. Roman numerals label the grid boundaries, the conditions of which are summarized in Table 4.3.

Equation system for PCM

Applying a finite differences approach and evaluating the time step $\Delta\tau^n = \tau^{n+1} - \tau^n$, the first law of thermodynamics for a grid cell j,k located inside the PCM computational grid (Figure 4.4) becomes

$$V(r_j,l_k)\rho(r_j,l_k)[en(r_j,l_k,\tau^{n+1}) - en(r_j,l_k,\tau^n)] = Q(r_j-0.5\Delta r,l_k,\tau^{n+\theta}) + Q(r_j+0.5\Delta r,l_k,\tau^{n+\theta}) + Q(r_j,l_k-0.5\Delta l,\tau^{n+\theta}) + Q(r_j,l_k+0.5\Delta l,\tau^{n+\theta}). \tag{4.28a}$$

Volume, density, and specific thermal energy of the grid cell are denoted by V, ρ, and en, respectively. The amounts of heat transfered across the boundaries of the grid cell during the time step $\Delta\tau^n$ are given by Q. Location and dimensions of the grid cell are specified by r_j, l_k, Δr, and Δl. For the previous time τ^n the temperature and energy distributions are known; for the current time τ^{n+1} temperature and energy distributions are to be calculated. To enhance the readability of equations, the local and temporal dependencies are expressed according to the following notation

$$en(r_j,l_k,\tau^{n+1}) = en_{j,k}^{n+1},$$

which simplifies Equation (4.28a) to

$$V_{j,k}\,\rho_{j,k}\left[en_{j,k}^{n+1} - en_{j,k}^{n}\right] = Q_{j-0.5,k}^{n+\theta} + Q_{j+0.5,k}^{n+\theta} + Q_{j,k-0.5}^{n+\theta} + Q_{j,k+0.5}^{n+\theta}. \tag{4.28b}$$

The different amounts of heat Q entering the grid cell j,k from the surrounding cells are each approximated by multiplying the time step $\Delta\tau^n$ with the heat flow $\dot{Q}$. Substituting the heat flow with the local temperature difference ΔT and thermal resistance R yields

$$Q^{n+\theta} = \Delta\tau^n\,\dot{Q}^{n+\theta} = \Delta\tau^n\,\frac{\Delta T^{n+\theta}}{R}. \tag{4.29}$$

The local temperature difference $\Delta T(\tau^{n+\theta}) = \Delta T^{n+\theta}$ and hence the heat flow $\dot{Q}(\tau^{n+\theta}) = \dot{Q}^{n+\theta}$ are evaluated at the intermediate time

$$\tau^{n+\theta} = \tau^n + \theta\Delta\tau^n = \tau^n + \theta(\tau_{n+1} - \tau_n) = (1-\theta)\tau^n + \theta\tau^{n+1} \quad \forall\ \theta \in [0,1]. \tag{4.30}$$

Consequently, the temperatures $T^{n+\theta} = T(\tau^{n+\theta})$ at the intermediate time are defined as

$$T^{n+\theta} = (1-\theta)T^n + \theta T^{n+1} \quad \forall\ \theta \in [0,1]. \tag{4.31}$$

By specifying the intermediate time, the parameter θ influences the applicable solution method. For $\theta = 0$ the heat flow is evaluated based on the already known temperatures at the previous time τ^n. This explicit method simplifies the calculation procedure but may lead to instabilities and wrong results if the time step $\Delta\tau$ is chosen too large. For $\theta > 0$ the heat flow is evaluated based on temperatures at the intermediate time as defined in Equation (4.30). This results in an implicit method of higher stability at the expense of having to solve a linear system of equations in the calculation procedure. The stability of the method increases with θ. For $\theta = 1$ the heat flow is evaluated based on the temperatures at the current time τ^{n+1} which yields a fully implicit and unconditionally stable method [5, Chapter 4.1.F]. Choosing $\theta = 0.5$ results in the Crank-Nicolson method, for which the order of the error is related quadratically to the orders of time and length scale. For all other methods with $\theta \neq 0.5$, the order of the error is related linearly to the order of time scale and quadratically to the order of length scale [5, Chapter 4.1.F].

The local temperature differences and thermal resistances define the amounts of heat Q transferred across the boundaries of the grid cell per time step $\Delta\tau^n$ (Equation (4.28)) as follows

$$Q^{n+\theta}_{j-0.5,k} = \Delta\tau^n \frac{T^{n+\theta}_{j-1,k} - T^{n+\theta}_{j,k}}{R_{j-0.5,k}}, \quad \text{with} \quad R_{j-0.5,k} = \frac{\ln\frac{r_j}{r_j - 0.5\Delta r}}{2\pi\lambda_{j,k}\Delta l} + \frac{\ln\frac{r_j - 0.5\Delta r}{r_{j-1}}}{2\pi\lambda_{j-1,k}\Delta l}, \tag{4.32}$$

$$Q^{n+\theta}_{j+0.5,k} = \Delta\tau^n \frac{T^{n+\theta}_{j+1,k} - T^{n+\theta}_{j,k}}{R_{j+0.5,k}}, \quad \text{with} \quad R_{j+0.5,k} = \frac{\ln\frac{r_j + 0.5\Delta r}{r_j}}{2\pi\lambda_{j,k}\Delta l} + \frac{\ln\frac{r_{j+1}}{r_j + 0.5\Delta r}}{2\pi\lambda_{j+1,k}\Delta l}, \tag{4.33}$$

$$Q^{n+\theta}_{j,k-0.5} = \Delta\tau^n \frac{T^{n+\theta}_{j,k-1} - T^{n+\theta}_{j,k}}{R_{j,k-0.5}}, \quad \text{with} \quad R_{j,k-0.5} = \frac{0.5\Delta l}{\lambda_{j,k}A_j} + \frac{0.5\Delta l}{\lambda_{j,k-1}A_j}, \tag{4.34}$$

$$Q^{n+\theta}_{j,k+0.5} = \Delta\tau^n \frac{T^{n+\theta}_{j,k+1} - T^{n+\theta}_{j,k}}{R_{j,k+0.5}}, \quad \text{with} \quad R_{j,k+0.5} = \frac{0.5\Delta l}{\lambda_{j,k}A_j} + \frac{0.5\Delta l}{\lambda_{j,k+1}A_j}. \tag{4.35}$$

The thermal conductivity of the grid cell is denoted by $\lambda_{j,k}$. A_j describes the top surface of the three-dimensional volume V_j corresponding to the rotationally symmetric extrusion of a two-dimensional grid cell (Figure 4.4). Both quantities can be calculated as follows

$$A_j = 2\pi r_j \Delta r, \tag{4.36}$$

$$V_j = A_j \Delta l. \tag{4.37}$$

Substituting the amounts of heat by Equations (4.32) to (4.35) and evaluating temperatures according to Equation (4.31), the first law of thermodynamics for a grid cell j,k (Equation (4.28)) becomes

$$\frac{V_{j,k}\,\rho_{j,k}}{\Delta\tau^n} en_{j,k}^{n+1} + B_{j,k}^n\, T_{j,k}^{n+1} = G_{j,k}^n, \tag{4.38a}$$

with

$$B_{j,k}^n = \theta \left(\frac{1}{R_{j-0.5,k}} + \frac{1}{R_{j+0.5,k}} + \frac{1}{R_{j,k-0.5}} + \frac{1}{R_{j,k+0.5}} \right), \tag{4.38b}$$

and

$$\begin{aligned} G_{j,k}^n = {} & \frac{V_{j,k}\,\rho_{j,k}}{\Delta\tau^n} en_{j,k}^n + \theta \left(\frac{1}{R_{j-0.5,k}} T_{j-1,k}^{n+1} + \frac{1}{R_{j+0.5,k}} T_{j+1,k}^{n+1} + \frac{1}{R_{j,k-0.5}} T_{j,k-1}^{n+1} + \frac{1}{R_{j,k+0.5}} T_{j,k+1}^{n+1} \right) \\ & + (1-\theta) \left[\frac{1}{R_{j-0.5,k}} T_{j-1,k}^{n} + \frac{1}{R_{j+0.5,k}} T_{j+1,k}^{n} + \frac{1}{R_{j,k-0.5}} T_{j,k-1}^{n} + \frac{1}{R_{j,k+0.5}} T_{j,k+1}^{n} \right. \\ & \left. - \left(\frac{1}{R_{j-0.5,k}} + \frac{1}{R_{j+0.5,k}} + \frac{1}{R_{j,k-0.5}} + \frac{1}{R_{j,k+0.5}} \right) T_{j,k}^n \right]. \end{aligned} \tag{4.38c}$$

Via the thermal conductivity $\lambda_{j,k}$ in the thermal resistances R, the coefficient $B_{j,k}^n$ depends on the temperature $T_{j,k}^n$ and therefore varies with time.

To keep the numerical calculation as simple as possible, it is appropriate to redefine the temperature scale applied in the latent heat TES so that the phase change occurs at $T = 0$

$$T_{j,k} = T_{j,k,\text{real}} - T_{\text{PC}}. \tag{4.39}$$

Consequently, the PCM in a grid cell is completely solid for all temperatures $T < 0$ and completely liquid for all temperatures $T > 0$. Based on this definition the specific internal energy of the PCM in a grid cell is defined as

$$\begin{aligned} \text{PCM solid:} \quad & en = c_\text{s}\, T && \forall T < 0 \\ \text{PCM liquid:} \quad & en = c_\text{l}\, T + \Delta h_\text{f} && \forall T > 0 \\ \text{PCM mushy:} \quad & 0 \le en \le \Delta h_\text{f} && \forall T = 0, \end{aligned} \tag{4.40}$$

with c_s, c_l, and Δh_f being the mass-specific heat capacity of the solid PCM, the mass-specific heat capacity of the liquid PCM, and the mass-specific enthalpy of fusion, respectively. All values are provided as constants. According to the phase of the PCM, the thermal conductivity assigned to a grid cell can assume three discrete values. The thermal conductivity of a grid cell filled with mushy PCM depends on the shape of the phase change front. As this shape is difficult to determine, Alexiades and Solomon [5, Chapter 4.3.B] suggested to choose the average of the solid and liquid thermal conductivity.

$$\begin{aligned} \text{PCM solid:} \quad & \lambda = \lambda_\text{s} && \forall T < 0 \\ \text{PCM liquid:} \quad & \lambda = \lambda_\text{l} && \forall T > 0 \\ \text{PCM mushy:} \quad & \lambda = 0.5\left(\lambda_\text{s} + \lambda_\text{l}\right) && \forall T = 0 \end{aligned} \tag{4.41}$$

Evaluating Equation (4.38) for each grid cell of the two-dimensional grid (Figure 4.4) under consideration of Equations (4.39) to (4.41) results in a system of non-linear equations for the unknown temperatures $T_{j,k}^{n+1}$ of the current time τ^{n+1}.

Numerical solution for PCM grid cells

The system of non-linear equations derived in the preceding section (Equations (4.38) to (4.41)) is numerically solved by applying a SOR algorithm [109, Chapter 17.5; also in 110, Chapter 20.5.1]. SOR stands for Successive OverRelaxation and constitutes a Gauß-Seidel method accelerated by overrelaxation. This algorithm is well suited for the presented problem. It provides considerable performance in efficiently solving sparsely filled systems of equations [109, Chapter 17.5], as resulting from heat conduction problems. In addition, this algorithm can be implemented with reasonable programming effort [109, Chapter 17.5], which is important for its adaption in a Kernel Scripting component.

Press et al. [109, Chapter 17.5] suggested the implementation of Chebyshev acceleration to speed up the solution algorithm. However, comparative calculations show an equal performance of the models with and without Chebyshev acceleration. Therefore, Chebyshev acceleration is not included in the solution algorithm of the model for the latent heat TES system.

The framework of the enthalpy method used to calculate the temperature and energy distribution ($T_{j,k}^{n+1}$, $en_{j,k}^{n+1}$) of the current time τ^{n+1} in the latent heat TES is depicted in the flowchart in Figure 4.5. The SOR enthalpy method, which is embedded in this framework, solves the system of non-linear Equations (4.38) to (4.41) numerically. The numerical solution requires the repeated evaluation of these equations in successive iteration loops. Therefore, an iteration loop based on the counter p is introduced, which replaces the time step superscript n in Equation (4.38). Details of the SOR enthalpy method are depicted in the flowchart in Figure 4.6.

In accordance with the method chosen, the change in temperature per PCM grid cell is augmented by successive overrelaxation. For enhanced convergence the relaxation factor $\omega_{\mathrm{SOR}} > 1$ is adjusted each iteration loop p as suggested by Press et al. [109, Chapter 17.5].

During a single iteration loop p, updated values for the temperature and specific internal energy of the PCM are calculated successively for each grid cell j,k. The corresponding variables ($T_{j,k}^{n+1}$, $en_{j,k}^{n+1}$) are updated immediately. Consequently, grid cells that are calculated later in the (grid) sequence benefit from updated values in grid cells that are calculated earlier in the (grid) sequence. Per grid cell, the change in specific internal energy between the current iteration loop p and the previous iteration loop $p-1$ is calculated. As soon as the maximal change, evaluated over all grid cells, falls below a predefined tolerance, the iteration is stopped, finishing the calculation of the current time τ^{n+1}.

Numerical solution for working fluid grid cells

The latent heat TES is charged and discharged by working fluid, which flows at a mass flow $\dot{M}_{\mathrm{fluid}}$ through a pipe being placed in the middle of the cylindrical storage segment. Starting at $r = 0$, the first longitudinal row of grid cells (index $j = 0$) is used for calculating the working fluid while all other grid cells are used for calculating the PCM (Figure 4.4).

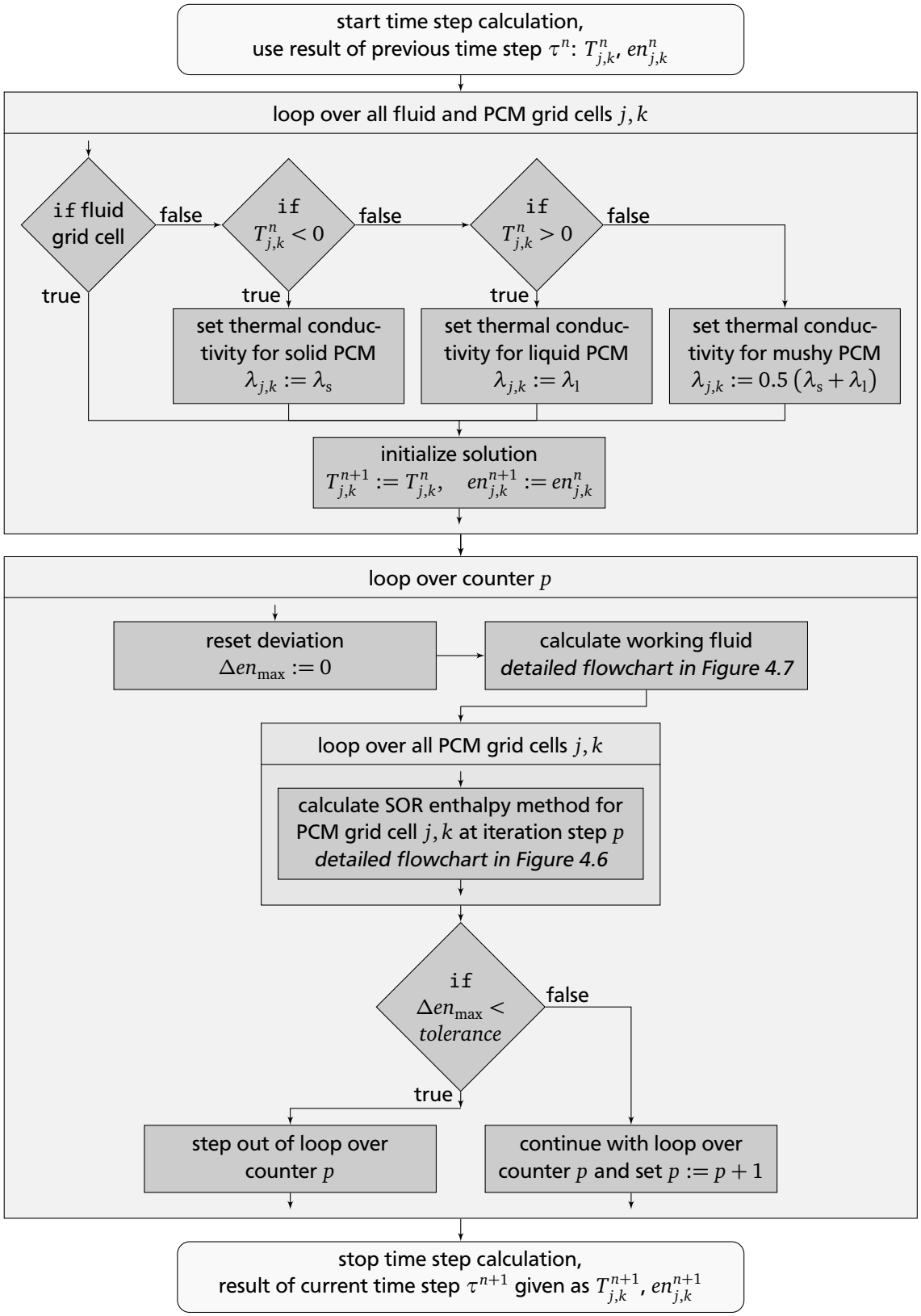

Figure 4.5: Flowchart depicting the framework of the enthalpy method used to calculate the temperature and energy distribution in the latent heat TES. Flowcharts of the embedded SOR enthalpy method and the working fluid calculation are depicted in Figures 4.6 and 4.7, respectively.

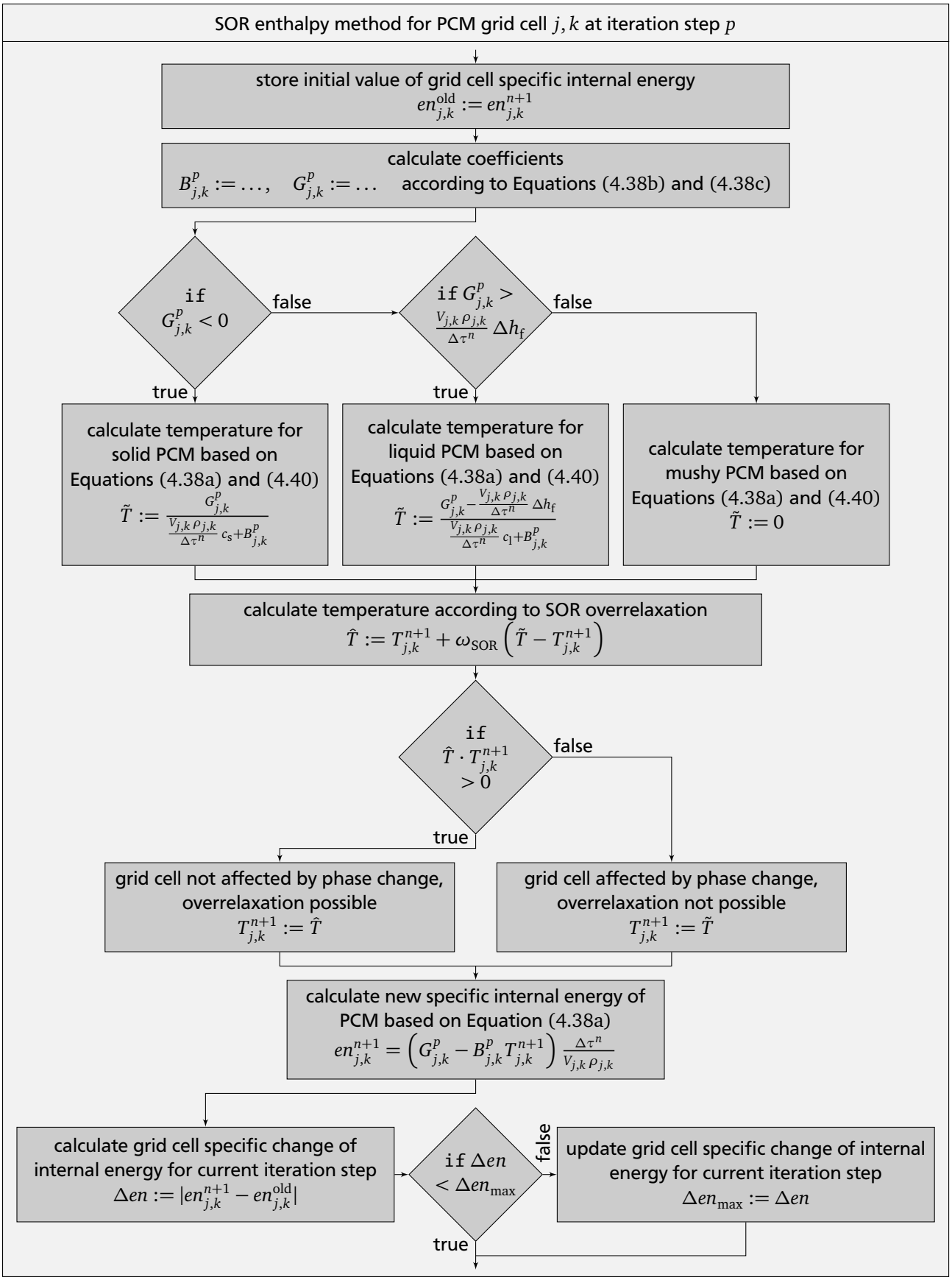

Figure 4.6: Detailed flowchart of the SOR enthalpy method for all PCM grid cells. The flowchart of the superordinate framework is depicted in Figure 4.5.

The energy transfer between working fluid and PCM is incorporated by solving an energy equation for each grid cell filled with working fluid

$$\underbrace{\left(h_{0,k}^{n+1} - \frac{p_{0,k}^{n+1}}{\rho_{0,k}^{n+1}} - h_{0,k}^{n} + \frac{p_{0,k}^{n}}{\rho_{0,k}^{n}}\right) M_{\text{fluid},k}}_{\text{(a)}} = \underbrace{\dot{M}_{\text{fluid}} \Delta\tau^{n} \left(h_{0,k-1}^{n+\theta} - h_{0,k}^{n+\theta}\right)}_{\text{(b)}} + \underbrace{\frac{\Delta\tau^{n}}{R_{0.5,k}} \left(T_{1,k}^{n+\theta} - T_{0,k}^{n+\theta}\right)}_{\text{(c)}}. \quad (4.42)$$

Mass-specific enthalpy, pressure, density and mass of the working fluid within grid cell $0,k$ are denoted by $h_{0,k}$, $p_{0,k}$, $\rho_{0,k}$, and $M_{\text{fluid},k}$. The change in internal energy of the grid cell (a) is caused by working fluid entering and leaving the grid cell (b), and by heat transfer between the working fluid and the adjacent PCM (c). This heat transfer is driven by the temperature difference between working fluid and PCM and has to overcome the thermal resistance $R_{0.5,k}$ due to convection and conduction. As resistance due to conduction, the pipe surrounding the working fluid and the PCM have to be considered.

Simulations show that the change in internal energy of a grid cell filled with working fluid is negligible in comparison to the change in internal energy of a grid cell filled with PCM. Consequently, the change in internal energy of a working fluid grid cell has no significant effect on the calculation result and is neglected, yielding the simplified working fluid energy equation

$$0 = \dot{M}_{\text{fluid}} \left(h_{0,k-1}^{n+\theta} - h_{0,k}^{n+\theta}\right) + \frac{1}{R_{0.5,k}} \left(T_{1,k}^{n+\theta} - T_{0,k}^{n+\theta}\right). \quad (4.43)$$

The mass-specific enthalpy of the working fluid entering the current grid cell from the adjacent grid cell in upstream direction is denoted by $h_{0,k-1}^{n+\theta}$. The mass-specific enthalpy of the working fluid entering the model is provided as boundary condition. Evaluating the mass-specific enthalpies and temperatures at the intermediate time $\tau^{n+\theta}$ (Equations (4.30) and (4.31)) and rearranging Equation (4.43) results in the mass-specific enthalpy of the fluid leaving grid cell $0,k$

$$h_{0,k}^{n+1} = h_{0,k-1}^{n+1} + \frac{1-\theta}{\theta} \left(h_{0,k-1}^{n} - h_{0,k}^{n}\right) + \frac{1}{R_{0.5,k}\dot{M}_{\text{fluid}}} \left[T_{1,k}^{n+1} - T_{0,k}^{n+1} + \frac{1-\theta}{\theta} \left(T_{1,k}^{n} - T_{0,k}^{n}\right)\right]. \quad (4.44)$$

The numerical solution of Equation (4.44) for all working fluid grid cells is embedded in the framework of the enthalpy method (Figure 4.5). Also enclosed in the iteration loop p, the calculation of the working fluid grid cells takes place just before the SOR enthalpy method for all PCM grid cells is called. A flowchart illustrating the calculation of the working fluid grid cells is depicted in Figure 4.7.

Specifics of the calculation of the working fluid grid cells are described in the following. Especially for small working fluid mass flows $\dot{M}_{\text{fluid}}$ incorporating an underrelaxation of the working fluid enthalpy in the calculation procedure is necessary. Without underrelaxation, oscillations might arise which can prevent the solution from converging. The relaxation factor has to be adjusted in the range of $0 < \omega_{\text{fluid}} < 1$ based on the PCM properties in the model as well as type and mass flow of the working fluid. As starting value for the adjustment, a relaxation factor of $\omega_{\text{fluid}} = 0.5$ shows good results.

To determine the temperature of the working fluid based on a database query, in addition to the specific enthalpy the pressure of the working fluid needs to be known for each working fluid grid cell. The pressure of the working fluid entering the latent heat TES and the pressure drop within the TES are provided as input values to the model. The pressure drop is linearly distributed over all fluid grid cells.

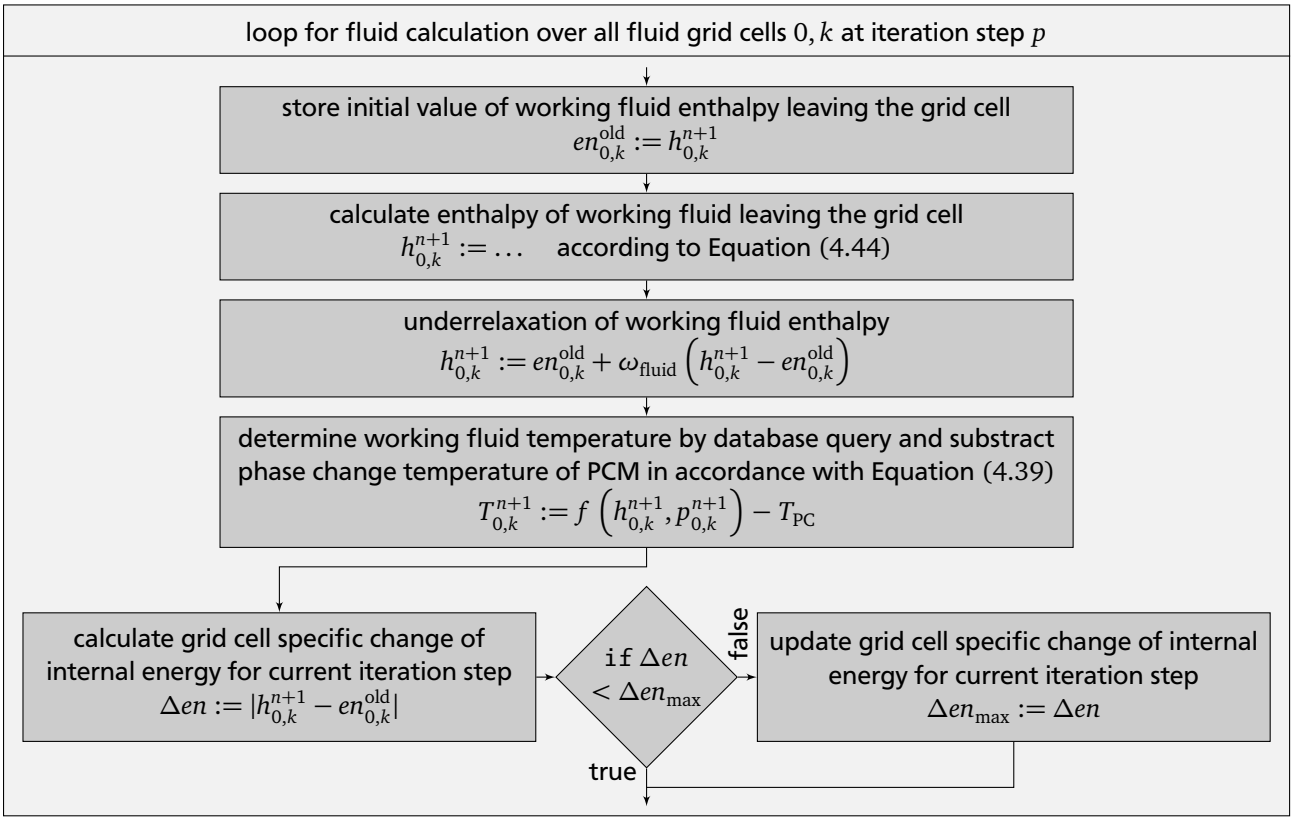

Figure 4.7: Detailed flowchart of the working fluid grid cell calculation. The flowchart of the superordinate framework is depicted in Figure 4.5.

Boundary conditions

The rectangular computational domain is enclosed by four boundaries, which are labeled with Roman numerals in Figure 4.4. In Table 4.3 the corresponding boundary conditions are summarized. For all third-type boundary conditions, the ambient temperature and the thermal resistances are provided as model input parameters. The thermal resistances are each composed of two parts, one thermal resistance due to conduction through the storage insulation and one thermal resistance due to convection between the insulation boundary and the ambient air.

Table 4.3: Summary of boundary conditions of the rectangular computational domain. Roman numerals label the boundaries depicted in Figure 4.4.

label	boundary condition
I	second-type boundary condition with zero normal heat flux (symmetry boundary condition)
II, III, IV	third-type boundary condition (convective boundary condition)

Heat convection between working fluid and surrounding pipe, and heat conduction through the pipe are not modeled within the latent heat TES. Instead, the thermal resistance due to convection and conduction

$$R_{\alpha,\lambda} = \frac{1}{\alpha_{\text{fluid}} 2\pi l_{\text{M}}} + \frac{\ln {}^{r_{\text{o}}}/_{r_{\text{i}}}}{\lambda_{\text{pipe}} 2\pi l_{\text{M}}} \tag{4.45}$$

needs to be provided as model input. The inner and outer radius of the pipe, its thermal conductivity and its length considered in the model are denoted by r_{i}, r_{o}, λ_{pipe}, and l_{M}, respectively. The global convective heat transfer coefficient α_{fluid} between working fluid and surrounding pipe is estimated through the Nusselt correlation for turbulent pipe flow [35]

$$\alpha_{\text{fluid}} = \frac{\lambda_{\text{fluid}}}{2r_{\text{i}}} Nu_{\text{fluid}} = \frac{\lambda_{\text{fluid}}}{2r_{\text{i}}} \frac{(\xi_\alpha/8) Re_{\text{fluid}} Pr_{\text{fluid}}}{1 + 12.7\sqrt{\xi_\alpha/8}\left(Pr_{\text{fluid}}^{2/3} - 1\right)} \left[1 + \left(\frac{2\,r_{\text{i}}}{l_{\text{M}}}\right)^{2/3}\right], \tag{4.46}$$

with

$$Re_{\text{fluid}} = \frac{u_{\text{fluid}} 2r_{\text{i}}}{\nu_{\text{fluid}}}, \tag{4.47}$$

$$\xi_\alpha = \left(1.8 \log_{10}(Re_{\text{fluid}}) - 1.5\right)^{-2}. \tag{4.48}$$

Nusselt, Reynolds, and Prandtl number of the fluid and its thermal conductivity are expressed by Nu_{fluid}, Re_{fluid}, Pr_{fluid}, and λ_{fluid}.

The nominal pressure drop experienced by the working fluid due to its passage through the pipes of the latent heat TES is estimated for turbulent flow through rough pipes [64]

$$\Delta p_{\text{TES,N}} = \xi_p \frac{l_{\text{R}}}{2r_{\text{i}}} \frac{\rho_{\text{fluid}} u_{\text{fluid}}^2}{2}, \tag{4.49}$$

with the drag coefficient ξ_p

$$\frac{1}{\sqrt{\xi_p}} = 2 \log_{10}\left(\frac{2r_{\text{i}}}{k}\right) + 1.14. \tag{4.50}$$

The absolute roughness within the pipe, stemming from the pipe itself and from fouling, is denoted by k. For fouled steel pipes, the absolute roughness is in the range of $1\,\text{mm} \leq k \leq 4\,\text{mm}$ [64]. Based on the actual $\dot{M}_{\text{fluid}}$ and nominal $\dot{M}_{\text{fluid,N}}$ working fluid mass flow through the pipes of the TES system (Equation (4.27)), the actual pressure drop Δp_{TES} is given by Equation (4.26).

The working fluid experiences a phase change during its passage trough the pipes of the latent heat TES system, which significantly changes the local convective heat transfer coefficient and local pressure drop. To account for these changes, the global heat transfer coefficients and total nominal pressure drops are determined for the inlet and for the outlet flow conditions. Finally, the corresponding mean values are used by the model.

Due to the low thermal conductivity of most phase change materials, heat transfer enhancement techniques are often applied (Chapter 2.6.2). Fins or structures of high thermal conductivity materials, that

are immersed in the PCM, are not modeled. The computational domain (Figure 4.4) is exclusively composed of PCM. To account for heat transfer enhancement techniques, the thermal conductivities used by the latent heat TES model are increased. PCM and heat transfer enhancement structures can be considered as a combination of thermal resistances. The type of combination depends on the geometrical arrangement. The parallel arrangement results in the lowest possible thermal resistance and the highest effective thermal conductivity $\lambda_{\mathrm{eff,parallel}}$. In contrast, the series arrangement results in the highest possible thermal resistance and the lowest effective thermal conductivity $\lambda_{\mathrm{eff,series}}$. In general, the increased thermal conductivities $\lambda_{\mathrm{s,M}}$ and $\lambda_{\mathrm{l,M}}$ employed by the model are given by a combination of the parallel and serial arrangement of the effective thermal conductivities

$$\lambda_{\mathrm{s,M}} = g\lambda_{\mathrm{s,eff,parallel}} + (1-g)\lambda_{\mathrm{s,eff,series}}, \tag{4.51a}$$

$$\lambda_{\mathrm{l,M}} = g\lambda_{\mathrm{l,eff,parallel}} + (1-g)\lambda_{\mathrm{l,eff,series}}. \tag{4.51b}$$

The geometry factor g that can attain values in the range of $0 < g < 1$, accounts for the geometrical integration of the fins or heat transfer enhancement structures into the PCM.

The most exact estimation of the geometry factor can be determined by matching the simulation results of the latent heat TES model with operational data of real latent heat TES systems. If operational data is not available, complete numerical simulations [54; 117] or analytical approaches can be employed to estimate the increased thermal conductivities.

Accounting for heat transfer enhancement techniques by increased thermal conductivities of the PCM presents a good compromise between simulation accuracy and computational effort. The applicability of this approach and the calculation of the effective thermal conductivities are demonstrated in the third part of the following validation.

4.3.3 Validation

The simulation of the latent heat TES is validated through comparisons with analytical solutions and experimental data. Analytical solutions are used to validate the simulation of transient heat conduction with and without phase change within the phase change material. Experimental data is employed to validate the simulation of fluid and storage temperatures during charging and discharging operation.

Transient heat conduction without phase change

For comparison with analytical solutions, one-dimensional heat conduction is calculated separately in radial and longitudinal direction on the two-dimensional grid depicted in Figure 4.4. Dimensions of the computational grid and material properties of the chosen storage material water are summarized in Table 4.4. In accordance with the simplifications presented at the beginning of Chapter 4.3.2, water density is assumed to stay constant, which yields the neglect of convective effects. At the beginning of

Table 4.4: Dimensions and material properties of the transient heat conduction simulation used for verification of the latent heat TES.

l_{min}	l_{max}	r_{min}	r_{max}	T_{init}	$T_{\mathrm{IV/I}}$	c_{l}	λ_{l}	ρ
0	4 cm	1 cm	5 cm	10 °C	50 °C	4186.8 J (kg K)$^{-1}$	0.564 W (m K)$^{-1}$	1000 kg m^{-3}

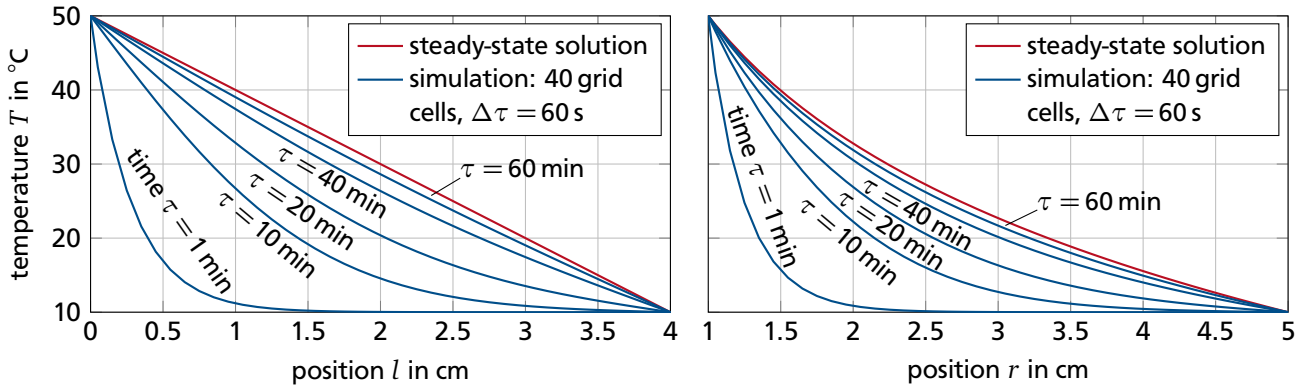

Figure 4.8: Temperature distributions at fixed times approaching the steady-state heat conduction solution. The left graph is based on heat conduction in longitudinal direction, the right graph is based on heat conduction in radial direction.

the calculation, boundary IV (longitudinal heat conduction) or boundary I (radial heat conduction) are subject to a temperature jump from initial temperature $T_{\text{init}} = 10\,°\text{C}$ to $T_{\text{VI/I}} = 50\,°\text{C}$. The remaining boundaries are kept adiabatic (Figure 4.4). The temperature distributions inside the TES at fixed times and the analytical steady-state solution are depicted in Figure 4.8. With advancing time, the simulated temperature distribution converges to the analytical steady-state solution. Consequently, the simulation of transient heat conduction without phase change is validated. The validation of the temperature distributions at each time step is presented in the following section.

Transient heat conduction with phase change

A transient, one-dimensional melting process in longitudinal direction is calculated on the two-dimensional grid depicted in Figure 4.4. At the beginning of the calculation, boundary IV is subject to a temperature jump from melting temperature ($T_{\text{PC}} = 0\,°\text{C}$) to $T_{\text{IV}} = 25\,°\text{C}$. All other boundaries are kept adiabatic. As long as the melting front does not reach boundary II, the problem can be considered as semi infinite in the longitudinal direction. This problem is also referred to as one-dimensional Stefan problem and is described in more detail in [5, Chapters 2.1.A and 2.1.E]. An analytical solution exists, if the computational domain is initialized under the condition of being entirely solid at melting temperature.

The derivation of the analytical solution is described in detail in [5, Chapter 2.1.B] yielding the position of the melt front

$$l_{\text{PC}}(\tau) = 2\delta\sqrt{\tau\frac{\lambda_{\text{l}}}{\rho c_{\text{l}}}} \tag{4.52}$$

and the time and position dependent temperature of the phase change material

$$T(l,\tau) = \begin{cases} T_{\text{IV}} - (T_{\text{IV}} - T_{\text{PC}})\frac{\operatorname{erf}\left(\delta\frac{l}{l_{\text{PC}}(\tau)}\right)}{\operatorname{erf}(\delta)} & \forall l < l_{\text{PC}}(\tau) \\ T_{\text{PC}} & \forall l \geq l_{\text{PC}}(\tau) \end{cases}. \tag{4.53}$$

Table 4.5: Dimensions, material properties, and characteristic numbers of the one-dimensional melting process used for verification of the latent heat TES.

$l_{\min}$	$l_{\max}$	$r_{\min}$	$r_{\max}$	T_{IV}	T_{PC}	c_{l}	λ_{l}	ρ	St	δ
0	4 cm	1 m	1.1 m	25 °C	0 °C	4186.8 J (kg K)$^{-1}$	0.564 W (m K)$^{-1}$	1000 kg m^{-3}	0.3139	0.3776

The variable δ is the solution of the transcendental equation

$$\delta e^{\delta^2} \operatorname{erf}(\delta) = \frac{St}{\sqrt{\pi}}, \tag{4.54}$$

with St being the Stefan number, the problem dependent ratio of sensible to latent heat

$$St = \frac{c_{\mathrm{l}} \left(T_{\mathrm{IV}} - T_{\mathrm{PC}} \right)}{\Delta h_{\mathrm{f}}}. \tag{4.55}$$

For the melting problem at hand the Stefan number is positive, so Equation (4.54) has a unique solution. In Table 4.5 the corresponding dimensions, properties, and characteristic numbers are summarized. In accordance with the simplifications presented at the beginning of Chapter 4.3.2, water density is assumed to stay constant, which yields the neglect of convective effects.

Before the simulations of the one-dimensional Stefan problem are evaluated, some general remarks on the plots presented in Figures 4.9 to 4.11 shall be mentioned. The simulation run times given are achieved with a standard, state-of-the-art desktop computer that uses a single CPU for the simulation. These run times are intended for relative, not for absolute comparisons. The amount of grid cells refers to the amount of grid cells distributed in the longitudinal direction. All graphs contain lines of two different types. If lines of only one type are visible, the lines of both types lie on top of each other.

In Figure 4.9 the position of the melt front simulated for different spatial and temporal discretizations is compared to the analytical solution. With finer spatial discretization, the deviation between the simulated and the analytical solution decreases, but the run time of the simulation increases. It is shown in the lower right graph that for the same spatial discretization, increasing the temporal discretization by reducing the time step, does hardly improve the simulation results. In summary, the simulation results are in very good agreement with the analytical solution.

The comparison of the simulated temporal temperature distribution at fixed positions to the analytical solution is depicted in Figure 4.10. In Figure 4.11 the comparison of the simulated spatial temperature distribution at fixed times to the analytical solution is plotted. In both figures, even for the roughest spatial discretization, a very good agreement between the simulated and the analytical solutions is achieved. The simulation results for a finer temporal discretization are not shown because result accuracy does hardly improve while simulation run time rises significantly.

It can be concluded that even for the roughest spatial discretization of 40 elements in longitudinal direction, simulation and analytical results are in very good agreement. Due to the vanishing increase of accuracy paired with a significant increase in run time, a finer temporal discretization is not favorable. In summary, the simulation of transient heat conduction including phase change is validated.

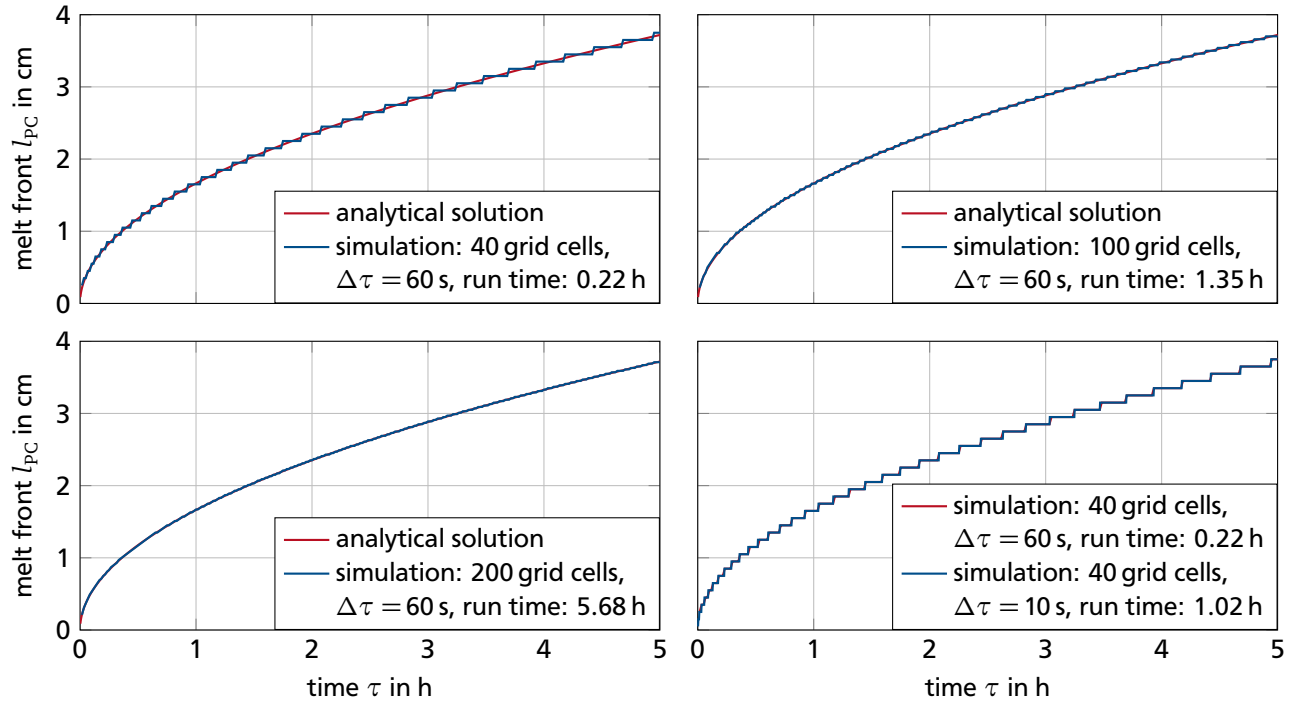

Figure 4.9: Comparison of melt front over time for the one-dimensional Stefan problem.

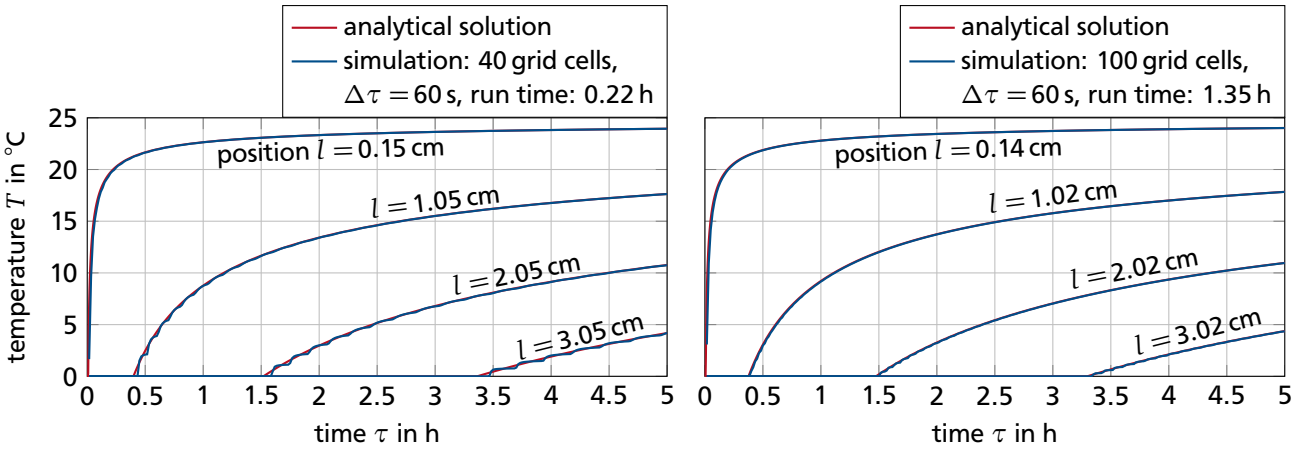

Figure 4.10: Comparison of the temperature distributions at fixed positions over time for the one-dimensional Stefan problem.

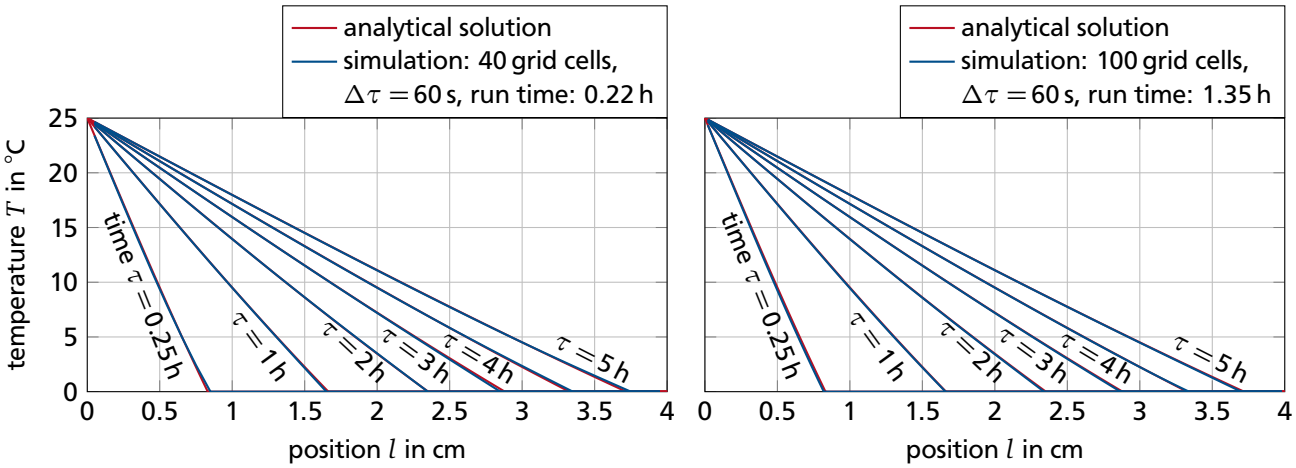

Figure 4.11: Comparison of the spatial temperature distributions at fixed times for the one-dimensional Stefan problem.

To validate the latent heat TES model, simulated working fluid and storage temperatures are compared with experimental data. As part of extensive research on latent heat TES systems at the German Aerospace Center (DLR), Laing et al. [71; 72] published experimental test results of a medium sized storage system filled with sodium nitrate ($NaNO_3$) during cyclic charging and discharging operation. The setup of the storage module is presented in Figure 4.12 and Table 4.6 [71; 72; 86; 117]. The cylindrical storage module is filled with approximately $M_{\mathrm{PCM}} = 140\,\mathrm{kg}$ of sodium nitrate which is traversed by seven heat exchanger pipes equipped with radially arranged, hexagonally shaped aluminum fins. The thermal oil Therminol VP 1 flows through the TES system at a constant mass flow of $\dot{M}_{\mathrm{fluid,R}}$.

Assuming that the charging and discharging process proceeds similar around all seven heat exchanger pipes, the rotationally symmetric computational domain (Figure 4.13) covers the PCM material around a single heat exchanger pipe, only. Model dimensions and parameters are given in Table 4.7. The outer radius of the computational domain $r_{\mathrm{fin,mean}}$ equals the radius of a circle that has the same surface area as the top surface of one hexagonally shaped fin with outer radius $r_{\mathrm{fin,max}}$. The length of the computational domain is shorter than the length of the entire storage module $l_{\mathrm{M}} < l_{\mathrm{R}}$, because the phase change material without fins is simulated. Consequently, the thermal energy storage capacity of the fins is neglected. In addition, based on the value of the thermal resistance R_{o}, heat losses to the environment are also neglected. The calculation procedures to determine the thermal resistance R_{i} between working fluid and PCM, as well as the increased thermal conductivity of solid and liquid PCM are described in

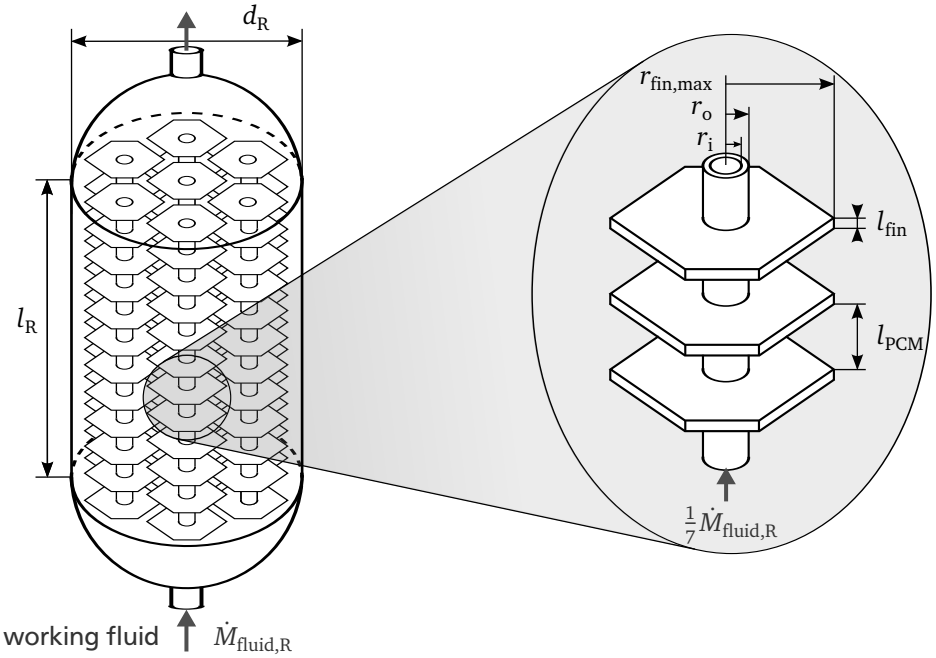

Figure 4.12: Setup of the DLR latent heat TES module [71; 72; 86; 117] filled with PCM and traversed by heat exchanger pipes with fins. The dimensions are given in Table 4.6.

Table 4.6: Dimensions of the latent heat TES module depicted in Figure 4.12.

l_{R}	d_{R}	l_{PCM}	l_{fin}	r_{i}	r_{o}	$r_{\mathrm{fin,max}}$
1365 mm	310 mm	10 mm	1 mm	5 mm	6 mm	55 mm

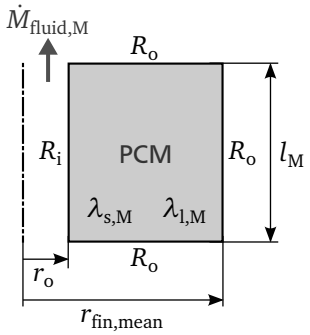

Figure 4.13: Rotationally symmetric computational domain of the latent heat TES model. Model dimensions and parameters are summarized in Table 4.7.

Table 4.7: Dimensions and parameters of the latent heat TES model depicted in Figure 4.13.

r_o	$r_{\mathrm{fin,mean}}$	l_M	R_i	R_o	$\dot{M}_{\mathrm{fluid,M}} = \frac{1}{7}\dot{M}_{\mathrm{fluid,R}}$	g	$\lambda_{\mathrm{s,M}}$	$\lambda_{\mathrm{l,M}}$
in mm		in m	in $\mathrm{K\,W^{-1}}$		in $\mathrm{kg\,s^{-1}}$	-	in $\mathrm{W\,(m\,K)^{-1}}$	
6	50	1.24	$7.674 \cdot 10^{-3}$	$1 \cdot 10^{20}$	0.1239	0.45	10.2006	10.0486

Chapter 4.3.2. For the geometrical arrangement of PCM and fins around a single pipe, the effective thermal conductivities of parallel ($\lambda_{\mathrm{eff,parallel}}$) and serial ($\lambda_{\mathrm{eff,series}}$) arrangement are given by

$$\lambda_{\mathrm{s/l,eff,parallel}} = \frac{\lambda_{\mathrm{s/l,PCM}} l_{\mathrm{PCM}} + \lambda_{\mathrm{fin}} l_{\mathrm{fin}}}{l_{\mathrm{PCM}} + l_{\mathrm{fin}}}, \tag{4.56a}$$

$$\lambda_{\mathrm{s/l,eff,series}} = \frac{l_{\mathrm{PCM}} + l_{\mathrm{fin}}}{l_{\mathrm{PCM}}/\lambda_{\mathrm{s/l,PCM}} + l_{\mathrm{fin}}/\lambda_{\mathrm{fin}}}. \tag{4.56b}$$

All thermal properties required for the parametrization of the model are summarized in Table 4.8. In the relevant pressure range, the thermal properties of Therminol VP 1 are independent of pressure. Therefore, the working fluid pressure drop across the TES system does not need to be considered.

In the experimental investigation [71; 72] the latent heat TES system is consecutively charged and discharged for 3.5 h and 2.5 h, respectively. The time-dependent development of the working fluid inlet temperature is similar for each of the consecutive charging and discharging periods. After several charging and discharging periods, also the working fluid outlet temperature and the spatially averaged PCM temperature follow a repetitive pattern. Measured by Laing at al. [71], Figure 4.14 depicts the working fluid inlet and outlet temperatures as well as the mean temperature of the PCM for a representative charging and discharging period over time. Taking the measured working fluid inlet temperature as model input, several consecutive charging and discharging cycles are simulated by the model of the latent heat TES. For a geometry factor of $g = 0.45$, best agreement is achieved between measurement and simulation results. Based on the identified geometry factor and a phase change temperature of $T_{\mathrm{PC}} = 305\,^{\circ}\mathrm{C}$ [70], the simulated temperatures of a representative charging and discharging period are also depicted in Figure 4.14. Comparing experiment and simulation shows a very good agreement of the working fluid outlet temperature distribution and a good agreement of the spatially averaged PCM temperature distribution. The deviations in PCM temperature originate primarily from the simulation of the phase change. However, at the end of the charging and discharging periods, the deviations vanish. Considering the heat transfered during charging and discharging (Table 4.9), the simulation results are in good agreement with the experimental evaluation. The maximum deviation amounts to less than 11 %.

Table 4.8: Thermal properties required for the parametrization of the latent heat TES model.

sodium nitrate [9]		Therminol VP 1 [130]		pipe with fins [101]	
T_{PC}	306 °C	T	304.5 °C	T	300 °C
Δh_f	177.5 kJ (kg)$^{-1}$	ρ	800.67 kg m^{-3}	λ^1_{steel}	18 W (m K)$^{-1}$
ρ_s	2120 kg m^{-3}	λ	93.60 · 10^{-3} W (m K)$^{-1}$	λ^2_{Al}	232 W (m K)$^{-1}$
ρ_l	1908 kg m^{-3}	c	2350 J (kg K)$^{-1}$		
λ_s	0.70 W (m K)$^{-1}$	ν	2.648 · 10^{-7} m^2 s^{-1}		
λ_l	0.55 W (m K)$^{-1}$ [152]				
c_s	1658 J (kg K)$^{-1}$				
c_l	1658 J (kg K)$^{-1}$				

[1] stainless steel, material number 1.4571
[2] aluminum alloy, material number EN AW-1200

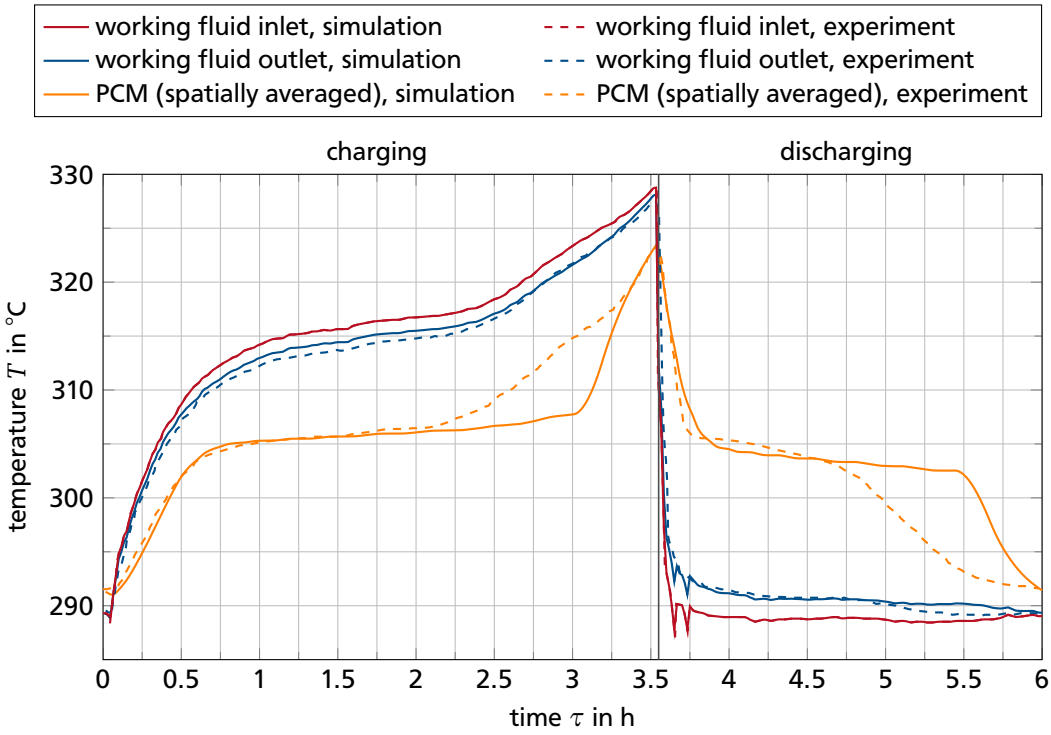

Figure 4.14: Temperature distribution during charging and discharging operation of a latent heat TES over time. Comparison of simulation results and experimental data [71].

Table 4.9: Transfered heat during charging and discharging. The simulation results are compared to values determined by Laing et al. [71] based on theoretical considerations and measured temperatures.

	simulation result	theoretical value [71]	value based on measured temperatures [71]
Q_{charge} in kWh	8.62	8.51	7.87
$Q_{discharge}$ in kWh	7.72	-	7.20

Regarding the integration of the latent heat TES model into the model of the PHES system, different deviations have different impacts. Deviations in PCM temperature are more tolerable than deviations in working fluid outlet temperature, because the working fluid outlet temperature directly influences the operation of other PHES system components.

In summary, the simulation results are in good agreement with experimental data, which successfully concludes the validation of the model for the latent heat TES. For a reliable parametrization of the latent heat TES model, especially for the determination of the increased thermal conductivities ($\lambda_{s,M}$, $\lambda_{l,M}$), experimental data or results of a complete numerical simulations are required.

4.4 Exergy, economic, and exergoeconomic analysis procedures

Energy analyses are widely applied to assess energy conversion systems. In accordance with the first law of thermodynamics, energy cannot be destroyed; it can be converted between different forms of energy only. The first law of thermodynamics does not impose any restrictions on the conversion of energy. In contrast, the second law of thermodynamics accounts for different quality levels of energy forms which result in physical limitations of energy conversion. Based on the second law of thermodynamics, an exergy analysis also considers different quality levels of energy forms and therefore should be preferably chosen over energy based analyses methods.

An exergoeconomic analysis combines the results of an exergy analysis and an economic analysis (Figure 4.15) in order to assign costs to exergies and to determine the cost distribution among the components of a system. Based on simulation results or real process data, the exergy analysis provides the exergy distribution among the components of a system. Adapted to the operation scenario analyzed, component costs and costs for input quantities are provided by the economic analysis.

Consequently, an exergoeconomic analysis accounts for energy conversion efficiency, physical limits of energy conversion, and financial costs of energy conversion. The development of exergy and exergoeconomic analysis is summarized in detail by Tsatsaronis [141]. An extensive review of the same matter is presented by Sciubba and Wall [125]. Analysis procedures adapted in this work for the exergy, economic, and exergoeconomic analysis of PHES systems are described in the following sections.

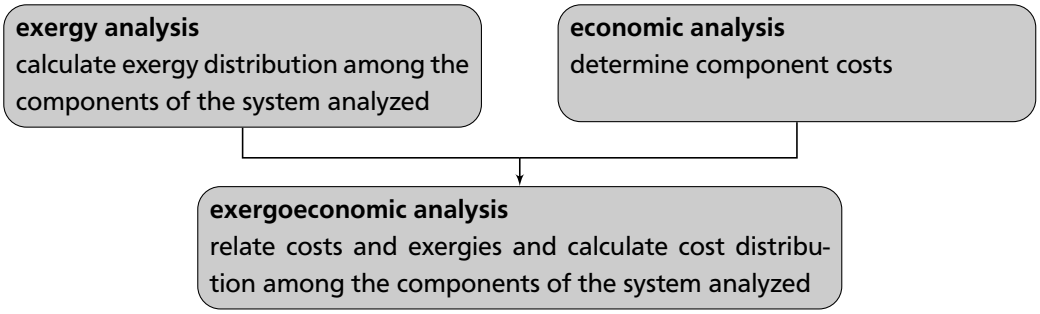

Figure 4.15: Basic principle of an exergoeconomic analysis.

4.4.1 Exergy analysis

The maximum amount of useful work can be conducted by a system, if the system is reversibly brought into equilibrium with its environment. Based on technical and etymological considerations, Rant [114] proposed the term exergy for the maximum amount of useful work in 1956, which was soon widely accepted and is commonly used these days. Several definitions, detailed introductions, and derivations

to the concept of exergy can be found in [7, Chapter 3.3; 11, Chapter 3; 134, Chapter 11]. The basic approach is described in the following.

Neglecting nuclear, magnetic, electrical, and surface tension effects [11, Chapter 3], the equilibrium with the environment is characterized in terms of physical, chemical, kinetic, and potential equilibrium. If the environment itself is not in equilibrium, contradictions to the second law of thermodynamics arise [7, Chapter 3.3]. Consequently, an exergy analysis requires the definition of an equilibrium reference environment.

Corresponding to the equilibrium conditions considered, the exergy E_{sys} of a system is composed of the four parts physical exergy E_{phy}, chemical exergy E_{ch}, kinetic exergy E_{kin}, and potential exergy E_{pot} [11, Chapter 3]

$$E_{\mathrm{sys}} = E_{\mathrm{phy}} + E_{\mathrm{ch}} + E_{\mathrm{kin}} + E_{\mathrm{pot}}. \tag{4.57}$$

Physical exergy is almost always considered in exergy analyses [7, Chapter 3.3], describing the departure from the thermodynamic equilibrium with the reference environment. For closed systems the physical exergy becomes

$$E_{\mathrm{phy}} = M\left((en - en_{\mathrm{ref}}) + p_{\mathrm{ref}}(\rho^{-1} - \rho_{\mathrm{ref}}^{-1}) - T_{\mathrm{ref}}(s - s_{\mathrm{ref}})\right), \tag{4.58}$$

with mass-specific internal energy, mass-specific entropy, density and pressure denoted by en, s, ρ, and p. The subscript ref indicates quantities of the system being in thermodynamic equilibrium with the reference environment. For open systems the physical exergy is defined as

$$E_{\mathrm{phy}} = M\left((h - h_{\mathrm{ref}}) - T_{\mathrm{ref}}(s - s_{\mathrm{ref}})\right), \tag{4.59}$$

with the mass-specific enthalpy denoted by h. Only if chemical reactions and mixing of different species are part of the process to analyze, chemical exergy varies and has to be included in an exergy analysis. As these effects are not relevant for the PHES systems considered in this work, the underlying theory is not presented here. An introduction to chemical exergies and the related concept of fuel exergies is given in [7, Chapter 3.3; 11, Chapter 3]. Rarely, the parts kinetic and potential exergy are considered in an exergy analysis [7, Chapter 3.3; 97], which are equal to the respective energies En

$$E_{\mathrm{kin}} = En_{\mathrm{kin}}, \tag{4.60}$$

$$E_{\mathrm{pot}} = En_{\mathrm{pot}}. \tag{4.61}$$

Compared to the physical exergy, kinetic and potential exergies can be neglected in the analysis of PHES systems. Consequently the exergy of a system considered in this work is composed solely of physical exergy

$$E_{\mathrm{sys}} = E_{\mathrm{phy}}. \tag{4.62}$$

Recalling the definition of exergy, it becomes clear that useful work supplied to or discharged by a system is pure exergy. Forms of work relevant in the context of PHES systems are electrical and mechanical work

$$E_{\mathrm{el}} = En_{\mathrm{el}}, \tag{4.63}$$

$$E_{\mathrm{mech}} = En_{\mathrm{mech}}. \tag{4.64}$$

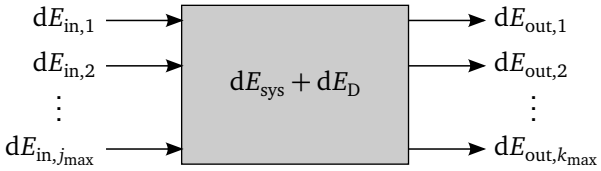

Figure 4.16: Sample system illustrating an exergy balance. The system Exergy E_{sys} depends on the exergies entering the system $E_{in,j}$, the exergies leaving the system $E_{out,k}$, and the exergy destruction within the system E_D.

Although electrical work is the thermodynamically correct term, the terminology electrical energy is almost exclusively used in technology and science. To avoid confusions, the commonly used term electrical energy is used throughout this work. The maximum amount of useful work that can be conducted by a heat Q does not only depend on the amount of heat, but also on the temperature of the heat T_Q and the temperature of the reference environment T_{ref}

$$E_Q = \left(1 - \frac{T_{ref}}{T_Q}\right) Q. \tag{4.65}$$

Exergy balances are essential parts of an exergy analysis. Considering the sample system of Figure 4.16, the corresponding exergy balance in differential form becomes

$$dE_{sys} + dE_D = \sum_{j=1}^{j_{max}} dE_{in,j} - \sum_{k=1}^{k_{max}} dE_{out,k}. \tag{4.66}$$

The system Exergy E_{sys} is increased by the exergies entering the system $E_{in,j}$ and decreased by the exergies leaving the system $E_{out,k}$. The operation of real, non-ideal systems is accompanied by an irrecoverable exergy destruction E_D. The smaller the exergy destruction, the closer comes the system to an ideal, thermodynamically reversible operation. In the limiting case of thermodynamically reversible system operation, the exergy destruction vanishes. Negative exergy destructions $E_D < 0$ are thermodynamically impossible. The exergies leaving the system could either be fueling downstream systems or they could be released to the reference environment being considered as exergy losses E_L.

The thermodynamic performance of a system cannot be evaluated solely based on exergy destruction. On the one hand, exergy destruction scales with system size. On the other hand, exergy destruction does not capture exergy losses to the environment. These effects are accounted for by the exergetic efficiency, which is defined as the ratio of product exergy E_P to fuel exergy E_F

$$\eta_{ex} = \frac{dE_P}{dE_F} = 1 - \frac{dE_D + dE_L}{dE_F}. \tag{4.67}$$

Exergetic efficiencies evaluate the operation of a system with respect to the thermodynamic optimum. Consequently they scale between zero and one and are therefore superior to energetic efficiencies.

In contrast to the exergy destruction, which is unambiguously defined by the balance Equation (4.66), exergetic efficiencies depend on the definition of product and fuel exergy. Equation (4.66) can be ex-

pressed in terms of product and fuel exergies, which in turn are functions of the system exergy and the exergies entering and leaving the system

$$\begin{aligned} \mathrm{d}E_\mathrm{D} &= \mathrm{d}E_\mathrm{F} - \mathrm{d}E_\mathrm{P} - \mathrm{d}E_\mathrm{L} \\ \mathrm{d}E_\mathrm{D} &= \mathrm{d}E_\mathrm{F}\left(\mathrm{d}E_{\mathrm{in},j}, \mathrm{d}E_{\mathrm{out},k}, \mathrm{d}E_\mathrm{sys}\right) - \mathrm{d}E_\mathrm{P}\left(\mathrm{d}E_{\mathrm{in},j}, \mathrm{d}E_{\mathrm{out},k}, \mathrm{d}E_\mathrm{sys}\right) - \mathrm{d}E_\mathrm{L}\left(\mathrm{d}E_{\mathrm{out},k}\right). \end{aligned} \tag{4.68}$$

For often analyzed systems and system components, common product and fuel definitions can be found in literature [11, Chapter 3; 141]. However, for complex and seldom analyzed systems or components, universally valid definitions are not available. For clarity, all exergetic efficiencies provided in this work are accompanied by the corresponding product and fuel definitions.

Being based on identical product and fuel definitions, comparisons between exergetic efficiencies of similar components (e.g. compressors) are valid. In contrast, comparisons between exergetic efficiencies of dissimilar components (e.g. compressor and heat exchanger) are not meaningful [11, Chapter 3], because the maximum possible exergetic efficiencies depend on the component-specific state of the art.

4.4.2 Economic analysis

The economic analysis assigns costs to each component and each input quantity of the PHES system. Purchased equipment costs as well as operation and maintenance costs are determined for each component of the PHES system. Due to a scarcity of reliable, up-to-date data, market researches do not prove useful for determining purchased equipment costs.

Frangopoulos [30] introduces detailed cost functions that relate crucial performance figures of a component to its purchased equipment cost. The cost function of a turbine, for example, considers the mass flow, the pressure ratio and the inlet temperature of the working fluid as performance figures. Although the Frangopoulos cost functions have often been used in literature (e.g. [11, Appendix B; 146]) they have two shortcomings which prevent their employment in this work. First, developed for cogeneration plants, the cost functions are available for a limited amount of components and cover only a fraction of the PHES system components. Second, none of the publications presenting the cost functions describe the performance range in which the functions deliver reliable purchased equipment costs.

The purchased equipment costs of most components in this work are determined using cost correlations based on large-scale manufacturer inquiries. The module factor approach, originally introduced by Guthrie [38; 39] and modified by Ulrich [145], is employed in the most recent form presented by Turton et al. [144, Appendix A]. Based on cost data gained in a survey of equipment manufacturers between May and September 2001, the purchased equipment costs Z_C^PEC of a component C are fitted to the equation

$$\log_{10} Z_{C,\mathrm{Turton}}^\mathrm{PEC} = K_{C,1} + K_{C,2} \log_{10} A_C + K_{C,3} (\log_{10} A_C)^2. \tag{4.69}$$

The specific capacity/size parameter A_C of component C determines the costs and has to be within certain boundaries for the fitting equation to be valid. The fitting parameters $K_{C,1}$, $K_{C,2}$, and $K_{C,3}$ are provided for various components. Complementing the module factor approach in the form of additional components or broader capacity/size parameter ranges, cost curves provided by Towler et al. [140, Chapter 7] are employed. Based on cost data gained in a survey of equipment manufacturers in January 2010, Towler et al. fitted the purchased equipment costs Z_C^PEC of a component C to the equation

$$Z_{C,\mathrm{Towler}}^\mathrm{PEC} = K_{C,1} + K_{C,2} A_C^{K_{C,3}}. \tag{4.70}$$

Similarly to (4.69), A and $K_{C,1}, \ldots, K_{C,3}$ describe the component-specific capacity/size parameter and three fitting parameters, respectively.

For components that are not covered by the module factor or cost curves approach, a more basic cost scaling approach [11, Chapter 7; 144, Chapter 7] of the form

$$\frac{Z_{C,1}^{\mathrm{PEC}}}{Z_{C,2}^{\mathrm{PEC}}} = \left(\frac{A_{C,1}}{A_{C,2}}\right)^{K_{C,1}} \tag{4.71}$$

can be employed. In a first step, two components of the same type, each being characterized by a set of capacity/size parameter and purchased equipment costs, $A_{C,1}$ and $Z_{C,1}^{\mathrm{PEC}}$ as well as $A_{C,2}$ and $Z_{C,2}^{\mathrm{PEC}}$, are used to determine the scaling exponent $K_{C,1}$. For most types of components the scaling exponent is around 0.6. In a second step, the capacity/size parameter of a component for which the purchased equipment costs shall be determined, is inserted for $A_{C,1}$, resulting in those costs to be given by $Z_{C,1}^{\mathrm{PEC}}$.

Because the different approaches employed to determine the purchased equipment costs are based on data out of different years, the effects of price developments and inflation are roughly accounted for by converting the cost values to a common reference year. Due to its good applicability to total plants and groups of components [11, Chapter 7], the Chemical Engineering Plant Cost Index *CEPCI* is employed, which is published in each issue of the journal Chemical Engineering [15]. In accordance with

$$\frac{Z_{\text{projected year}}^{\mathrm{PEC}}}{Z_{\text{reference year}}^{\mathrm{PEC}}} = \frac{CEPCI_{\text{projected year}}}{CEPCI_{\text{reference year}}}, \tag{4.72}$$

purchased equipment costs scale linearly with the *CEPCI*.

Exemplarily, the purchased equipment costs Z_C^{PEC} in Euro, determined with the Turton/Towler cost curves and converted to the reference year 2016 become

$$Z_C^{\mathrm{PEC}} = Z_{C,\text{Turton/Towler}}^{\mathrm{PEC}} r_{€\$} \frac{CEPCI_{2016}}{CEPCI_{\text{Turton/Towler}}}, \tag{4.73}$$

with $r_{€\$}$ being the Euro-Dollar exchange rate of the year 2016.

The annuity method, as described in [11, Chapter 7], is employed to divide the purchased equipment costs over the entire projected operating time of n^{an} years into equal yearly payments, taking compounded interest at an interest rate i into account. In addition, a constant factor γ is introduced to estimate the annual operation and maintenance costs by assuming that these costs are proportional to the purchased equipment costs [11, Chapter 7]. Consequently, the annual component costs are given by

$$Z_C^{\mathrm{an}} = \left(\frac{i(1+i)^{n^{\mathrm{an}}}}{(1+i)^{n^{\mathrm{an}}} - 1} + \gamma\right) Z_C^{\mathrm{PEC}}. \tag{4.74}$$

Because the exergoeconomic analysis is conducted for a single operation period, the component costs per operation period Z_C^{OP} are determined by dividing the annual component costs equally among the number of annual operation periods N^{an}

$$Z_C^{\mathrm{OP}} = \frac{Z_C^{\mathrm{an}}}{N^{\mathrm{an}}}. \tag{4.75}$$

Table 4.10: Values of the Chemical Engineering Plant Cost Index *CEPCI* employed in this work to convert purchased equipment costs to the reference year 2016.

	2016 (preliminary)	January 2010 Towler et al., cost curves	2008	May - September 2001 Turton et al., module factor approach
CEPCI	542.1	532.9	575.4	397.0
reference	[15]	[140, Chapter 7]	[15]	[144, Appendix A]

Table 4.11: Parameters of the economic model that are equally set for all analyses in this work.

	$r_{€\$}$	i	γ	n^{an}	N^{an}
value	$0.90\,€\,\$^{-1}$	1.50 %	1.50 %	20 a	365
reference	[59]	[148]	[11, Chapter 7]	[11, Chapter 7]	Chapter 5.2

In this work, the exergoeconomic analysis will be conducted with respect to the reference year 2016. The cost indices necessary to convert the costs determined by the cost functions presented in this section, are summarized in Table 4.10. Parameters of the economic model that are equally set for all analyses are given in Table 4.11. The values for the Euro-Dollar exchange rate $r_{€\$}$ and the interest rate i are also based on the reference year 2016. The number of operation periods per year N^{an} is deduced in Chapter 5.2.

Purchased equipment, operation, and maintenance costs are considered in this work. Additional costs, such as costs for piping, buildings, engineering, and installation, are not considered. Because additional costs can be expected to scale with purchased equipment costs [11, Chapter 7; 144, Chapter 7], the influence of additional costs is taken into consideration by the sensitivity analysis. Moreover, neglecting additional costs does not restrict the comparative exergoeconomic evaluation of the PHES systems covered in this work.

4.4.3 Exergoeconomic analysis

The first approaches in thermoeconomics combining thermodynamic and economic considerations arose in the third decade of the previous century [125]. Szargut [136] was among the first who combined exergetic and economic considerations. A detailed approach called exergy costing was developed by Tsatsaronis [141]. Exergy costing became also known as exergoeconomic analysis and is widely accepted and applied. Therefore, the exergoeconomic analysis based on Tsatsaronis is chosen to analyze and evaluate PHES systems in this work. The basic approach of an exergoeconomic analysis is described in the following, a detailed introduction can be found in [11, Chapter 8; 141].

Costs associated with the operation of a system are provided by the economic analysis as input parameters to the exergoeconomic model. In the case of the PHES system, these costs are composed of the component costs per operation period and the costs for the electrical energy entering the heat pump. It is important that these costs are entering the model at the very component that is responsible for the cost generation.

The exergoeconomic model calculates the cost propagation through the system to analyze by relating costs and exergy at each working fluid pipe, electrical lead, and mechanical shaft that carries exergy. Costs C are assigned to exergy E via exergy costing [11, Chapter 8; 141]

$$\mathrm{d}C = c\,\mathrm{d}E, \tag{4.76}$$

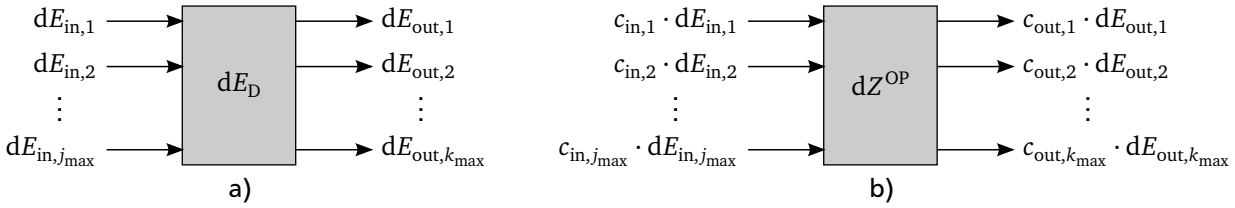

Figure 4.17: Sample component for an exergoeconomic analysis. Due to exergies entering and leaving the component a) costs enter and leave the component b).

introducing the specific costs per exergy c, which can be determined by cost balances. Figure 4.17 a) depicts a sample component being subject to entering and leaving exergies. Changes in system exergy $\mathrm{d}E_{\mathrm{sys}}$ are neglected, because they vanish for the cyclic processes analyzed in this work. The costs entering and leaving the sample component (Figure 4.17 b)) result in the following cost balance

$$\sum_{j=1}^{j_{\max}} \mathrm{d}C_{\mathrm{in},j} + \mathrm{d}Z^{\mathrm{OP}} = \sum_{k=1}^{k_{\max}} \mathrm{d}C_{\mathrm{out},k} \tag{4.77a}$$

$$\sum_{j=1}^{j_{\max}} \left(c_{\mathrm{in},j} \cdot \mathrm{d}E_{\mathrm{in},j} \right) + \mathrm{d}Z^{\mathrm{OP}} = \sum_{k=1}^{k_{\max}} \left(c_{\mathrm{out},k} \cdot \mathrm{d}E_{\mathrm{out},k} \right). \tag{4.77b}$$

Cost balances around each component of a system yield a linear system of equations for the unknown specific costs per exergy c. If system components have more than one exergy outlet, auxiliary relations are needed, which provide additional relations between the unknown specific costs per exergy. For standard heat pump and heat engine components, auxiliary relations are suggested in literature [11, Chapter 8; 141]. After having determined the specific costs per exergy c for all exergies $\mathrm{d}E$ processed by the system, the associated costs $\mathrm{d}C$ are determined using Equation (4.76).

For a detailed analysis of a component, system, or subsystem, costs for product and fuel exergies are defined [11, Chapter 8; 141]

$$\mathrm{d}C_{\mathrm{P}} = c_{\mathrm{P}}\, \mathrm{d}E_{\mathrm{P}}, \qquad \mathrm{d}C_{\mathrm{F}} = c_{\mathrm{F}}\, \mathrm{d}E_{\mathrm{F}}. \tag{4.78}$$

Based on the same product and fuel definitions deduced for the determination of exergetic efficiencies, the costs $\mathrm{d}C$ are employed to determine the costs for product and fuel exergies, $\mathrm{d}C_{\mathrm{P}}$ and $\mathrm{d}C_{\mathrm{F}}$. Afterwards, the specific product and fuel costs c_{P} and c_{F} are calculated using Equation (4.78).

Tsatsaronis and Bejan [11, Chapter 8; 141] define several exergoeconomic variables, like the cost of exergy destruction, the relative cost difference, and the exergoeconomic factor, which can be used to evaluate the exergoeconomic performance of components of a system. The value ranges that these variables attain depend on the component type; comparisons across components of different types are not meaningful. Therefore, exergoeconomic variables are useful to evaluate component performances of large systems that contain several components of the same type. The PHES systems analyzed in this work, however, rarely contain more than one component of a single component type. Consequently, the exergoeconomic variables are not considered in this work.

Moreover, the level of detail of the modeled PHES systems allows for the comparison of system and subsystem performance. However, the level of detail is considered to be too low in order to compare the performance of single components.

4.5 Sensitivity analysis procedures

Saltelli et al. [122] define sensitivity analysis as "the study of how the uncertainty in the output of a model (numerical or otherwise) can be apportioned to different sources of uncertainty in the model input." In other words, a sensitivity analysis provides information about the relative importance of the input factors in determining the output [121]. Usually input factors "follow a very asymmetric distribution of importance, few factors accounting for most of the output uncertainty with most factors playing little or no role" [122]. Consequently, a sensitivity analysis is closely connected to an uncertainty analysis. Input factors for both analysis methods can be variables, parameters, and quantities that are allowed to vary and the effect of which on the model output should be studied [121].

Next to the uncertainty originating from the input factors, an uncertainty stemming from the model itself can be apportioned. The uncertainty stemming from the model can only be determined and evaluated meaningfully, if several different models exist to calculate the desired output. For the PHES systems considered in this work, only one model representation is available for each, the physical and the exergoeconomic model. Therefore, the models are considered of being right and adding no uncertainty to the output.

4.5.1 Models and possible procedures

In general, models provide various output factors. A sensitivity analysis can be conducted with respect to only one output factor at a time. Therefore, the output factor of interest, possibly a scalar, which provides the top-most information that the model is supposed to provide, should be selected for sensitivity analysis [122].

Models and their input factors can be clustered in different groups. On the one hand, models can either be linear or non-linear. In linear models the output is a linear function of the input factors. This property does obviously not hold for non-linear models. However, non-linear models can be additive, which means that the model output is an additive combination of terms that each depend on one single input factor only. Additive models can be linear or non-linear, while non-additive models are always non-linear. On the other hand, models can either have orthogonal or non-orthogonal input factors. Orthogonal input factors are completely independent of each other whereas non-orthogonal input factors have a dependency structure, which means they are correlated[1] [122]. The combination of the introduced properties yields different groups which demand different methods for sensitivity analysis (Figure 4.18). Linear models with orthogonal input factors are the most easy ones to handle and regression based sensitivity analysis methods can be applied. Non-additive models in combination with non-orthogonal input factors entail the highest complexity and require variance decomposition methods for meaningful sensitivity analyses.

For computationally intensive models with complex combinations of model and input factor properties, the numerical cost per model evaluation might be significant. Because variance decomposition methods require a substantial amount of model evaluations, these methods might not be applicable in this case, especially if the number of input factors is high. Screening methods for sensitivity analysis might be an alternative; they provide qualitative sensitivity measures based on a limited amount of model evaluations [122]. In the following sections, a short overview of the aforementioned sensitivity analysis methods is presented.

[1] Orthogonal input factors are non-correlated, whereas the inverse is not true. Non-correlated input factors are not necessarily orthogonal [122].

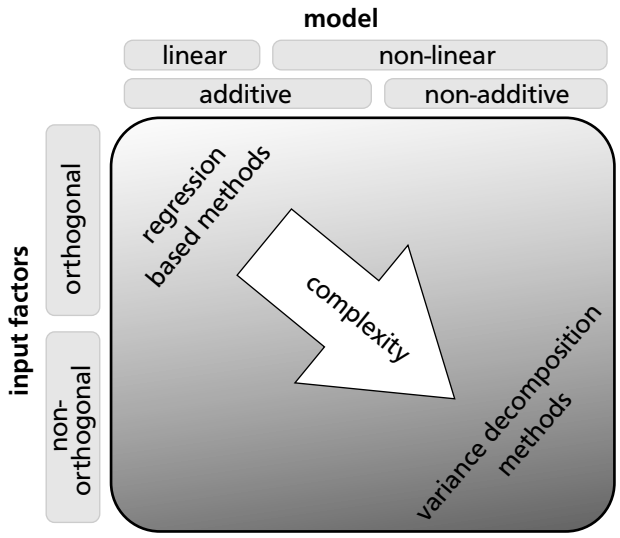

Figure 4.18: The combination of model and input factor properties yields different groups which require different sensitivity analysis methods. The darker the shading, the more complex the combination of model and input factor properties is, requiring more sophisticated sensitivity analysis methods.

Regression based methods

As usual for global sensitivity analysis methods, the entire input space of each input factor is explored [122]. Consequently, the effect of one input factor is averaged over all possible values of the other input factors. However, regression based methods have a poor performance for non-linear models and might produce totally misleading results for non-monotonic models. Consequently, these methods are not model-independent and do therefore not fulfill all criteria of an ideal sensitivity analysis [122].

Variance decomposition methods

Variance decomposition methods are model independent and fulfill all criteria of an ideal sensitivity analysis [122]. Consequently, these methods are powerful but can become computationally very expensive. Non-orthogonal input factors should only be considered when absolutely necessary. Saltelly et al. [122] suggest to always start a sensitivity analysis by treating all input factors as orthogonal ones.

Screening methods

Sensitivity analyses based on screening methods require a relatively small number of model evaluations, especially if the model has only a few influential input factors next to a lot of non-influential ones, and are usually easy to implement [122]. The number of required model runs is a linear function of the number of examined factors. However, screening methods provide only qualitative results in the form of a ranking of input factors, but they do not provide information about how much the factors differ in importance.

Morris' method [98] is often applied due to its global approach which averages local effects over the entire value range of all input factors. It provides a classification of all input factors with respect to their effect on the output in terms of negligible, linear and additive, and nonlinear or interactive effects.

The Morris method is referred to as “one-factor-at-a-time” method which means that input factors are changed individually in order to evaluate their effect on the output.

4.5.2 Selected sensitivity analysis procedure

The exergoeconomic analysis of PHES systems is based on various input factors as parameters, material properties, efficiencies and cost data, to name just a few, all of which have uncertainties attached to their values. Due to the scarcity of reliable data, the purchased equipment cost are expected to be the most uncertain input factors. Therefore, the sensitivity analysis focuses on the exergoeconomic model. The considered input factors are the purchased equipment costs of the PHES system components $Z_{\mathrm{C}}^{\mathrm{PEC}}$ and the specific costs for electrical energy $c_{\mathrm{el,in}}$ entering the PHES system during heat pump operation. As output factor of the sensitivity analysis, the specific costs for electrical energy $c_{\mathrm{el,out}}$ leaving the PHES system during heat engine operation are selected. Because the exergoeconomic model, assigning costs to exergy via exergy costing, is linear (4.4.3), a regression based sensitivity analysis method should be selected.

Because the implementation and evaluation of a complete regression based sensitivity analysis could not be completed in the scope of this work, a simplified approach is selected. This approach evaluates the sensitivity of the selected economic output factor with respect to the uncertainty of the economic input factors. The exergoeconomic cost balance (Equation (4.77)) around the complete PHES system reads

$$c_{\mathrm{el,in}} E_{\mathrm{el,in}} + Z_{\mathrm{PHES}}^{\mathrm{OP}} = c_{\mathrm{el,out}} E_{\mathrm{el,out}}, \tag{4.79}$$

with

$$Z_{\mathrm{PHES}}^{\mathrm{OP}} = \sum_{\mathrm{C}} Z_{\mathrm{C}}^{\mathrm{OP}} \tag{4.80}$$

being the component costs per operation period of the entire PHES system. Rearranging Equation (4.79) for the desired output factor yields

$$c_{\mathrm{el,out}} = \frac{c_{\mathrm{el,in}} E_{\mathrm{el,in}} + Z_{\mathrm{OP}}^{\mathrm{PEC}}}{E_{\mathrm{el,out}}}. \tag{4.81}$$

For each PHES system analyzed in this work, the influence of variations in specific costs per electrical energy entering the system $c_{\mathrm{el,in}}$ and the influence of variations in purchased equipment costs $Z_{\mathrm{OP}}^{\mathrm{PEC}}$ on the specific costs per electrical energy released by the system $c_{\mathrm{el,out}}$ is determined. First, $c_{\mathrm{el,in}}$ is varied between 0 % and 200 % of its initial value, while $Z_{\mathrm{OP}}^{\mathrm{PEC}}$ stays constant at its initial value. Second, $c_{\mathrm{el,in}}$ stays constant at its initial value and $Z_{\mathrm{OP}}^{\mathrm{PEC}}$ is varied between 0 % and 200 %. In a third approach, both values are varied simultaneously between 0 % and 200 %.

5 Preliminary Considerations for the Exergoeconomic Analyses

In this chapter, preliminary considerations are described, which are necessary for and applied to all exergoeconomic analyses. First, the thermodynamic reference conditions are defined. Second, a characteristic operation scenario is deduced from the European market for electrical energy. Afterwards, the cyclic steady state is introduced as basis for a reproducible analysis of transient system operation. Finally, energetic and exergetic efficiencies of the PHES system and its subsystems are presented.

5.1 Thermodynamic reference conditions

During operation, a PHES system exchanges heat and mass, if applicable, with the surrounding environment. Consequently, the thermodynamic reference conditions necessary for an exergy analysis are given by the ambient conditions. The ambient temperature is is based on the mean temperature in Germany in the years 2015 and 2016 [21; 22].

$$T_{\mathrm{ref}} = T_{\mathrm{amb}} = 10\,^{\circ}\mathrm{C} \tag{5.1a}$$

$$p_{\mathrm{ref}} = p_{\mathrm{amb}} = 1\,\mathrm{bar} \tag{5.1b}$$

5.2 Characteristic operation scenario

Operation scenarios depend on the structure of and the conditions on the electrical energy market. Therefore, possible operation scenarios are deduced from a brief introduction to the European energy market. A characteristic operation scenario is selected based on the economic requirements imposed by a PHES system.

5.2.1 European market for electrical energy

A schematic overview of the European market for electrical energy is depicted in Figure 5.1. On the one hand, the wholesale of electrical energy is based on over-the-counter (OTC) trades between suppliers and major consumers [14]. At the OTC market, there is few transparency without standards for products, terms, and conditions. On the other hand, the wholesale of electrical energy is based on transparent, standardized trading at the European Energy Exchange (EEX) [26]. At the derivatives market, under the roof of the EEX, long-term trading takes place up to six years in advance of supply.

EEX short-term trading takes place at the spot market, being divided into the day-ahead market and the intraday market, both operated by the European Power Exchange (EPEX Spot) [27]. Until noon, the electrical energy supply of the following day is traded at the day-ahead market, principally clustered in one hour time frames. As long as the capacity of the electrical grid is sufficient, international offers are considered to fulfill national demands among Austria, the Benelux countries, France, Germany, Great

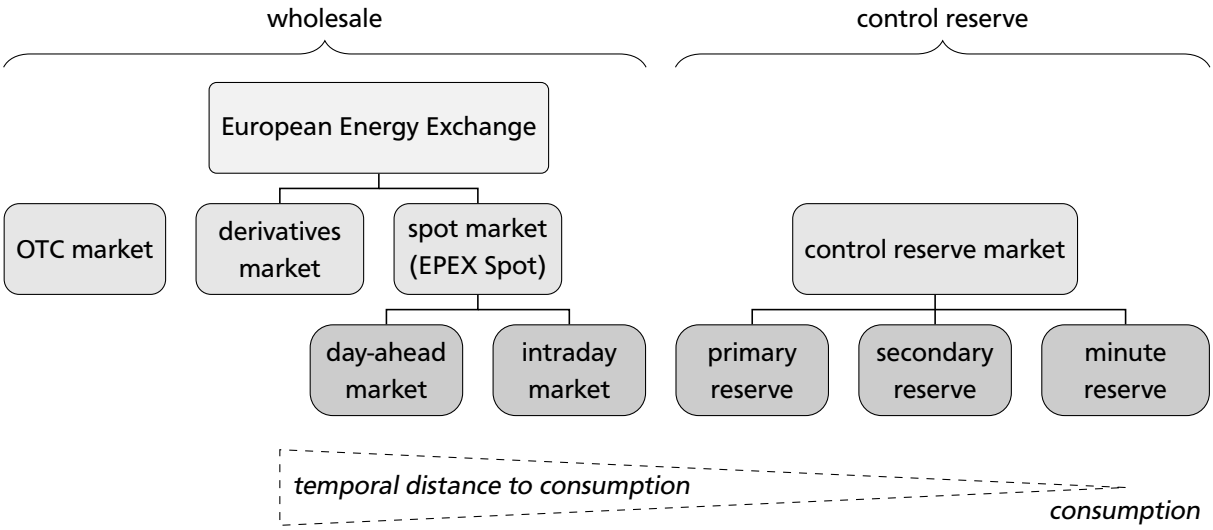

Figure 5.1: Schematic overview of the European market for electrical energy.

Britain and Switzerland [27]. To determine the market price of electrical energy, all supply offers are ranked in ascending order. Following the merit order and matching the projected demand (market clearing volume), the cheapest suppliers win the bid. The highest offer among all selected suppliers determines the price (market clearing price) that is payed to all suppliers, independent of their original offers [31; 103].

When the supply of electrical energy exceeds the projected demand extremely, negative electricity prices can occur at the day-ahead market. Although negative electricity prices coincide with a large supply of electrical energy from renewable sources, the ultimate reason lies in the insufficient flexibility of the conventional suppliers [37]. In peak times the supply of renewably generated electrical energy did never exceed 65 % [37].

Temporally closer to generation of electrical energy, the demand estimations are likely to change. At the intraday market, electrical energy can be traded until 30 minutes before generation in order to balance supply and demand [14; 26]. The trading is organized in flexible time frames of 15 minutes up to several hours.

Deviations from the projections lead to differences between the real supply and demand. These differences are balanced by the grid operators at the control reserve market. Suppliers having capacities exceeding 5 MW [31] can offer positive or negative control reserves. The offers are clustered into primary control reserve, secondary control reserve, or minute reserve, depending on the start up time to full load, being within 30 s, 5 min or 15 min, respectively [14].

5.2.2 Identification of possible operation scenarios

Characteristic operation scenarios need to be based on common, repetitive market situations. Due to the lack of standards and transparency, the OTC market cannot be used to deduce characteristic operation scenarios. As the derivatives market focuses on large volume, long term contracts, it is unlikely to beneficially capitalize the operation of a medium sized electricity storage system at this market. At the control reserve and intraday market, electrical energy is traded in short and irregular time periods which are not favorable as a basis for repetitive operation of PHES systems.

The development of electricity prices at the day-ahead market for Germany and Austria shows a high predictability regarding daily repetitiveness [28]. The hourly prices for electrical energy averaged over

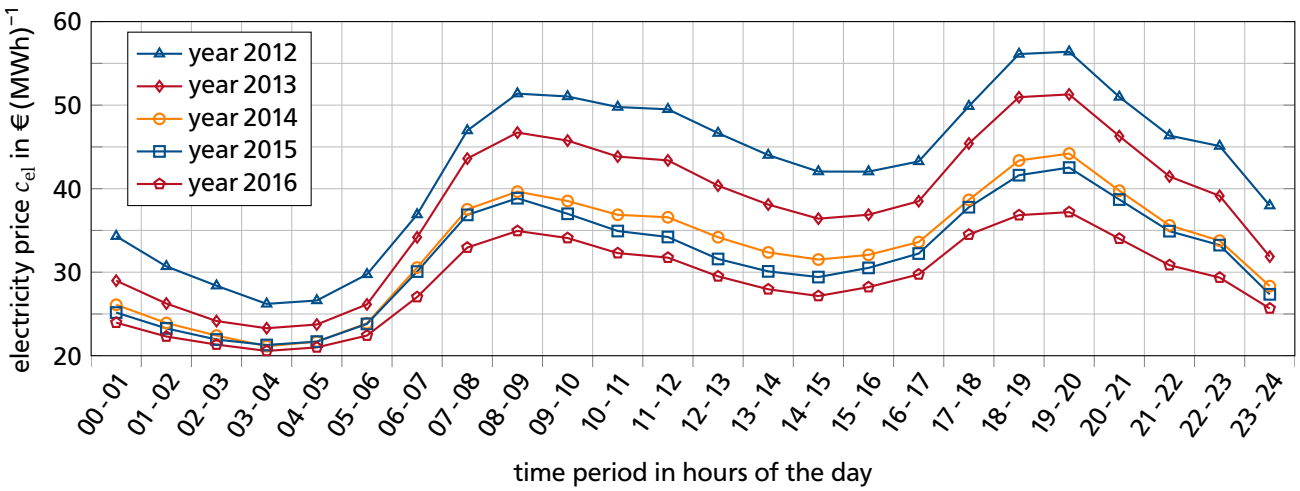

Figure 5.2: Yearly averaged, hourly prices for electrical energy at the day-ahead market (data by [28]).

the course of a year indicate similar distributions for the years 2012 to 2016 (Figure 5.2). In the early morning hours around 4:00 h the price distributions have a global minimum, which indicates a large potential electricity supply compared to the projected demand. In contrast, in the evening hours around 19:00 h the price distributions have a global maximum, which indicates a small potential electricity supply compared to the actual demand. As a consequence, a characteristic operation scenario of the PHES system based on the day-ahead market is composed of a heat pump operation (charging) in the early morning and a heat engine operation (discharging) in the evening hours. Thereby, the economically favorable price difference between heat pump and heat engine operation can be maximized. Considering the grid, the mismatch between potential electricity supply and projected demand can be reduced.

An economically favorable operation of a PHES system has to account for two reverse effects. On the one hand, the prices for electrical energy should be low during heat pump operation and high during heat engine operation. Maximizing this price difference reduces the amount of possible operation periods of the PHES system. On the other hand, the influence of the purchased equipment costs should be kept small by distributing them on many operation periods resulting in low component costs per operation period.

Charging the PHES system only if the day-ahead market reports negative prices for electrical energy, increases the price difference further between heat pump and heat engine operation. However, previous calculations showed that operation scenarios solely based on negative electricity prices at the day-ahead market are currently not economically feasible [4, Chapter 4.3; 31, Chapter 3.3]. The number of operation periods per year is too low which results in unacceptably high component costs per operation period. Nevertheless, if the base load supplied by conventional power plants stays constant, the amount of negative electricity prices is expected to rise from 64 h in 2013 to 1000 h in 2022 [37]. Consequently, the operation of PHES systems based on negative electricity prices might become beneficial in the near future.

Previous calculations also showed that operation scenarios being based on the minute reserve alone and on a combination of minute reserve and day-ahead market are economically less beneficial than operation scenarios being based on the day-ahead market alone [31, Chapter 3.4].

5.2.3 Selection of a characteristic operation scenario

Resulting from the evaluation of possible characteristic operation scenarios in the previous section, the selected scenario is based on the day-ahead market for Germany and Austria. This market shows a high predictability regarding daily repetitiveness of the electricity price distribution [28]. As introduced at the end of Chapter 2.3, the DLR [66] identified potential economic and operational feasibility for small scale electrical energy storage systems with a charge/discharge power of 10 MW_{el} to 30 MW_{el}, charge/discharge times of 4 h to 6.5 h, and capacities in the order of 50 MWh_{el} to 150 MWh_{el}. In this work, PHES systems classified at the lower boundaries of the aforementioned ranges are considered. To maximize the electricity price difference (Figure 5.2) the PHES system shall be charged for 4 h in the early morning and discharged for 4 h in the later course of the day, performing a complete operation period once within 24 h, at each day of the year ($N^{an} = 365$).

To account for recent developments on the day-ahead market, the electricity prices of the year 2016 are solely selected as reference data. For each day of the year, the continuous 4 hour time periods with the lowest and highest average electricity price between 23:00 h of the previous day and 24:00 h are determined. Because these time periods are used for the heat pump and heat engine operation of the PHES system, the time periods do not overlap and the heat pump operation periods take place prior to the heat engine operation periods. Averaging the electricity prices of all determined time periods over the entire year results in average market prices of 19.66 € $(MWh)^{-1}$ = 1.966 ct $(kWh)^{-1}$ during the heat pump and 38.42 € $(MWh)^{-1}$ = 3.842 ct $(kWh)^{-1}$ during the heat engine operation of the PHES system. The frequency distribution of the operation periods shows that most heat pump operation takes place between 01:00 h and 05:00 h and most heat engine operation between 17:00 h and 21:00 h (Figure 5.3).The specification of the characteristic operation scenario used for the exergoeconomic analysis is summarized in Table 5.1.

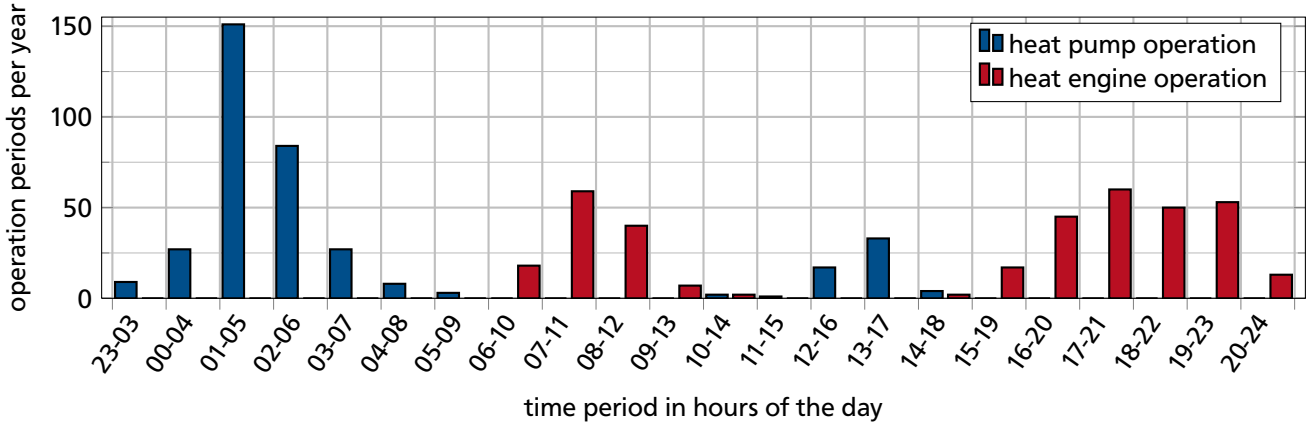

Figure 5.3: Frequency distribution of the daily 4 h heat pump and heat engine operation for the reference year 2016.

Table 5.1: Specification of the characteristic operation scenario used for the exergoeconomic analyses.

operation mode	start time in h	end time in h	duration in h	averaged electricity price
heat pump (charging)	01:00	05:00	4	19.66 € $(MWh)^{-1}$
idle after heat pump	05:00	17:00	12	-
heat engine (discharging)	17:00	21:00	4	38.42 € $(MWh)^{-1}$
idle after heat engine	21:00	01:00	4	-

5.2.4 Evaluation of the economic environment for electrical energy storage systems

The yearly averaged, hourly prices for electrical energy at the day-ahead market are constantly falling for the years 2012 to 2016 (Figure 5.2). Moreover, price differences between the averaged daily maximum and daily minimum are decreasing from 30.18 € $(\mathrm{MWh})^{-1}$ in 2012 to 16.62 € $(\mathrm{MWh})^{-1}$ in 2016. This trend results in a decreasing economic potential for electrical energy storage systems. The currently unfavorable and prospectively uncertain economic environment for electrical energy storage systems was also identified and criticized by the German Aerospace Center (DLR) [66; 158] and RWE power [99]. Consequently, a potentially uneconomically operation of the PHES system has to be mitigated in the light of the current economic environment.

5.3 Cyclic steady-state analysis

As described in Chapter 4, the operation of the PHES system is simulated transiently. Due to varying storage inlet and outlet conditions, the charge states of the TES systems influence the operation of the remaining PHES system, which in turn influences the charge states of the TES systems. The individual charge state is characterized by a specific distribution of internal energy and temperature within the storage material.

A meaningful and reproducible analysis has to be independent of arbitrary charge states. The simulation of consecutive operation periods of the PHES system according to the characteristic operation scenario eventually converges into the cyclic steady state. Operation periods in cyclic steady state have the following characteristics:

- the end of one period marks the beginning of the following period,
- all periods take the same time,
- each TES system has identical charge states at the beginning and at the end of the operation period,
- and the time-dependent course of the PHES operation is identical for all operation periods.

All exergoeconomic analyses in this work are based on the simulation results of a characteristic operation period in cyclic steady state. The time-dependent exergy flows $\dot{E}$ processed by each component are integrated over the entire operation period. The resulting amounts of exergy E are then processed in the exergoeconomic analyses. Equivalently, component costs per operation period Z^{OP} are considered in the analyses. Specifying a daily operation of the PHES system, these costs are linearly derived from the annual component costs Z^{an}.

5.4 Energetic and exergetic efficiencies of a PHES system

As already introduced in Chapter 1, the round-trip efficiency of a PHES system is defined as the ratio of electrical energy released during heat engine operation to electrical energy supplied during heat pump operation. Against the purpose of the PHES system this definition is easily comprehensible. Because electrical energy is pure exergy, a distinction between energetic round-trip efficiency and exergetic round-trip efficiency is not necessary

$$\eta_{\mathrm{PHES}} = \frac{En_{\mathrm{el,out}}}{En_{\mathrm{el,in}}} = \frac{E_{\mathrm{el,out}}}{E_{\mathrm{el,in}}}. \tag{5.2}$$

In order to analyze the performance of a PHES system in more detail, the efficiencies of the subsystems are evaluated. From an exergetic and energetic point of view, the subsystems heat pump (HP), thermal

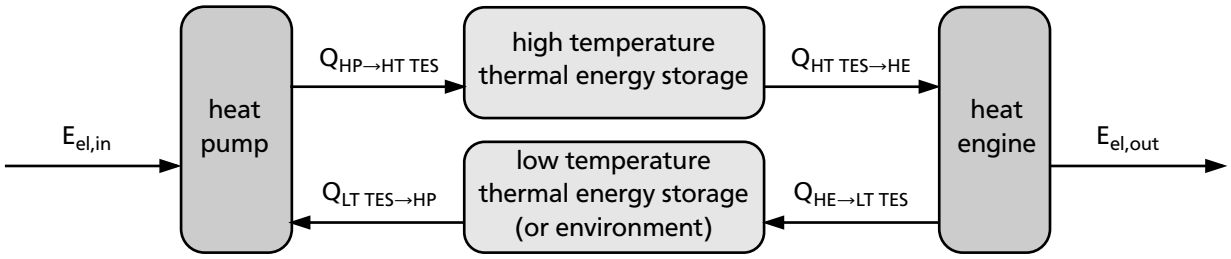

Figure 5.4: Amounts of energy transferred between environment and subsystems of the PHES system.

energy storage (TES), and heat engine (HE) are arranged in sequence. As a consequence, the product of the subsystem efficiencies has to be equal to the round-trip efficiency of the entire PHES system

$$\eta_{\mathrm{PHES}} = \eta_{\mathrm{en,HP}} \cdot \eta_{\mathrm{en,TES}} \cdot \eta_{\mathrm{en,HE}} = \frac{En_{\mathrm{el,out}}}{En_{\mathrm{el,in}}} \tag{5.3a}$$

$$= \eta_{\mathrm{ex,HP}} \cdot \eta_{\mathrm{ex,TES}} \cdot \eta_{\mathrm{ex,HE}} = \frac{E_{\mathrm{el,out}}}{E_{\mathrm{el,in}}}. \tag{5.3b}$$

Referring to Figure 5.4, which illustrates the amounts of energy being transferred between environment and subsystems of the PHES system, two possible sets of efficiencies are defined.

The first set of efficiencies (η_{I}, Equation (5.4)) is deduced for PHES systems without low temperature TES, which results in the following definitions

$$\eta_{\mathrm{PHES}} = \underbrace{\frac{Q_{\mathrm{HP\rightarrow HT\ TES}}{En_{\mathrm{el,in}}}}_{\eta_{\mathrm{I,en,HP}}} \cdot \underbrace{\frac{Q_{\mathrm{HT\ TES\rightarrow HE}}{Q_{\mathrm{HP\rightarrow HT\ TES}}}}_{\eta_{\mathrm{I,en,TES}}} \cdot \underbrace{\frac{En_{\mathrm{el,out}}}{Q_{\mathrm{HT\ TES\rightarrow HE}}}}_{\eta_{\mathrm{I,en,HE}}}, \tag{5.4a}$$

$$= \underbrace{\frac{E_{\mathrm{HP\rightarrow HT\ TES}}{E_{\mathrm{el,in}}}}_{\eta_{\mathrm{I,ex,HP}}} \cdot \underbrace{\frac{E_{\mathrm{HT\ TES\rightarrow HE}}{E_{\mathrm{HP\rightarrow HT\ TES}}}}_{\eta_{\mathrm{I,ex,TES}}} \cdot \underbrace{\frac{E_{\mathrm{el,out}}}{E_{\mathrm{HT\ TES\rightarrow HE}}}}_{\eta_{\mathrm{I,ex,HE}}}. \tag{5.4b}$$

This approach is consistent with the widely used definitions of heat pump and heat engine efficiencies. For comparisons, the first set of efficiencies can also be applied to PHES systems having a high and a low temperature TES. In this case, however, the neglect to account for the exergy entering the heat pump from the low temperature TES, yields to exergetic heat pump efficiencies greater than unity.

The second set of efficiencies (η_{II}, Equation (5.6)) is deduced for PHES systems having a high and a low temperature TES. The entire TES subsystem, resulting from the imaginary unification of low and high temperature TES, is subject to the following net amounts of energy and exergy transfer

$$\begin{aligned} Q_{\mathrm{HP\rightarrow TES}} &= Q_{\mathrm{HP\rightarrow HT\ TES}} - Q_{\mathrm{LT\ TES\rightarrow HP}}, & Q_{\mathrm{TES\rightarrow HE}} &= Q_{\mathrm{HT\ TES\rightarrow HE}} - Q_{\mathrm{HE\rightarrow LT\ TES}}, \\ E_{\mathrm{HP\rightarrow TES}} &= E_{\mathrm{HP\rightarrow HT\ TES}} - E_{\mathrm{LT\ TES\rightarrow HP}}, & E_{\mathrm{TES\rightarrow HE}} &= E_{\mathrm{HT\ TES\rightarrow HE}} - E_{\mathrm{HE\rightarrow LT\ TES}}. \end{aligned} \tag{5.5}$$

Based on these net amounts of energy and exergy transfer, the second set of efficiencies becomes

$$\eta_{\mathrm{PHES}} = \underbrace{\frac{Q_{\mathrm{HP}\rightarrow\mathrm{HT\ TES}} - Q_{\mathrm{LT\ TES}\rightarrow\mathrm{HP}}}{En_{\mathrm{el,in}}}}_{\eta_{\mathrm{II,en,HP}}} \cdot \underbrace{\frac{Q_{\mathrm{HT\ TES}\rightarrow\mathrm{HE}} - Q_{\mathrm{HE}\rightarrow\mathrm{LT\ TES}}}{Q_{\mathrm{HP}\rightarrow\mathrm{HT\ TES}} - Q_{\mathrm{LT\ TES}\rightarrow\mathrm{HP}}}}_{\eta_{\mathrm{II,en,TES}}} \cdot \underbrace{\frac{En_{\mathrm{el,out}}}{Q_{\mathrm{HT\ TES}\rightarrow\mathrm{HE}} - Q_{\mathrm{HE}\rightarrow\mathrm{LT\ TES}}}}_{\eta_{\mathrm{II,en,HE}}}, \tag{5.6a}$$

$$= \underbrace{\frac{E_{\mathrm{HP}\rightarrow\mathrm{HT\ TES}} - E_{\mathrm{LT\ TES}\rightarrow\mathrm{HP}}}{E_{\mathrm{el,in}}}}_{\eta_{\mathrm{II,ex,HP}}} \cdot \underbrace{\frac{E_{\mathrm{HT\ TES}\rightarrow\mathrm{HE}} - E_{\mathrm{HE}\rightarrow\mathrm{LT\ TES}}}{E_{\mathrm{HP}\rightarrow\mathrm{HT\ TES}} - E_{\mathrm{LT\ TES}\rightarrow\mathrm{HP}}}}_{\eta_{\mathrm{II,ex,TES}}} \cdot \underbrace{\frac{E_{\mathrm{el,out}}}{E_{\mathrm{HT\ TES}\rightarrow\mathrm{HE}} - E_{\mathrm{HE}\rightarrow\mathrm{LT\ TES}}}}_{\eta_{\mathrm{II,ex,HE}}}. \tag{5.6b}$$

The above definitions have the advantage of incorporating the performance of all components. Consequently, the energetic and exergetic efficiencies of all subsystems have an upper boundary of unity, which is advantageous for exergy analyses. However, an energetic heat pump efficiency below unity is not an indicator for an inefficient system design any more.

For PHES systems having a high and low temperature TES, both sets of efficiencies will be applied in this work. While the first set of definitions (η_{I}) yields intuitively accessible results for the energetic subsystem efficiencies, the second set of definitions (η_{II}) yields intuitively accessible results for the exergetic subsystem efficiencies. Additional subsystem efficiencies that fulfill Equations (5.3) have not been derived.

6 Analysis of PHES Systems based on Joule Cycles

In this chapter, design and analysis of PHES systems based on Joule cycles are presented. First, the design of the thermodynamic cycles of heat pump and heat engine, followed by the design of the TES systems is described. Second, the calculation procedure applied to identify optimal temperature and pressure levels is introduced. Afterwards, a detailed analysis of two PHES systems is presented, comprising exergy analyses, economic analyses, and exergoeconomic analyses. The largest uncertainties are captured in a sensitivity analysis, before fundamental results are assessed.

6.1 System design

To achieve high round-trip efficiencies for PHES systems, five design constraints are deduced from the studies published in literature (Chapter 2.2.1).

1. If available, established technology should be employed in order to reduce technological risks.
2. The PHES system layout should be simple, limiting the amount of components to the essentially necessary required for an exergy efficient and cost efficient operation.
3. Heat rejection to the environment should be realized at a small temperature difference in order to minimize the associated exergy loss. Due to irreversibilities, entropy is generated within the PHES system. The generated entropy has to be rejected, which is achieved by heat rejection to the environment. If the generated entropy is not rejected to the environment it accumulates in the TES systems eventually resulting in TES temperature profiles that do neither allow for heat pump nor for heat engine operation any more.
4. The PHES system should be combined with a high and a low temperature TES instead of just one TES. This reduces the amount of heat exchanged with the environment and associated exergy losses to a minimum.
5. Regenerative heat transfer does not improve the efficiency of PHES systems based on Joule cycles and is therefore not implemented. Due to the utilization of two TES systems, the low temperature heat provided by the heat engine is already exploited. Moreover, steady-state design calculations indicated a reduction of round-trip efficiency, if regenerative heat transfer is implemented in PHES systems based on Joule cycles.

Considering the aforementioned design constraints, two setups of thermodynamic cycles are deduced. While the heat pump and heat engine design of both setups follow basic Joule cycles, the setups differ in the position of heat rejection to the environment (Figure 6.1, Table 6.1). In setup 1, heat is rejected during heat engine operation, succeeding the heat transfer from the heat engine to the low temperature TES system. In setup 2, heat is rejected during heat pump operation succeeding the heat transfer from the heat pump to the high temperature TES system.

For a reasonable operation of the PHES system, two additional design constraints have to be taken into account. First, the inlet temperature of the working fluid into the high temperature TES has to be kept constant during the entire system operation. Preliminary analyses [4; 31; 111; 155] and studies [19; 23] have shown that a constant working fluid inlet temperature is necessary to establish useful temperature

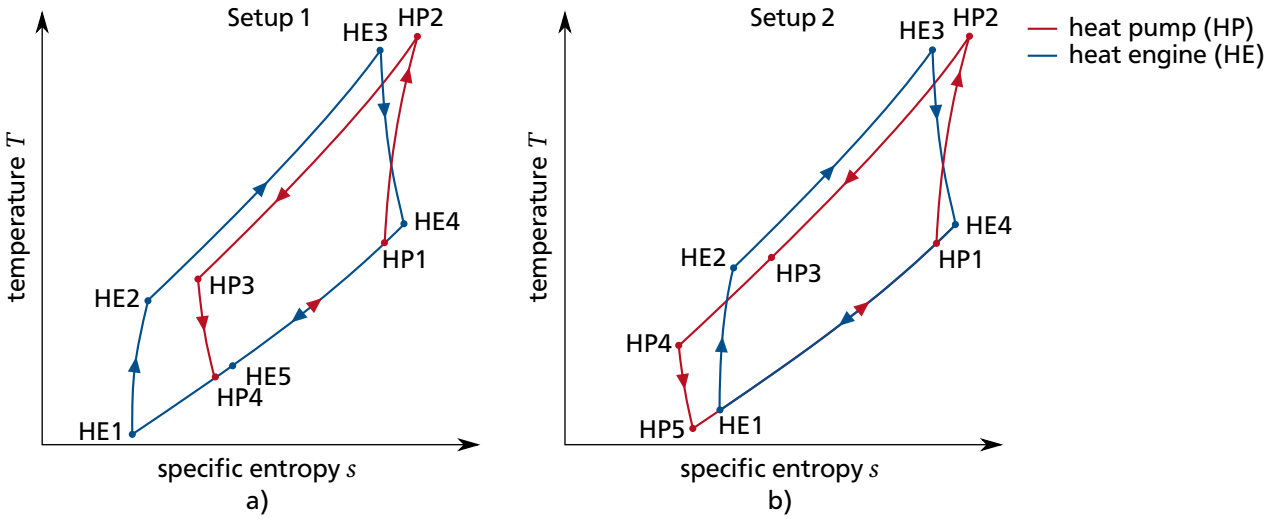

Figure 6.1: Two different setups a) and b) of thermodynamic cycles for PHES systems. While the heat pump (HP) and heat engine (HE) design of both setups follow basic Joule cycles, the setups differ in the position of heat rejection to the environment. The changes of state are explained in Table 6.1.

Table 6.1: Explanation of the changes of state for the two setups of thermodynamic cycles for PHES systems based on the Joule cycles depicted in Figure 6.1.

Change of state	Explanation setup 1 (Figure 6.1 a))	Change of state	Explanation setup 2 (Figure 6.1 b))
HP1 - HP2	compression	HP1 - HP2	compression
HP2 - HP3	heat rejection to high temp. TES	HP2 - HP3	heat rejection to high temp. TES
HP3 - HP4	expansion	HP3 - HP4	heat rejection to environment
HP4 - HP1	heat absorption from low temp. TES	HP4 - HP5	expansion
HE1 - HE2	compression	HP5 - HP1	heat absorption from low temp. TES
HE2 - HE3	heat absorption from high temp. TES	HE1 - HE2	compression
HE3 - HE4	expansion	HE2 - HE3	heat absorption from high temp. TES
HE4 - HE5	heat rejection to low temp. TES	HE3 - HE4	expansion
HE5 - HE1	heat rejection to environment	HE4 - HE1	heat rejection to low temp. TES

profiles within the TES systems that are required to finally enter the cyclic steady state. Considering the compressor characteristics, constant TES inlet temperatures of the working fluid can be achieved with varying compression ratios. Second, the electrical power consumed and released by the PHES system has to remain constant during operation in order to enable a beneficial and predictable integration into the electrical grid. Rather complex controlling algorithms might be necessary to set the required compression ratios, mass flows, and powers based on compressor characteristics. However, controlling algorithms are not developed in detail as these are not the focus of the current work.

6.1.1 Selection of thermodynamic cycles

Based on exergoeconomic considerations, the working fluid as well as the temperature and the pressure levels are specified, which leads to the selection of one out of the two possible setups of the thermodynamic cycles presented in Figure 6.1 and Table 6.1.

The initial start up phase of the PHES system or the start up phase after a longer period of downtime (e.g. due to maintenance) is not the focus of the current work and will not be analyzed in detail. Re-

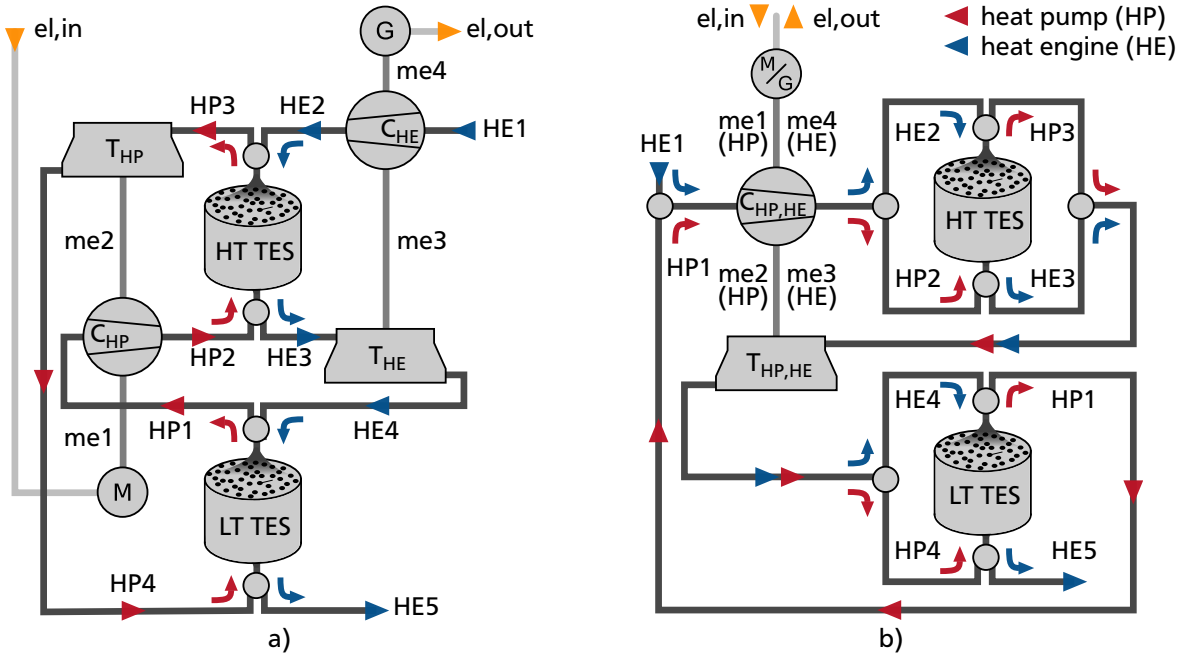

Figure 6.2: Schematics of the PHES system corresponding to setup 1 of the thermodynamic cycle depicted in Figure 6.1 a). While schematic a) illustrates a PHES system with two separate turbine-compressor strands, schematic b) is based on a single turbine-compressor strand for the entire PHES system.

ferring to the characteristic operation scenarios presented in Chapter 5.2 these start up phases are rare compared to the standard operation of the PHES system. However, PHES systems with high temperature TESs having temperature levels below ambient temperature require cooling during the initial start up phase. This cooling could only be provided employing an additional heat pump which reduces the exergoeconomic performance of the PHES system due to additional purchased equipment costs. Therefore, the temperature level of the high temperature TES system should be above ambient temperature.

Selecting air as working fluid in heat pump and heat engine enables the replacement of the heat exchanger that rejects heat and entropy to the environment. Instead of passing through the heat exchanger, the hot air could be released to the environment and air at ambient conditions could be sucked in. The replacement of the heat exchanger increases the exergoeconomic performance of the PHES system, because purchased equipment costs can be decreased and the heat exchanger pressure drop can be avoided. However, replacing the heat exchanger imposes constraints on the thermodynamic cycles. The air leaving the PHES system should be at ambient pressure to minimize exergy losses (Figure 6.1 a) setup 1: $p_{\mathrm{HE5}} = p_{\mathrm{amb}}$; Figure 6.1 b) setup 2: $p_{\mathrm{HP3}} = p_{\mathrm{amb}}$). The air entering the PHES system is provided at ambient conditions which sets further constraints of the thermodynamic cycle.

In the thermodynamic cycle of setup 2 (Figure 6.1 b)), the ambient air entering the system ($p_{\mathrm{HP4}} = p_{\mathrm{amb}}$) is expanded to a pressure significantly lower than the ambient pressure ($p_{\mathrm{HP5}} < p_{\mathrm{amb}}$). To rely on established technology and prevent condensation of air humidity inside the PHES system, pressures being below ambient pressure are avoided. Consequently, setup 1 (Figure 6.1 a), Table 6.1) is selected for the PHES system. Two schematics of a PHES system corresponding to setup 1 are depicted in Figure 6.2. The red arrows illustrate the path of the working fluid during heat pump operation, the blue arrows illustrate the path of the working fluid during heat engine operation. The working fluid passes the TES systems in opposite directions during heat pump and heat engine operation in order to minimize exergy losses and to reach the desired outlet temperatures.

Opposed to the PHES system depicted in Figure 6.2 a) with two separate turbine-compressor strands, the PHES system in Figure 6.2 b) is based on a single turbine-compressor strand. A PHES system based on the single strand schematic is selected for further consideration, because of its higher exergoeconomic performance due to lower purchased equipment costs at the expense of a slight reduction in system efficiency.

6.1.2 Consideration of Joule/resistive heating

Instead of employing a Joule cycle based heat pump to heat the high temperature TES, a cycle based on Joule/resistive heating could be selected that converts electrical energy directly into heat. Figure 6.3 depicts a Joule cycle as well as a cycle based on Joule/resistive heating. Both cycles are designed to provide the same amount of specific heat

$$h_{\mathrm{HP2}} - h_{\mathrm{HP3}} = h_{\mathrm{JH2}} - h_{\mathrm{JH3}} \tag{6.1}$$

at identical inlet $T_{\mathrm{HT\ TES,in}}$ and identical outlet temperatures $T_{\mathrm{HT\ TES,out}}$ to the high temperature TES system.

To charge the high temperature TES, the heat pump needs to be supplied with the specific electrical energy consumed by the compressor minus the specific electrical energy supplied by the turbine

$$e_{\mathrm{el,in,HP}} = h_{\mathrm{HP2}} - h_{\mathrm{HP1}} - (h_{\mathrm{HP3}} - h_{\mathrm{HP4}}). \tag{6.2}$$

In order to focus on the relevant energy conversions, the efficiency of the motor attached to the turbine-compressor set is neglected without compromising the following argumentation. The heat pump cycle is closed by heating the working fluid with heat from the low temperature TES (HP4→HP1).

To supply the same amount of specific heat to the high temperature TES (Equation (6.1)), the cycle based on Joule/resistive heating converts electrical energy directly into heat

$$e_{\mathrm{el,in,JH}} = h_{\mathrm{JH2}} - h_{\mathrm{JH1}} = h_{\mathrm{HP2}} - h_{\mathrm{HP1}}. \tag{6.3}$$

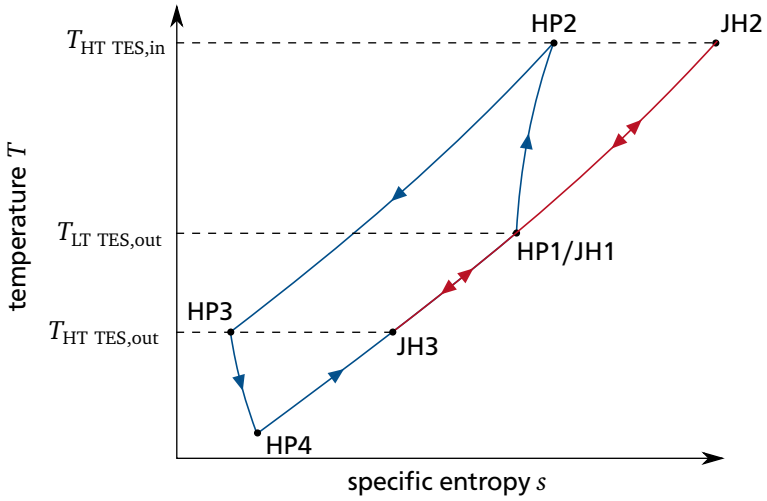

Figure 6.3: T,s-diagram of a Joule cycle based heat pump (HP) and a Joule/resistive heating cycle (JH) to heat the high temperature TES.

After leaving the high temperature TES, the cycle is closed by heating the working fluid with heat from the low temperature TES (JH3→JH1).

Comparing Equations (6.2) and (6.3) reveals that the heat pump system consumes less specific energy than the system based on Joule/resistive heating

$$e_{\mathrm{el,in,HP}} < e_{\mathrm{el,in,JH}}. \tag{6.4}$$

The heat supplied by the low temperature TES system in order to close the thermodynamic cycles is inevitably generated during the heat engine operation of the PHES system. Therefore, the higher consumption of specific heat by the heat pump compared to the Joule/resistive heating

$$h_{\mathrm{HP1}} - h_{\mathrm{HP4}} > h_{\mathrm{JH1}} - h_{\mathrm{JH3}} \tag{6.5}$$

does not represent any exergetic burden. Consequently, from an exergetic point of view, the heat pump operates more efficiently than a cycle based on Joule/resistive heating. Taking into consideration that heat pump and heat engine share the same components, the heat pump itself does not generate additional purchased equipment costs. In contrast, the cycle based on Joule/resistive heating would generate additional purchased equipment costs. As a result, the heat pump has a better exergoeconomic performance and should be preferably chosen over the Joule/resistive heating approach.

6.1.3 Selection of thermal energy storage systems

During heat transfer between TES and heat pump as well as heat engine, the working fluid experiences a temperature change. To minimize exergy losses due to heat transfer, temperature differences between working fluid and TES material should be kept small. Consequently, the PHES system based on Joule cycles is combined with sensible heat TES systems. For a reasonable heat transfer between working fluid and TES material, a packed bed arrangement is chosen (Chapter 2.6.1).

Based on a study by Rundel [119] examining the long term thermal and mechanical stability of packed beds, basalt chips without quartz content are selected as TES material. This material performed best among all tested materials; without any degradation it withstood 7000 charging and discharging cycles with inlet temperatures of 600 °C and 24 °C, respectively. Relevant material properties of basalt chips without quartz content are summarized in Table 6.2.

The volume-specific void fraction is defined in Equation (4.2). The value provided by Rundel [119; 120] of $\epsilon = 0.46$ was measured based on a cylindrical container of the packed bed that does not fulfill the condition $d_{\mathrm{R}} d_{\mathrm{Pa}}^{-1} > 40$. As a result, the provided void fraction was influenced by wall effects [88] and is not universally applicable. Because the cylindrical storage container employed in this work does fulfill the condition $d_{\mathrm{R}} d_{\mathrm{Pa}}^{-1} > 40$ and the particles are selected to be identically sized, the void fraction

Table 6.2: Material properties [120] of basalt chips without quartz content used as TES material in the form of a packed bed. Value for void fraction taken from [142].

mean specific heat capacity $\bar{c}_{p,\mathrm{Pa}}$ in J (kg K)$^{-1}$	mean specific thermal conductivity $\bar{\lambda}_{\mathrm{Pa}}$ in W (m K)$^{-1}$	density ρ_{Pa} in kg m^{-3}	void fraction (by volume) ϵ
1004	1.7	2950	0.40

suggested by Tsotsas [142] for loosely packed beds is chosen (Table 6.2). Moreover, for the mentioned constraints, the void fraction is independent from the packed bed particle sizes.

As motivated at the beginning of Chapter 4.2.1, heat losses to the environment are neglected because proper insulation of the cylindrical TES container is provided. Panels of microporous insulation materials ($\lambda_{\mathrm{iso}}|_{\Delta T=600\,\mathrm{K}} = 0.04\,\mathrm{W(mK)^{-1}}$ [63]) having a thicknesses of $l_{\mathrm{iso,side}} = 0.5\,\mathrm{m}$ at the side and $l_{\mathrm{iso,front}} = 2.0\,\mathrm{m}$ at the top and bottom front walls of the TES provide sufficient insulation [31, Chapter 5.1.3].

The amount of electrical energy to be stored using the PHES system determines the size of the TES systems. Its mass and volume can be calculated based on estimated mean temperature differences within the TES systems. As the temperature differences realized during cyclic steady-state operation are likely to differ from the estimations, the final size of the TES systems is adjusted based on simulation results.

6.1.4 Design point optimization to determine temperature and pressure levels

As motivated in detail in Section 6.1.1, setup 1 (Figure 6.1 a)) combined with working fluid air is chosen for the thermodynamic cycles of the PHES system. For the rejection of entropy to the environment, the working fluid is released at state HE5 to the environment and ambient air is entering the heat engine at state HE1. Furthermore, the minimum pressure within the PHES system is equal to the ambient pressure. The thermodynamic states defined by these constraints are summarized in Table 6.3.

The selection of the maximal temperature of the working fluid in the heat pump $T_{\mathrm{max,HP}}$ and the maximal pressure of the working fluid in the heat engine $p_{\mathrm{max,HE}}$ influences the round-trip efficiency of the PHES system. Figure 6.4 depicts the thermodynamic cycles of two PHES systems having equal maximal temperature $T_{\mathrm{max,HP}}$, equal minimal temperature T_{amb}, and equal minimal pressure p_{amb}, but different maximal pressures $p_{\mathrm{max,HE\,B}} > p_{\mathrm{max,HE\,A}}$. The higher the maximal pressure, the higher the exergy losses become in the turbomachinery. However, increasing the maximal pressure decreased the temperature difference bridged by the TES systems. This results in lower pressure drops and hence in lower exergy losses experienced by the working fluid passing through the TES systems. These reverse effects on the round-trip efficiency indicate the existence of an optimal maximal pressure.

The optimal temperature and pressure levels depend on the isentropic efficiencies of the turbomachinery, the working fluid pressure drop in the TES systems, and the efficiency of the TES systems. To determine the optimum, a simplified model of the PHES system is developed that calculates the round-trip efficiency of the PHES system for the steady state at design-point conditions. The simplified model will be referred to as optimization model and takes the following parameters into consideration:

1. the efficiencies of motor and generator,
2. the isentropic efficiencies of the turbomachinery,
3. the efficiencies of the TES systems,
4. the maximal temperature $T_{\mathrm{max,HP}} = T_{\mathrm{HP2}}$ that is reached by the working fluid in the heat pump,
5. the maximal pressure $p_{\mathrm{max,HE}} = p_{\mathrm{HE2}}$ that is reached by the working fluid in the heat engine, and
6. the pressure drop Δp_{TES} experienced by the working fluid in the TES systems.

Table 6.3: Fixed thermodynamic states of the PHES system. The ambient conditions are defined in Chapter 5.1. The nomenclature refers to setup 1 in Figure 6.1 a).

	HE1	HE5	HP1
pressure p	p_{amb}	p_{amb}	p_{amb}
temperature T	T_{amb}	-	-

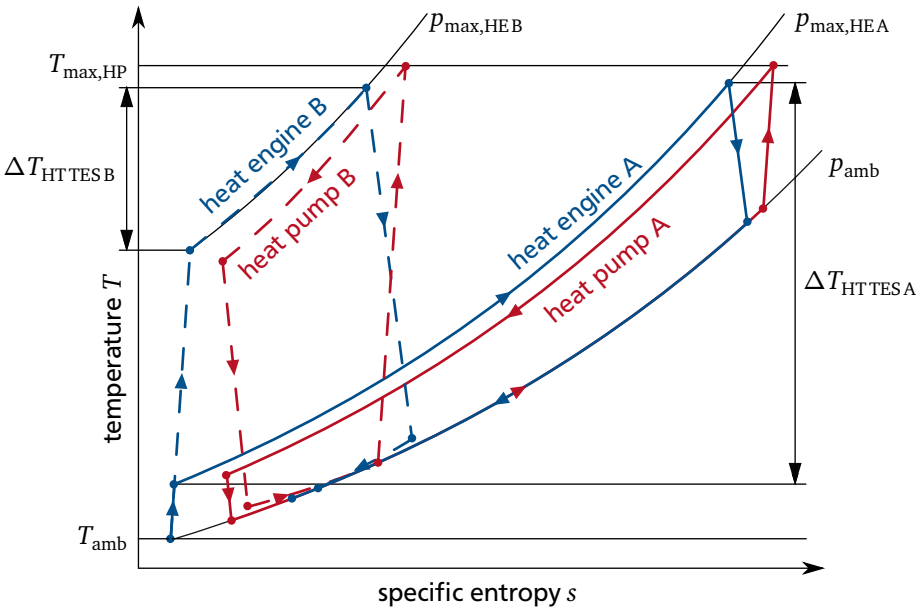

Figure 6.4: T,s-diagram of two PHES systems having equal maximal temperature $T_{\mathrm{max,HP}}$, equal minimal temperature T_{amb}, equal minimal pressure p_{amb}, but different maximal pressures $p_{\mathrm{max,HEB}} > p_{\mathrm{max,HEA}}$. Higher maximal pressures result in lower temperature differences ΔT_{TES} inside the TESs.

Table 6.4: Summary of component efficiencies of the Joule PHES system at the design point. The schematic of the PHES system is depicted in Figure 6.2.

component	efficiency	reference
motor	$\eta_{\mathrm{M}} = 0.96$	[130]
generator	$\eta_{\mathrm{G}} = 0.96$	[130]
compressor	$\eta_{s,\mathrm{C}} = 0.85$	[130; 135]
turbine	$\eta_{s,\mathrm{T}} = 0.90$	[130; 135]

According to currently available technology, the efficiencies of motor and generator as well as the isentropic efficiencies of the turbomachinery are listed in Table 6.4. All efficiencies are given for the design point which defines the optimal operating point of the components.

As a first step, the optimization model is used for a generic analysis in order to identify general rules governing the round-trip efficiency of the PHES system. The round-trip efficiency of the TES systems is approximated by imposing a minimum temperature drop of $\Delta T_{\mathrm{TES,min}} = 10\,\mathrm{K}$ between charging and discharging of the TES systems. The effect of the aforelisted parameters 4 to 6 on the round-trip efficiency at the design point is evaluated based on a parameter variation using the optimization model. Figure 6.5 illustrates the dependence of the PHES round-trip efficiency on the maximal pressure of the working fluid in the heat engine, influenced by different maximal temperatures of the working fluid in the heat pump and different TES pressure drops. The highest maximal round-trip efficiency that can possibly be reached increases with increasing maximal temperature $T_{\mathrm{max,HP}}$ and decreasing TES pressure drop Δp_{TES}. Consequently, the maximal temperature in the heat pump should be as high as possible and the TES pressure drop as low as possible. The maximal pressure of the working fluid in the heat engine that maximizes the PHES round-trip efficiency, depends on the actual values of $T_{\mathrm{max,HP}}$ and Δp_{TES}.

When the round-trip efficiency depicted in Figure 6.5 reaches zero, the electrical power generated by the heat engine drops to zero. This is caused by an equality of the mechanical power released by

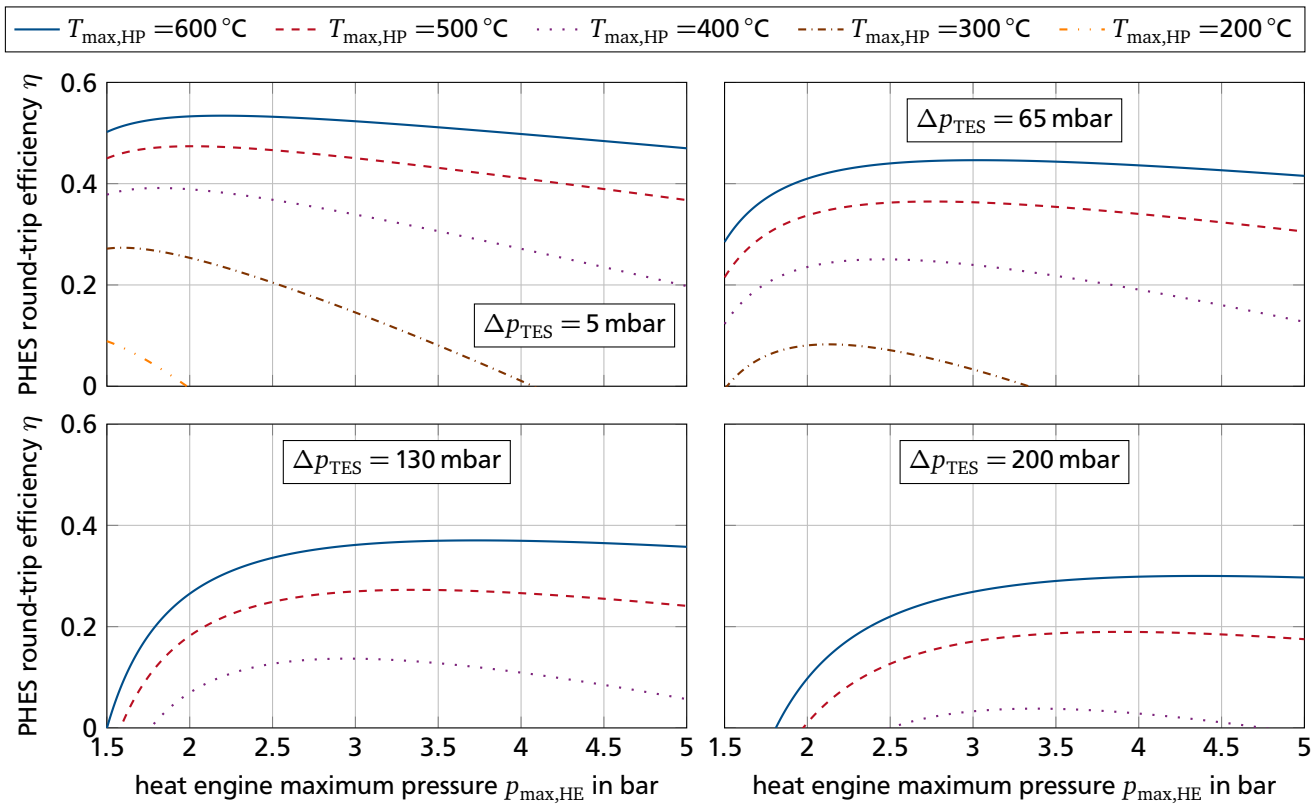

Figure 6.5: Estimated round-trip efficiency of the PHES system η depending on heat engine maximal pressure $p_{max,HE}$. The influence of the parameters TES pressure drop Δp_{TES} and heat pump maximal temperature $T_{max,HP}$ is illustrated.

the turbine of the heat engine and the mechanical power consumed by the compressor of the heat engine. Vanishing heat engine output powers are favored by low maximum pressures $p_{max,HE}$ combined with large TES pressure drops Δp_{TES} as well as high maximum pressures $p_{max,HE}$ combined with low isentropic efficiencies η_s.

Facing similar technological limitations as the ADELE project, the heat pump maximal temperature is selected to $T_{max,HP} = 600\,°C$ [85] (Chapter 2.3). For this maximal temperature, the influence of the TES pressure drop on maximum PHES round-trip efficiency η_{max} and the corresponding heat engine maximal pressure is depicted in Figure 6.6.

The dimensions and the composition of the TES systems as well as the working fluid flow conditions influence the performance of the TES systems in the form of pressure drop and outlet temperatures. These effects can only be captured by the transient simulation of the entire model of the PHES system. Therefore, as a second step, the optimization model is coupled with the detailed PHES system model as illustrated in Figure 6.7. In repeating loops, the output of the PHES system model serves as the input to the optimization model, and vice versa. The loop is exited when the output of both calculations is not subject to major changes any more.

The coupled optimization calculations reveal that the round-trip efficiency of the PHES system is more sensitive to a change in TES pressure drop than to a change in convective heat transfer coefficient between the storage material and the working fluid. Consequently, the diameter of the packed bed particles should be chosen as large as possible to minimize the pressure drop at the expense of a reduced convective heat transfer coefficient. However, the modeling approach chosen for the packed bed sensible heat TES system (Chapter 4.2.1) is based on the assumption of homogeneous temperatures within the

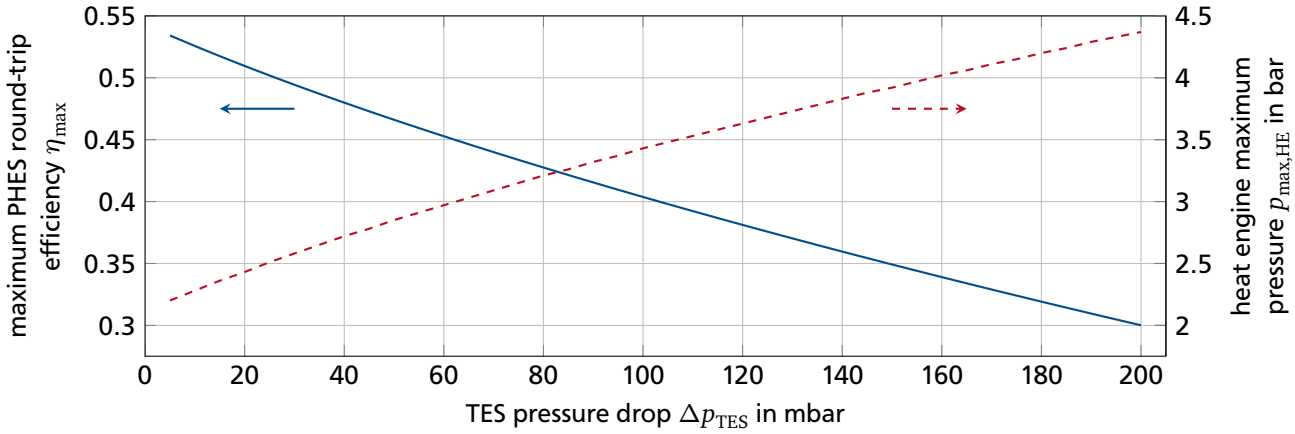

Figure 6.6: Maximum estimated round-trip efficiency of the PHES system η_{max} and the corresponding heat engine maximal pressure $p_{max,HE}$ over TES pressure drop Δp_{TES} for $T_{max,HP} = 600\,°C$.

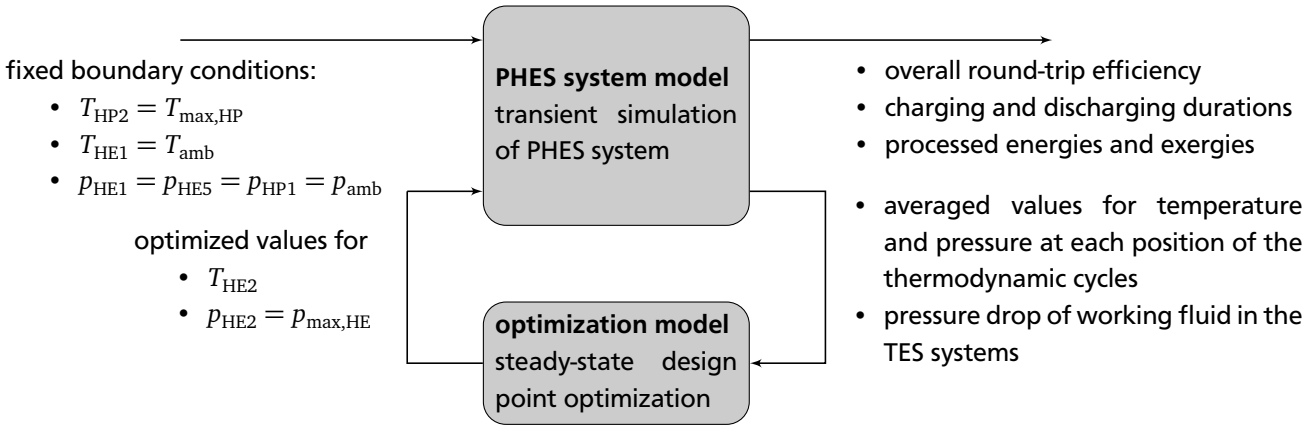

Figure 6.7: Procedure of coupling the PHES system model and the optimization model in order to determine optimal temperature and pressure levels.

particles, which results in the requirement of $Bi < 1$ and limits the maximal diameter of the packed bed particles. All particles selected in this work fulfill the condition $Bi < 0.73$.

Another parameter that should be discussed in detail is the outlet temperature of the working fluid leaving the high temperature TES system, because it influences both, the round-trip efficiency and the storage capacity of the PHES system. As described earlier, the temperature of the working fluid entering the high temperature TES needs to be kept constant during heat pump (charging) and heat engine (discharging) operation to enable the development of the cyclic steady state. Because the working fluid inlet and outlet temperatures to and from the low temperature TES adjust automatically to the PHES system operation, they cannot and do not have to be controlled.

During the heat pump operation of the PHES system (charging), the temperature of the working fluid leaving the high temperature TES system increases over time (Figure 6.8 a)). After a period of an almost constant outlet temperature it increases progressively until the heat pump operation is stopped. In theory, the outlet temperature of the working fluid could increase until it reaches the inlet temperature. However, with increasing outlet temperature, the heat flow transferred to the TES system decreases, resulting in decreasing energetic and exergetic efficiencies of the heat pump. Consequently, for a reasonable operation of the PHES system, the TES outlet temperatures do not reach the respective inlet temperatures. During the heat engine operation of the PHES system (discharging), the relation be-

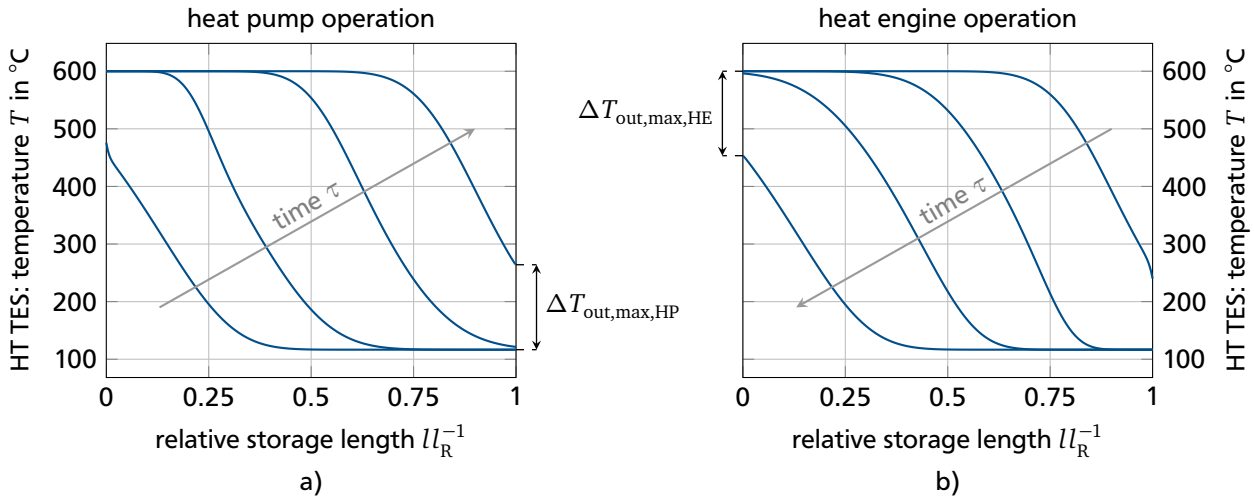

Figure 6.8: Time-dependent development of the temperature distribution inside the high temperature TES during heat pump a) and heat engine operation b). $\Delta T_{\mathrm{out,max}}$ indicates the maximum outlet temperature difference.

tween working fluid inlet and outlet temperature is reversed and the temperature of the working fluid leaving the high temperature TES system decreases over time (Figure 6.8 b)). With decreasing outlet temperature, the energetic and exergetic efficiency of the heat engine decreases.

The difference between the outlet temperature reached at the end of the charging (discharging) operation and the outlet temperature at the beginning of the charging (discharging) operation will be referred to as maximum outlet temperature difference $\Delta T_{\mathrm{out,max}}$

$$\Delta T_{\mathrm{out,max,HP}} = T_{\mathrm{HP3}}(\tau_{\mathrm{end\ HP}}) - T_{\mathrm{HP3}}(\tau_{\mathrm{begin\ HP}}) = T_{\mathrm{HP3}}(\tau_{\mathrm{end\ HP}}) - T_{\mathrm{HE2}}, \tag{6.6a}$$

$$\Delta T_{\mathrm{out,max,HE}} = T_{\mathrm{HE3}}(\tau_{\mathrm{begin\ HE}}) - T_{\mathrm{HE3}}(\tau_{\mathrm{end\ HE}}) = T_{\mathrm{HP2}} - T_{\mathrm{HE3}}(\tau_{\mathrm{end\ HE}}). \tag{6.6b}$$

Six identically parametrized PHES systems having identically parametrized TES systems only differing in $\Delta T_{\mathrm{out,max}}$ are simulated and evaluated. For the cyclic steady state, the temperature distributions inside the high and low temperature TES systems at the beginning, in the middle, and at the end of the heat engine operation are compared in Figure 6.9. In reverse order, the temperature distributions during the heat pump operation are qualitatively identical with almost negligible quantitative differences. The higher the maximum outlet temperature difference, the larger the slope of the temperature distribution is, which increases the storage capacity per unit of storage length. Additional performance data of the cyclic steady-state operation is summarized in Table 6.5.

With increasing maximum outlet temperature difference, the amount of stored thermal energy and the durations of heat pump (charging) as well as heat engine (discharging) operation increase. However, the energetic and exergetic efficiencies of heat pump, TES system, and heat engine as well as the round-trip efficiency of the PHES system decrease with increasing maximum outlet temperature difference $\Delta T_{\mathrm{out,max}}$.

For the maximum outlet temperature difference of 3 K, the cyclic-steady-state temperature distribution depicted in Figure 6.9 does barely change during the charging and discharging process. The developed temperature distribution does only allow for very short charging and discharging processes with small amounts of heat being transfered. Consequently, the corresponding performance data depicted in Table 6.5 is subject to large uncertainties.

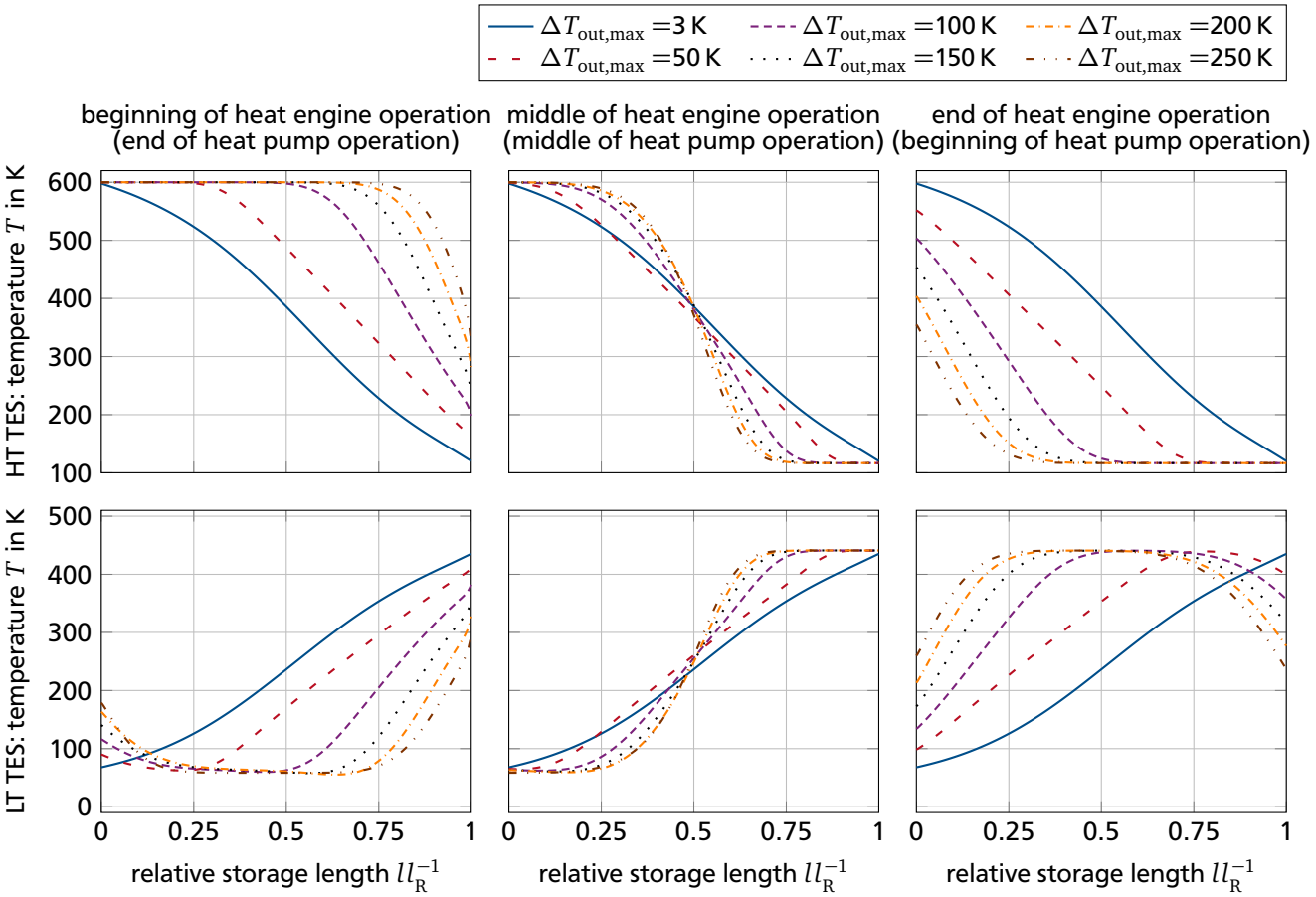

Figure 6.9: Comparison of temperature distributions in identical TES systems only differing in maximum outlet temperature differences $\Delta T_{\mathrm{out,max}}$ at different times in cyclic steady state.

Table 6.5: Performance data of identical PHES systems differing in maximum outlet temperature differences $\Delta T_{\mathrm{out,max}}$ in cyclic steady state.

$\Delta T_{\mathrm{out,max}}$ in K	3	50	100	150	200	250
duration of heat pump operation τ_{HP} in h	0.02	3.95	7.40	9.28	10.42	11.38
duration of heat engine operation τ_{HE} in h	0.02	3.98	7.10	8.63	9.50	10.15
electrical energy input $E_{\mathrm{el,in}}$ in MWh	0.49	50.0	93.2	117.8	134.0	143.4
electrical energy output $E_{\mathrm{el,out}}$ in MWh	0.21	21.5	38.3	46.3	50.2	52.8
exergetic efficiency of heat pump $\eta_{\mathrm{II,ex,HP}}$	0.81	0.80	0.80	0.79	0.79	0.79
exergetic efficiency of TES systems $\eta_{\mathrm{II,ex,TES}}$	0.84	0.86	0.84	0.82	0.81	0.81
exergetic efficiency of heat engine $\eta_{\mathrm{II,ex,HE}}$	0.63	0.62	0.62	0.60	0.59	0.58
round-trip efficiency of PHES system η_{PHES}	0.43	0.43	0.41	0.39	0.37	0.37

6.1.5 Chosen system designs

The operation of two different PHES systems based on Joule cycles is analyzed in this work. The design parameters of both systems are summarized in Table 6.6. Parameters that have a high influence on the round-trip efficiency of the PHES system have been identified in the previous section. These parameters are listed in Table 6.6 without indentation. The selection of all design parameters is described in the following.

Table 6.6: Summary of design parameters applied to both PHES systems based on Joule cycles analyzed in this work.

design parameters	Joule system 1	Joule system 2
$T_{\mathrm{max,HP}}$ in °C	600	600
$\dot{M}_{\mathrm{max}}$ in kg s^{-1}	110	110
$P_{\mathrm{el,in}}$ in MW	12.6	12.6
$E_{\mathrm{el,in}}$ in MWh	50.4	50.4
$\tau_{\mathrm{HP}} = \tau_{\mathrm{HE}}$ in h	4	4
$\Delta T_{\mathrm{out,max,HP}}$ in K	85.8	241.6
$\Delta T_{\mathrm{out,max,HE}}$ in K	28.0	103.7
$M_{\mathrm{R,HT\ TES}} = M_{\mathrm{R,LT\ TES}}$ in t	3650	1620
$d_{\mathrm{R,HT\ TES}} = d_{\mathrm{R,LT\ TES}}$ in m	13.80	13.80
$l_{\mathrm{R,HT\ TES}} = l_{\mathrm{R,LT\ TES}}$ in m	13.80	6.10
$d_{\mathrm{Pa,HT\ TES}} = d_{\mathrm{Pa,LT\ TES}}$ in mm	30	25
$p_{\mathrm{max,HE}}$ in bar	2.549	2.449

Data published by the ADELE project [66; 99; 158] is used as a reference for currently available technology in order to determine the maximal temperature and the maximal mass flow, which led to the selection of $T_{\mathrm{max,HP}}$ and $\dot{M}_{\mathrm{max}}$. Influenced by the maximum mass flow and based on the results by Krüger et al. [66], who investigated the economic feasibility of small scale adiabatic CAES systems, the electrical input power consumed by the heat pump $P_{\mathrm{el,in}}$ is set. Taking the charging and discharging duration τ into consideration, as defined in Section 5.2.3, yields the electrical energy consumed by the PHES system $E_{\mathrm{el,in}}$ during heat pump operation. All parameters introduced so far have identical values for both PHES systems to analyze.

Influencing both, the PHES round-trip efficiency and the size of the TES systems, the maximum outlet temperature differences $\Delta T_{\mathrm{out,max}}$ are chosen differently for system 1 and system 2. System 1 is characterized by relatively small maximum outlet temperature differences, which results in relatively large storages masses M_{R}. Minimizing the surface area of the cylindrical TES container (Figure 4.2 a)) for a fixed container volume, its diameter and height are given by

$$d_{\mathrm{R}} = l_{\mathrm{R}} = \sqrt[3]{\frac{4V_{\mathrm{TES}}}{\pi}} = \sqrt[3]{\frac{4V_{\mathrm{TES,Pa}}}{\pi(1-\epsilon)}} = \sqrt[3]{\frac{4M_{\mathrm{R}}}{\pi(1-\epsilon)\rho_{\mathrm{Pa}}}}. \tag{6.7}$$

In contrast, system 2 is characterized by relatively large maximum outlet temperature differences, which results in smaller storages masses M_{R}. To prevent a significant rise in pressure drop, the storage diameter d_{R} is adopted from system 1 and only the storage length l_{R} is reduced. The diameters d_{Pa} of the packed bed particles are chosen as large as possible in oder to reduce pressure drop and as small as necessary to yield acceptably small Biot numbers Bi. Small Biot numbers are required by the modeling approach of the packed bed sensible heat TES system to be valid.

Below an upper boundary that is far from being reached, the maximal pressure of the working fluid in the heat engine $p_{\mathrm{max,HE}}$ can be freely chosen. As presented in Chapter 6.1.4, $p_{\mathrm{max,HE}}$ has an optimal value that maximizes the round-trip efficiency of the PHES system. The optimal value of $p_{\mathrm{max,HE}}$ (Table 6.6) is determined by coupling the optimization model with the detailed PHES system model as illustrated in Figure 6.7.

The detailed analysis of system 1 and system 2 is presented in the following section. For both systems, heat transfer coefficients and model parameters of the packed bed sensible heat TES systems are summarized in Appendix A.1.

6.2 System analysis

The simulation results of system 1 and system 2 presented in this section are based on the characteristic operation scenario (Chapter 5.2.3) evaluated in cyclic steady state (Chapter 5.3). The design parameters of both systems, its boundary conditions, and design point efficiencies of the employed components are summarized in Tables 6.6, 6.3, and 6.4, respectively. Figure 6.2 b) depicts a schematic that is applicable to both PHES systems 1 and 2.

6.2.1 Exergy analysis

The time-dependent operation of heat pump during charging and heat engine during discharging of the PHES system is illustrated in Figure 6.10 for system 1 and Figure 6.11 for system 2, respectively. Each figure depicts the thermodynamic cycle of heat pump and heat engine in T,s-diagrams for five hourly shifted points in time, starting with the beginning of the operation period (time $\tau = 0\,\mathrm{h}$) and stopping with the end of the operation period (time $\tau = 4\,\mathrm{h}$). In accordance with the characteristic operation scenario (Chapter 5.2.3, Table 5.1), heat pump and heat engine are not operated at the same time. However, time τ is chosen to refer to the duration of heat pump and heat engine operation in order to facilitate comparisons between both operation modes. The relation between time τ of heat pump as well as heat engine operation and the entire operation period is illustrated in Figure 6.12.

For all points in time depicted in the T,s-diagrams in Figures 6.10 and 6.11, the thermodynamic states are summarized in Appendix A.2. During heat pump operation the high temperature TES is charged and the low temperature TES is discharged, which leads to varying TES outlet temperatures HP3 and HP1, respectively. The biggest change of the thermodynamic states takes place within the last hour of the heat pump operation. For the stability of the cyclic steady state, the temperature of the working fluid entering the high temperature TES (HP2) needs to remain constant during the entire operation period. A constant inlet temperature is achieved by adjusting the compressor compression ratio (HP1 $\rightarrow$ HP2). The heat engine thermodynamic cycle is subject to less temporal variations than the heat pump cycle because the thermodynamic state of the air entering from the environment (HE1) is constant. Furthermore, the heat engine maximum outlet temperature difference $\Delta T_{\mathrm{out,max,HE}}$ is smaller than the heat pump maximum outlet temperature difference $\Delta T_{\mathrm{out,max,HP}}$, which limits the temperature drop of HE3. Due to varying charging conditions of the low temperature TES, the temperature of the working fluid leaving the heat engine (HE5) changes over time. The T,s-diagram of system 2 is subject to higher temporal variation than that of system 1, because system 2 has larger maximum outlet temperature differences $\Delta T_{\mathrm{out,max}}$ than system 1 (Table 6.6).

The time curves of inlet, outlet and mean temperature distribution of the high and low temperature TES systems are depicted in Figure 6.12. In accordance with the characteristic operation scenario (Chapter 5.2.3) the PHES system is charged during heat pump operation between 1:00 h and 5:00 h and discharged during heat engine operation between 17:00 h and 21:00 h. As already mentioned, the working fluid inlet temperature to the high temperature TES stays constant during heat pump and heat engine operation. After remaining constant until approximately $\tau = 2\,\mathrm{h}$ of operation time, the working fluid outlet temperature of the high temperature TES deviates in the direction of the inlet temperature. The maximum deviation is defined by the maximum outlet temperature difference

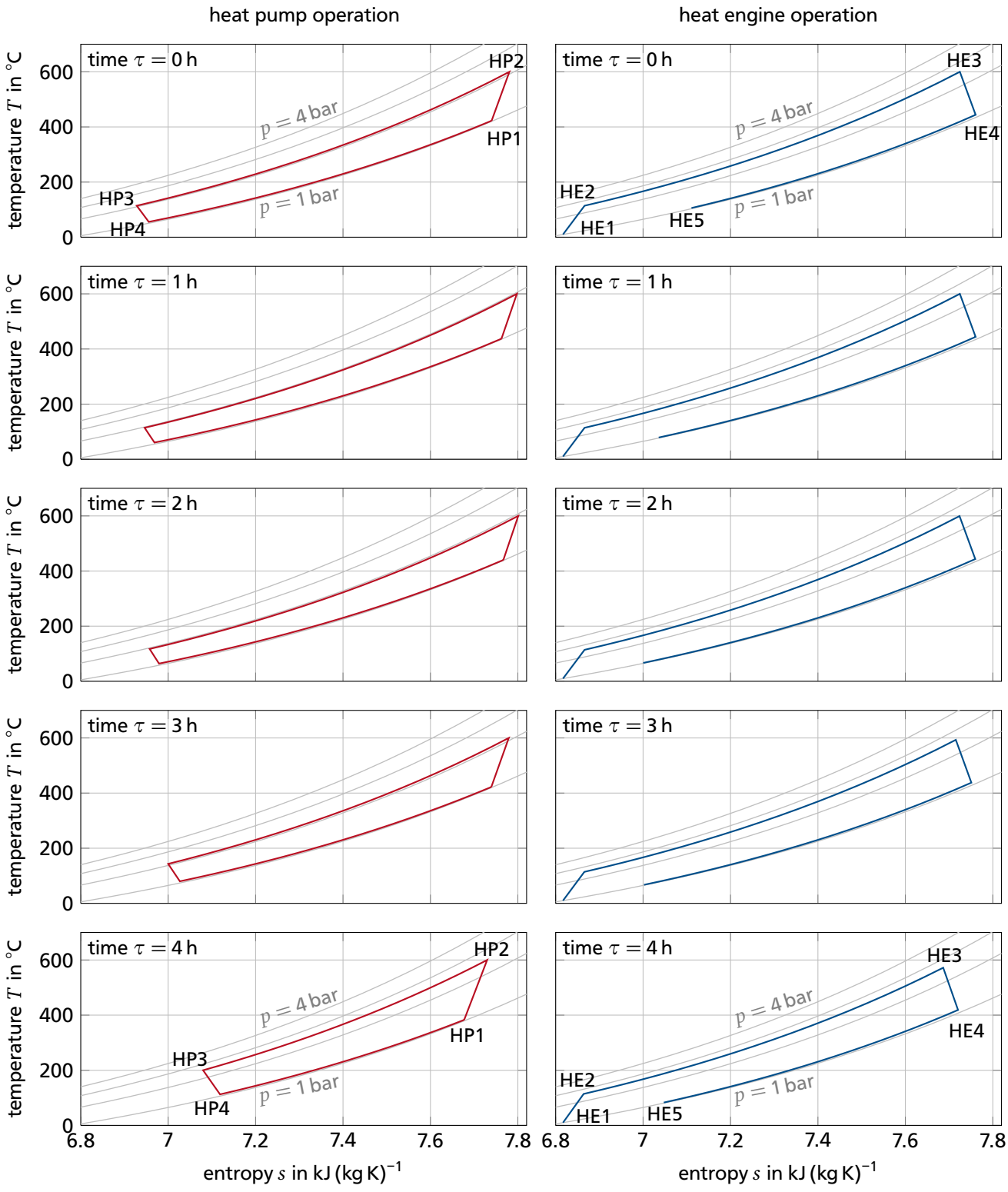

Figure 6.10: System 1: Comparison of the heat pump and heat engine cycles in the T,s-diagram at different times τ. The times τ report the duration of the corresponding operation period.

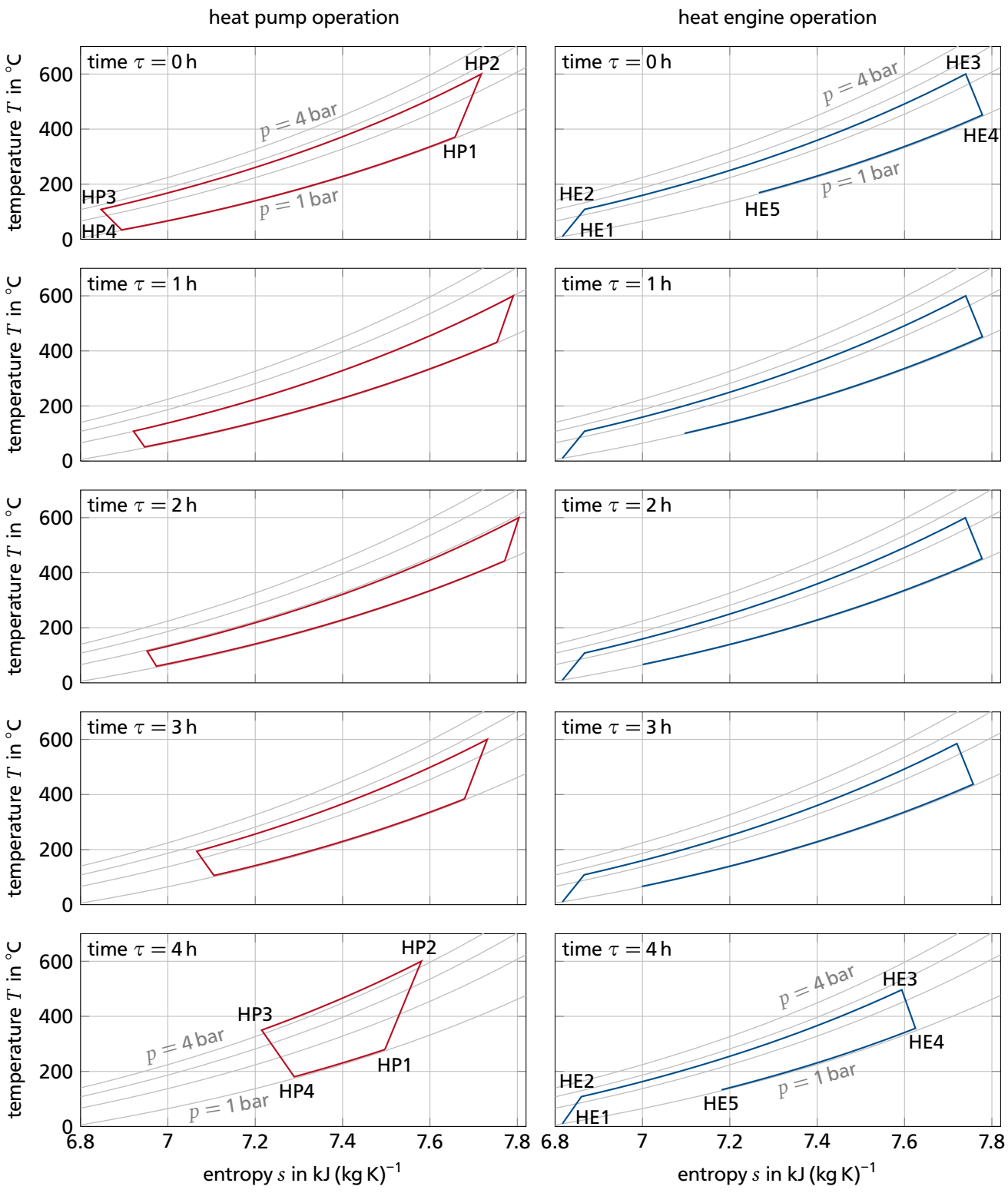

Figure 6.11: System 2: Comparison of the heat pump and heat engine cycles in the T, s-diagram at different times τ. The times τ report the duration of the corresponding operation period.

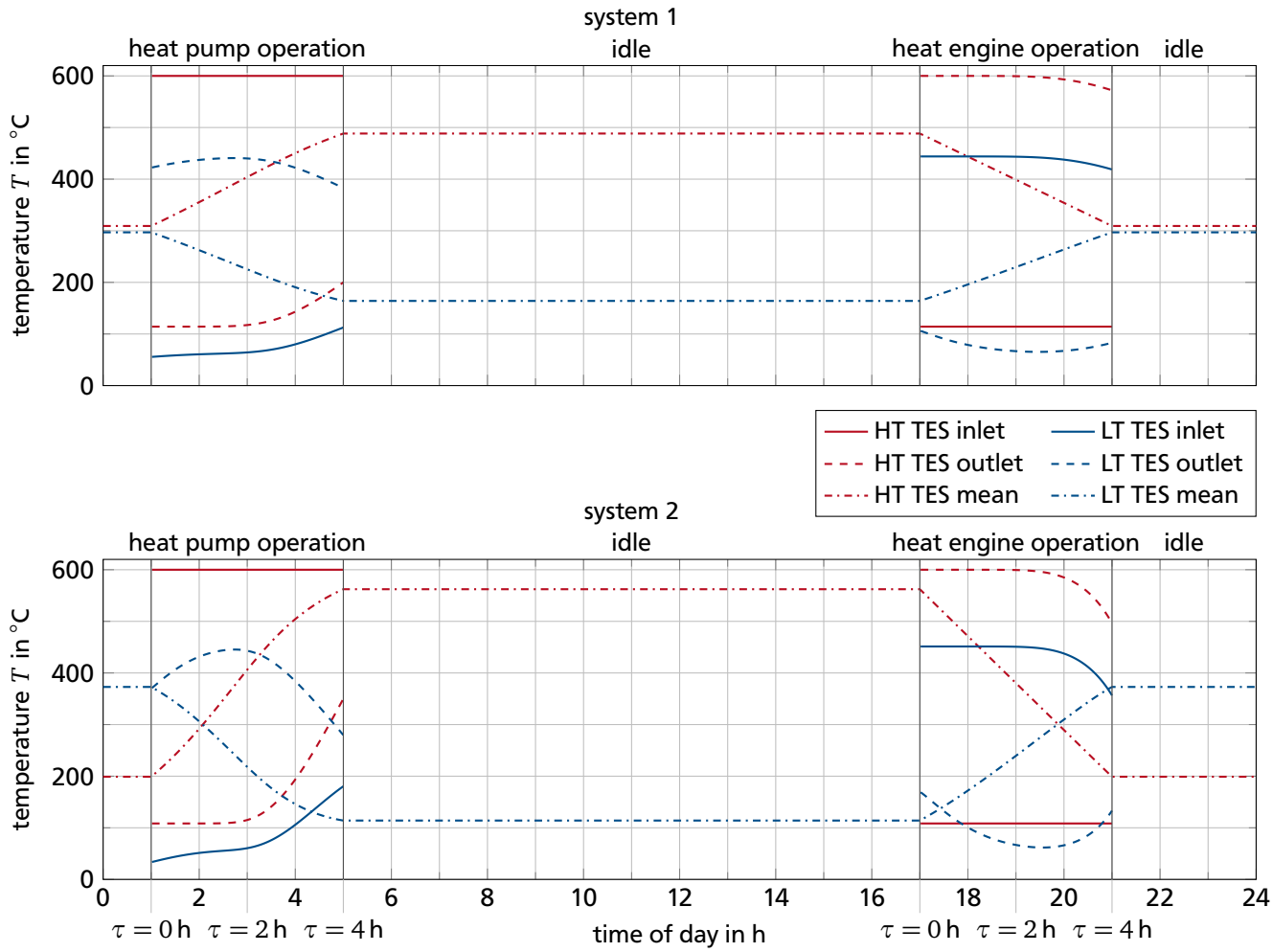

Figure 6.12: Time curves of inlet, outlet, and mean temperature of the high and low temperature TES.

Table 6.7: Summary of the differences in mean TES temperature for system 1 and system 2.

	system 1	system 2
$\Delta T_{\mathrm{mean,\ HT\ TES}}$ in K	179.1	363.3
$\Delta T_{\mathrm{mean,\ LT\ TES}}$ in K	132.9	258.9

$\Delta T_{\mathrm{out,max,HP}} > \Delta T_{\mathrm{out,max,HE}}$. The inlet and outlet temperatures of the working fluid passing through the low temperature TES adjust automatically to the operation conditions of the PHES system. The inlet temperature increases during heat pump and decreases during heat engine operation. It is apparent that these inlet temperatures follow the outlet temperatures of the high temperature TES. The outlet temperatures of the working fluid leaving the low temperature TES reach a maximum during heat pump operation and a minimum during heat engine operation, respectively. The time curves of system 2 are subject to higher variations than the time curves of system 1, which can also be attributed to the larger maximum outlet temperature differences $\Delta T_{\mathrm{out,max}}$ of system 2 compared to system 1.

Across the heat pump and heat engine operation periods, the mean temperatures of the high and low temperature TES are subject to differences $\Delta T_{\mathrm{mean,TES}}$ which are summarized in Table 6.7 for both systems. The differences in mean temperature allow for two conclusions. First, system 2 has a higher TES utilization than system 1. Second, being equally sized, the high temperature TES systems store more thermal energy and more exergy than the low temperature TES systems.

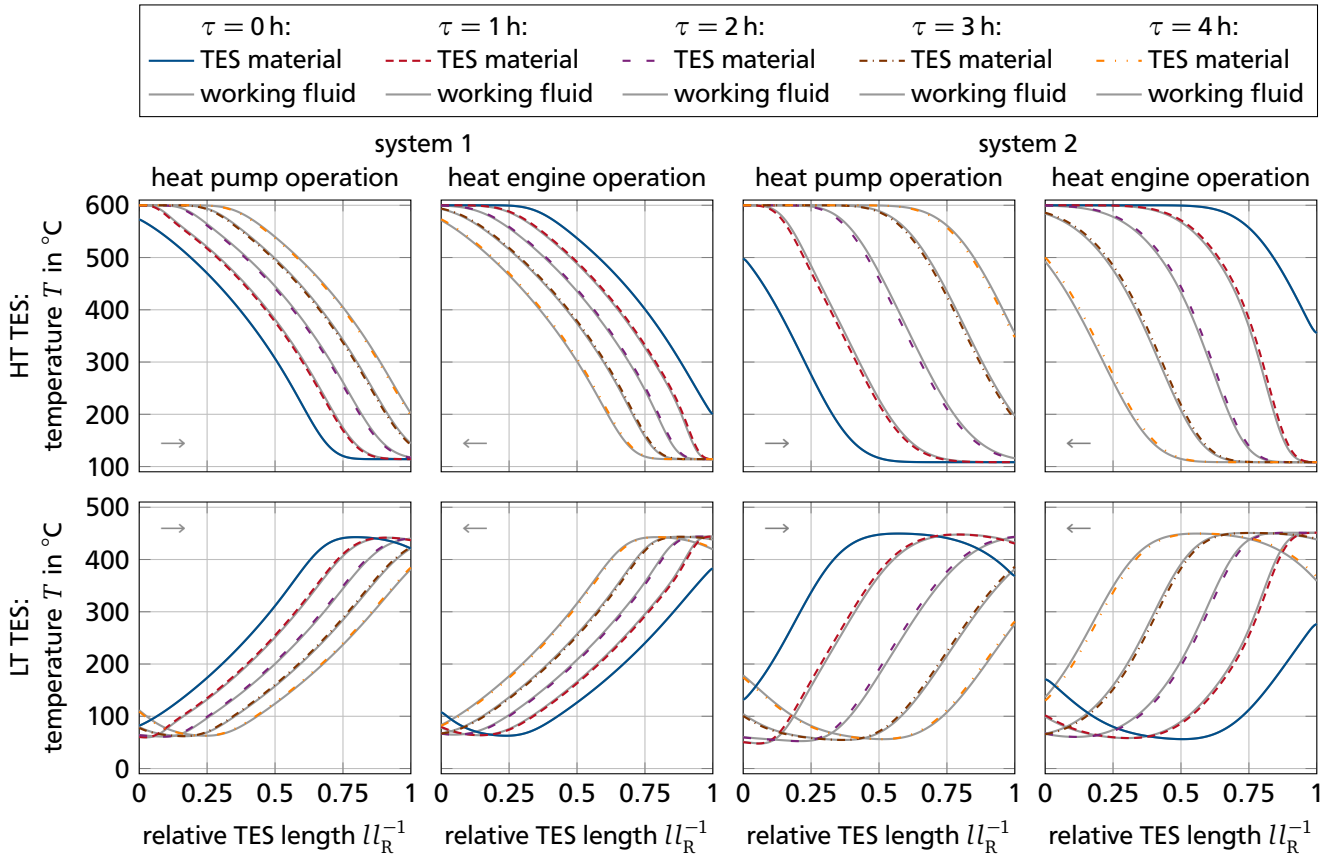

Figure 6.13: Comparison of temperature distributions of working fluid and storage material inside the high and low temperature TES systems at different times τ during the heat pump and heat engine operation. The times τ report the duration of the corresponding operation period. The gray arrow indicates the flow direction of the working fluid through the TES.

Figure 6.13 depicts the temperature distribution of working fluid and storage material along the longitudinal axis of the TES systems at different times τ. A small gray arrow indicates the working fluid flow direction. The constant inlet temperature of the working fluid during heat pump and heat engine operation results in the development of a stratified temperature distribution inside the high temperature TES. Because the low temperature TES inlet temperature varies with time, a stratified temperature distribution does not develop. Close to the inlet and outlet of the low temperature TES systems, the temperature gradient is reversed.

The temperature distributions in Figure 6.13 illustrate the higher TES utilization of system 2 compared to system 1. Consequently, the high temperature TES of system 2 has larger regions that reach the maximum and minimum storage temperatures. Taking into consideration that the TES systems of system 1 are more than twice as long as those of system 2 (Table 6.6), the regions reaching the maximum and minimum temperatures are approximately of equal absolute size. However, in the region between the temperature maxima, the temperature change per storage length is larger in the TESs of system 2 than in the TESs of system 1. The larger the temperature change per storage length, the better the storage utilization is. In contrast, large ratios of storage utilization are coupled to larger temperature differences between TES material and working fluid, as depicted in Figure 6.13. Table 6.8 summarizes averaged mean and averaged maximum temperature differences between working fluid and storage material for both PHES systems. Mean and maximum temperature difference are determined for the entire storage

Table 6.8: Averaged mean and maximum temperature difference between working fluid and TES material for the high and low TES during heat pump and heat engine operation.

		heat pump operation		heat engine operation	
		$\overline{\Delta T_{\mathrm{mean}}}$ in K	$\overline{\Delta T_{\mathrm{max}}}$ in K	$\overline{\Delta T_{\mathrm{mean}}}$ in K	$\overline{\Delta T_{\mathrm{max}}}$ in K
system 1	HT TES	3.1	6.0	3.1	8.5
	LT TES	2.6	4.7	2.6	6.5
system 2	HT TES	4.7	12.5	4.9	18.6
	LT TES	4.4	10.5	4.4	15.3

at each simulation time step ($\Delta\tau = 60\,\mathrm{s}$). The results are averaged over the entire heat pump and heat engine operation period. To conclude, the averaged temperature differences are small for both PHES systems, indicating large convective heat transfer coefficients between working fluid and TES material (Appendix A.1).

Figure 6.14 contains various graphs illustrating the transient operation of the PHES systems. Energetic and exergetic efficiencies of the heat pump are illustrated in Figure 6.14 a) and c), energetic and exergetic efficiencies of the heat engine are illustrated in Figure 6.14 b) and d). The same efficiencies are depicted in plots with two different scalings in order to completely visualize the distributions. Based on the efficiency definitions presented in Chapter 5.4, the heat pump efficiencies η_{I} exceed unity, while all efficiencies η_{II} have an upper boundary of unity. The efficiency peak of η_{I} during heat pump operation results from the temperature maximum of the working fluid leaving the low temperature TES (Figure 6.12), because the definition of η_{I} does not account for the energy and exergy being supplied to the heat pump by the low temperature TES. In contrast, the efficiency peak of η_{II} during heat engine operation results from the temperature minimum of the working fluid leaving the low temperature TES (Figure 6.12). The definition of η_{II} counts the energy and exergy being deposited in the low temperature TES as useful product of the heat engine. The deposition reaches a maximum when the low temperature TES outlet temperature reaches a minimum.

The transient heat pump efficiencies of system 1 and system 2 reach approximately the same maxima at the same operation time. However, at the beginning and at the end of the operation periods the efficiencies of system 2 experience a larger drop than the efficiencies of system 1. The transient heat engine efficiencies of system 1 and system 2 show a similar trend. As the thermodynamic cycle of system 2 (Figure 6.11) is subject to larger temporal variations than the thermodynamic cycle of system 1 (Figure 6.10), the efficiency of system 2 is reduced by more distinct off-design operation.

The mass flow $\dot{M}$ through heat pump and heat engine (Figure 6.14 e) and f)) is adjusted with the objective of providing a constant demand for electrical energy by the heat pump as well as a constant supply of electrical energy by the heat engine (Figure 6.14 g) and h)). Towards the end of the heat pump operation, the shaft power of turbine and compressor increase (Figure 6.14 g)), because the pressure ratio Π bridged by turbine and compressor increases (Figure 6.14 i)). The increase in pressure ratio, however, originates from the requirement to achieve a constant high temperature TES inlet temperature HP2 (Figure 6.12). The slight increase in turbine and compressor shaft power towards the end of the heat engine operation (Figure 6.14 h)) is caused by the increase in mass flow due to the decrease in turbine inlet temperature HE3 (Figure 6.12). Turbine and compressor pressure ratio stay constant during the heat engine operation (Figure 6.14 j)) and therefore are not responsible for the increase in shaft power. In accordance with the modeling approach chosen (Chapter 4.2.1), the pressure drop Δp experienced by the working fluid at its passage through the TES systems (Figure 6.14 k) and l)) follows the development of the working fluid mass flow (Figure 6.14 e) and f)).

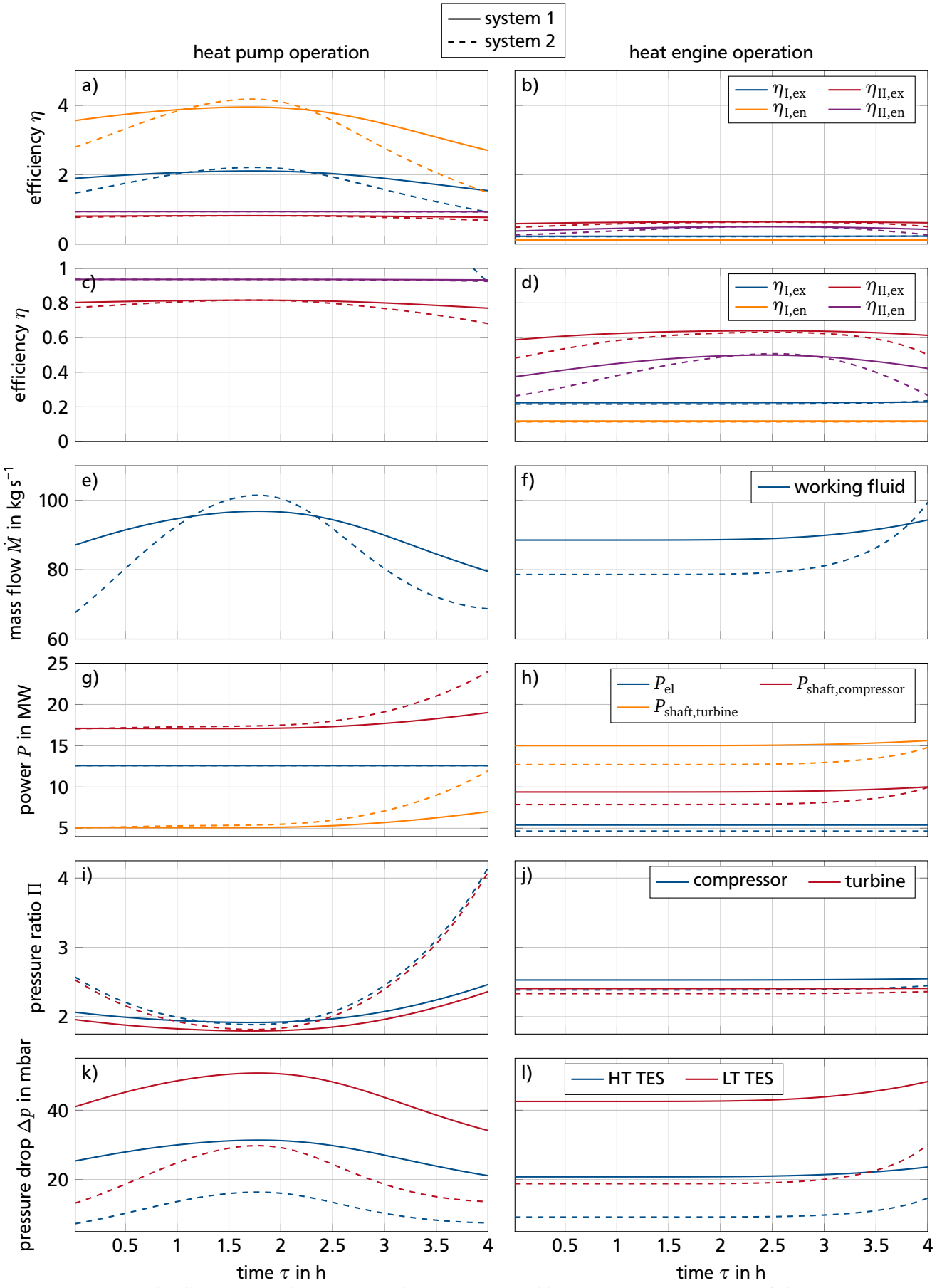

Figure 6.14: Graphs illustrating the transient heat pump and heat engine operation of the PHES systems. The graphs of system 1 and system 2 are printed in black and gray, respectively.

Table 6.9: Exergy and energy being consumed and released by the PHES system as well as exchanged between its subsystems.

			$Q_{\mathrm{HP}\rightarrow\mathrm{TES}}$		$Q_{\mathrm{TES}\rightarrow\mathrm{HE}}$			
		$En_{\mathrm{el,in}}$	$Q_{\mathrm{HP}\rightarrow\mathrm{HT\ TES}}$	$Q_{\mathrm{LT\ TES}\rightarrow\mathrm{HP}}$	$Q_{\mathrm{HT\ TES}\rightarrow\mathrm{HE}}$	$Q_{\mathrm{HE}\rightarrow\mathrm{LT\ TES}}$	$M_{\mathrm{HE5}\rightarrow\mathrm{amb}}$	$En_{\mathrm{el,out}}$
system 1	E in MWh		40.53		34.50			
	(En in MWh)		(47.13)		(47.13)			
		50.40	98.38	57.85	96.11	61.61	2.43	21.60
		(50.40)	(182.52)	(135.39)	(182.52)	(135.39)	(23.64)	(21.60)
system 2	E in MWh		39.37		31.79			
	(En in MWh)		(47.05)		(47.05)			
		50.40	88.76	49.39	85.29	53.50	3.56	18.60
		(50.40)	(163.63)	(116.59)	(163.63)	(116.59)	(26.83)	(18.60)

The performances of the two PHES systems show that system 1 is subject to smaller temporal variations but higher levels of mass flow $\dot{M}$ and TES pressure drop Δp than system 2. Also subject to smaller variations but lower levels are the compressor and turbine pressure ratios Π during heat pump operation of system 1 compared to system 2.

The amounts of energy and exergy that are consumed and released by the PHES system as well as exchanged between its subsystems are summarized in Table 6.9. In addition to the amounts of exergy (energy) exchanged with the high and low temperature TES systems, the net amounts exchanged with the entire TES subsystem are listed (HP→TES, TES→HE). These net amounts of exergy (energy) are defined in Equation (5.5) and will especially be considered in the evaluation of the PHES system and subsystem performance. Table 6.9 illustrates that electrical energy completely consists of exergy, whereas the exergy content of heat (at a finite temperature) is smaller than its energy content. Because the TES systems are modeled adiabatically, the amount of energy entering and leaving the TES systems is conserved. Originating from working fluid pressure losses and from heat transfer at finite temperature differences, the amount of exergy entering the TES systems is larger than the amount of exergy leaving the TES systems. In order to release the entropy generated in the PHES system, the heat pump discharges working fluid to the environment ($M_{\mathrm{HE5}\rightarrow\mathrm{amb}}$). Larger than the amount of electrical energy supplied by the heat engine, the discharged working fluid contains a considerable amount of energy. However, solely originating from temperatures being moderately above ambient temperature, its exergy content is rather small. From electrical energy input to electrical energy output, PHES system 1 conserves more exergy than PHES system 2.

For all components, the subsystems and the entire PHES systems, Table 6.10 summarizes energetic and exergetic efficiencies, the underlying product and fuel definitions, as well as the exergy destruction integrated over the entire operation period. The energetic efficiency is not suitable for comparisons of single components, because it does not show large variations in performance. The exergetic efficiency and the exergy destruction, however, reveal that compressors and turbines have a lower system performance than the motor/generator set.

Comparing the subsystems, the definition of exergetic efficiencies according to Equation (5.6) should be employed, which is indicated by superscript 2 in Table 6.10. For both PHES systems, the TES systems have the highest exergetic efficiencies, followed by heat pump and heat engine. The exergy destruction indicates the same trend. The relatively low exergy destruction of the TES systems is caused by two effects. First, the temperature difference between working fluid and storage material during charging and discharging is small (Table 6.8). Second, the thermal conductivity between the particles of the TES

Table 6.10: Integrated exergy destruction, product and fuel definitions as well as energetic and exergetic efficiencies for the components, the subsystems, and the entire PHES systems. The nomenclature of the components and attached fluid pipes, electrical leads, and mechanical shafts follows Figure 6.2 b).

			system 1			system 2		
com-ponent	fuel definition	product definition	η_{en}	η_{ex}	E_D in MWh	η_{en}	η_{ex}	E_D in MWh
C_{HP}	me1 + me2	HP2 − HP1	0.990	0.933	4.67	0.990	0.930	5.15
T_{HP}	HP3 − HP4	me2	0.990	0.885	2.85	0.990	0.880	3.53
M	el,in	me1	0.953	0.953	2.35	0.953	0.953	2.35
HT TES	HP2 − HP3	HE3 − HE2	1.000	0.977	2.27	1.000	0.961	3.47
LT TES	HE4 − HE5	HP1 − HP4	1.000	0.939	3.76	1.000	0.923	4.11
C_{HE}	me3 − me4	HE2 − HE1	0.990	0.859	5.35	0.990	0.849	4.90
T_{HE}	HE3 − HE4	me3	0.990	0.935	4.23	0.990	0.929	3.95
G	me4	el,out	0.960	0.960	0.90	0.960	0.960	0.77
HP[1]	el,in	HP2 − HP3	3.621	1.952	9.87	3.247	1.761	11.03
TES[1]	HP2 − HP3	HE3 − HE2	1.000	0.977	6.03	1.000	0.961	7.58
HE[1]	HE3 − HE2	el,out	0.118	0.225	12.90	0.114	0.218	13.19
HP[2]	el,in	HP2 − HP3 − (HP1 − HP4)	0.935	0.804	9.87	0.934	0.781	11.03
TES[2]	HP2 − HP3 − (HP1 − HP4)	HE3 − HE2 − (HE4 − HE5)	1.000	0.851	6.03	1.000	0.807	7.58
HE[2]	HE3 − HE2 − (HE4 − HE5)	el,out	0.458	0.626	12.90	0.395	0.585	13.19
PHES	el,in	el,out	0.429	0.429	28.8	0.369	0.369	31.80

[1] product and fuel definition according to Equation (5.4)
[2] product and fuel definition according to Equation (5.6)

is small (Appendix A.1), which impairs the degradation of the temperature profile within the TES during the idle time. For comparisons with energetic efficiencies of conventional heat pumps and heat engines, the energetic subsystem efficiencies according to definition (5.4) should be employed.

All energetic and exergetic efficiencies of components and subsystems of system 1 are larger than or at least equal to the corresponding efficiencies of system 2. Consequently, the overall round-trip efficiency of PHES system 1 is larger than the round-trip efficiency of PHES system 2. In conclusion, PHES system 1 is characterized by smaller maximum outlet temperature differences, resulting in smaller variations of the thermodynamic cycle, smaller exergy destructions, and hence a higher round-trip efficiency than system 2. The considerable efficiency plus of 6 percentage points is gained by using TES systems that are more than twice as large (by volume and mass) as those of PHES system 2.

The propagation of exergy through the PHES systems 1 and 2 is visualized in the Sankey diagrams in Figures 6.15 and 6.16, respectively. For a complete overview of the PHES system performance, exergetic efficiencies are also listed. The Sankey diagrams exemplify that a multiple of the exergy entering and leaving the PHES system is stored in the TES systems. Furthermore, the propagation of exergy through the PHES system illustrates that the low temperature TES is an important component. Without the low temperature TES being present, the heat engine would release a substantial amount of exergy to the environment. This exergy would be missing during heat engine operation, approximately cutting the round-trip efficiency in half.

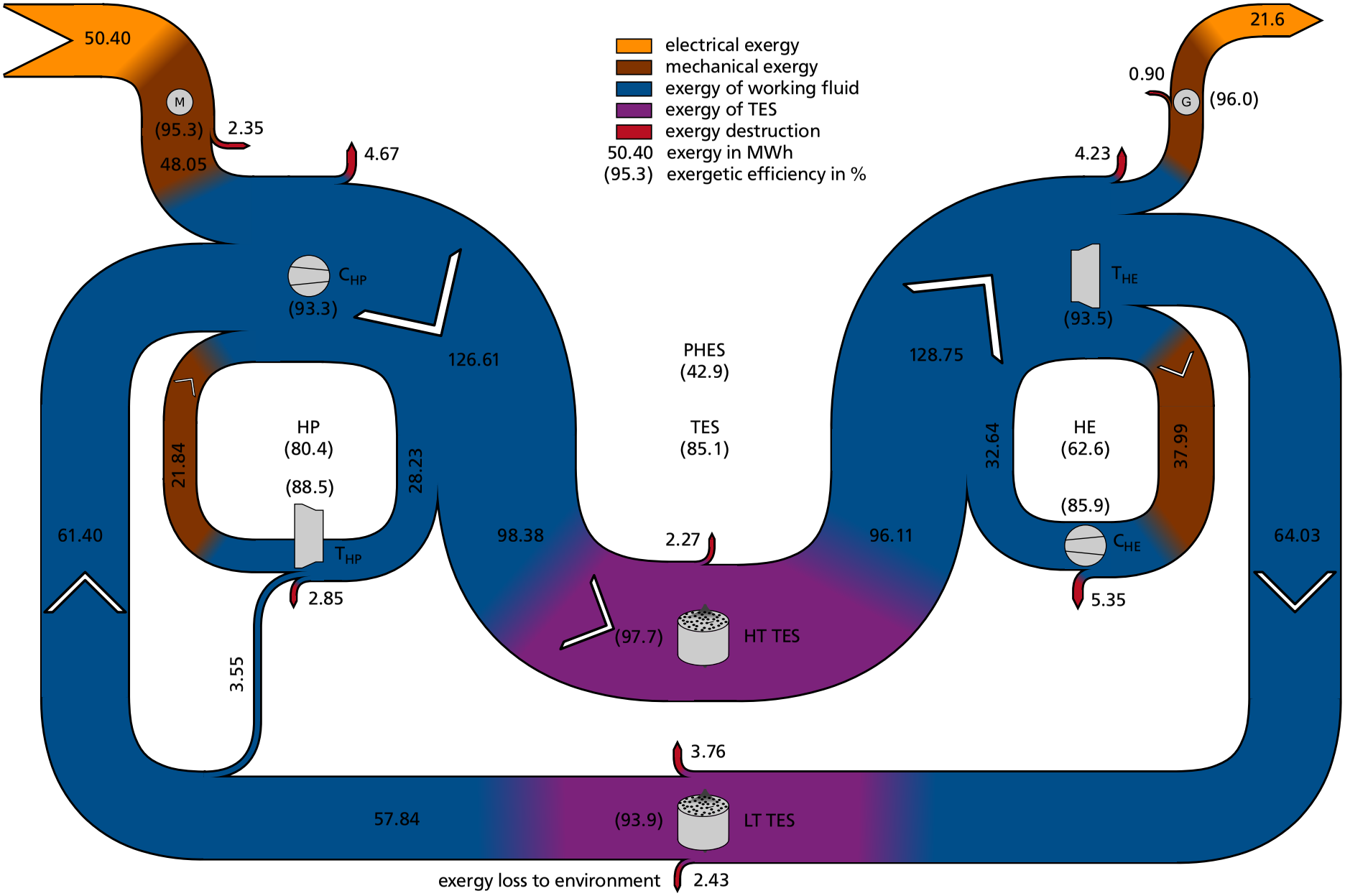

Figure 6.15: Sankey diagram visualizing the propagation of exergy through PHES system 1.

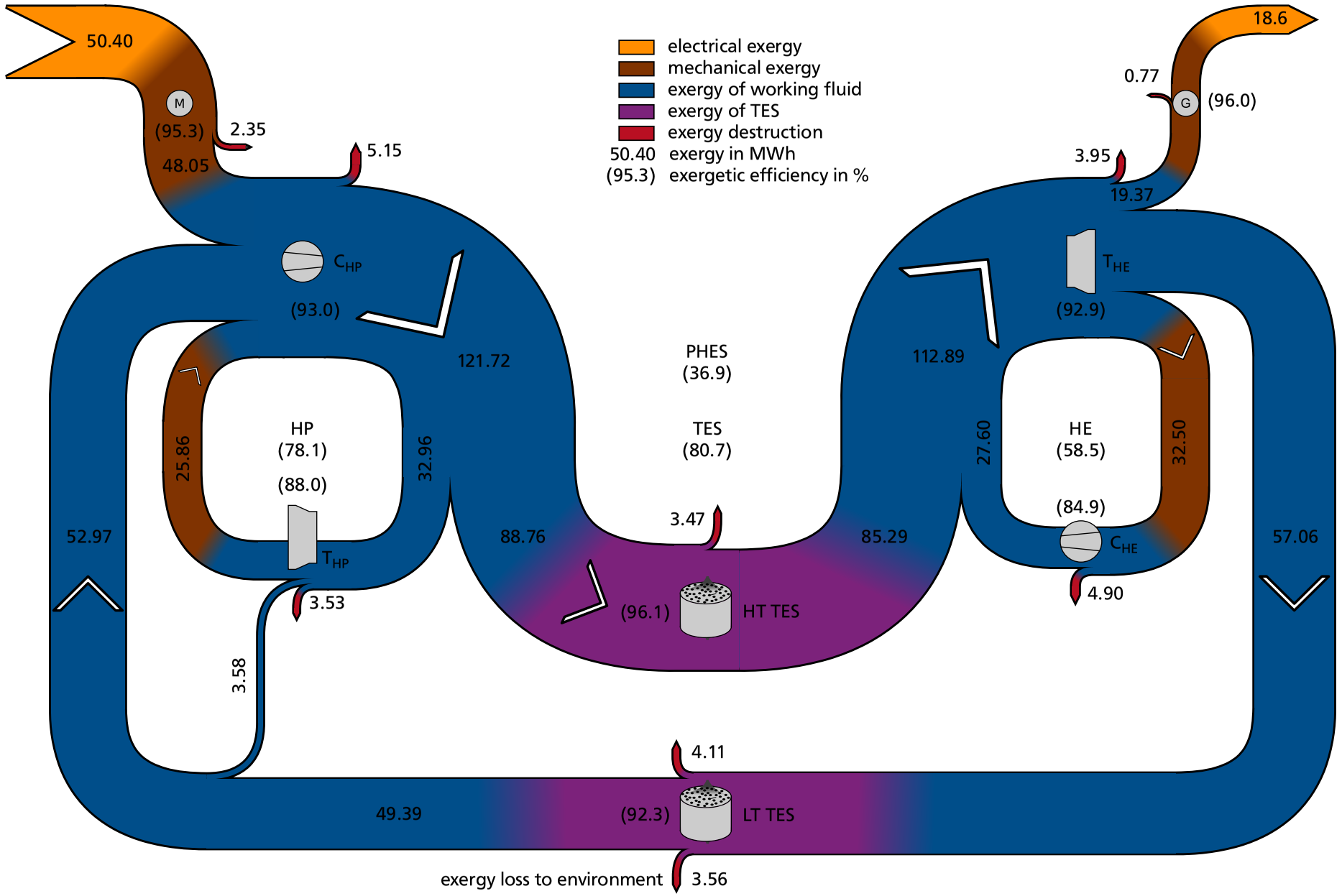

Figure 6.16: Sankey diagram visualizing the propagation of exergy through PHES system 2.

6.2.2 Economic analysis

As described in Chapter 4.4.2, the determination of purchased equipment costs is challenging due to the scarcity of reliable data. Consequently, the purchased equipment costs determined for most of the components employed in this work draw on cost correlations by Turton et al. [144, Appendix A] and Towler et al. [140, Chapter 7].

The purchased equipment costs Z^{PEC} and the capacity/size as well as fitting parameters used for their determination are summarized in Table 6.11 for all components of the PHES systems. In addition, annual component costs Z^{an} and the component costs per operation period Z^{OP} are given in Table 6.11. Based on the conversion expressed in Equation (4.73), all costs are provided in Euro for the reference year 2016. The purchased equipment cost of turbine and generator are solely determined with the parameters given in Table 6.11.

For the TES systems, the capacity/size as well as fitting parameters given in Table 6.11 determine the costs attributed to the casing only. Adding the costs for the storage material yields the total purchased equipment costs for the TES systems, as given in Table 6.11. For the required packed bed particle sizes, current prices for basalt chips as TES material range between $100\,€\,\mathrm{t}^{-1}$ and $200\,€\,\mathrm{t}^{-1}$ [10; 91]. Due to increased demands regarding homogeneously sized particles the upper price boundary is chosen. Costs for the insulation of the TES systems are not considered separately, which also justifies the selection of the upper price boundary.

Because a motor/generator set is not contained in the cost correlations by Turton et al. and Towler et al., the scaling equation (4.71) is employed to determine the purchased equipment costs. The scaling exponent K_1 is calculated based on performance and cost data by Balli et al. [8] (Table 6.12).

Table 6.11: Purchased equipment costs, annual costs and costs per operation period for each component of the PHES systems. In addition, the chosen approach and the capacity/size as well as fitting parameters are given.

	component	correlation equation	K_1	K_2	K_3	A	Z^{PEC} in k€	Z^{an} in k€	Z^{OP} in k€
system 1	compressor	(4.70)	$580 \cdot 10^3$	$20 \cdot 10^3$	0.6	19.1 MW	7362	539.2	1.477
	turbine	(4.69)	−21.7702	13.2175	−1.5279	15.7 MW	7570	554.4	1.519
	motor/generator	(4.71)	0.6196	-	-	12.7 MW	597	43.7	0.120
	HT TES	(4.70)	5800	1600	0.7	2065 m^3	1043	76.4	0.209
	LT TES	(4.70)	5800	1600	0.7	2065 m^3	1043	76.4	0.209
system 2	compressor	(4.70)	$580 \cdot 10^3$	$20 \cdot 10^3$	0.6	24.0 MW	8357	612.1	1.677
	turbine	(4.69)	−21.7702	13.2175	−1.5279	14.9 MW	7401	542.1	1.485
	motor/generator	(4.71)	0.6196	-	-	12.7 MW	597	43.7	0.120
	HT TES	(4.70)	5800	1600	0.7	913 m^3	502	36.7	0.101
	LT TES	(4.70)	5800	1600	0.7	913 m^3	502	36.7	0.101

Table 6.12: Performance and cost data [8] used to determine the scaling exponent for the motor/generator purchased equipment costs.

	P_{el} in MW	Z^{PEC} in k$
motor/generator 1	15.6	800
motor/generator 2	36.3	1350

The annual component costs Z^{an} result from leveling the purchased equipment costs over the entire projected operating time of n^{an} years under consideration of a compounded interest rate i and an annual operation and maintenance cost factor γ (Equation (4.74), Table 4.11). Finally, dividing the annual component costs by the amount of operation cycles per year N^{an}, as defined in Chapter 5.2, yields the component costs per operation period Z^{OP} (Equation (4.75)).

As input parameters to the exergoeconomic analysis, the component costs per operation period represent cost sources within each component. According to the chosen system design (Figure 6.2 b)), heat pump and heat engine share compressor, turbine, and motor/generator. Therefore, half of the component costs per operation period of these components is assigned to the heat pump and the other half is assigned to the heat engine. The specific costs for electrical energy consumed by the heat pump amount to $c_{\mathrm{el,in}} = 19.66\,€\,(\mathrm{MWh})^{-1}$, as determined in Chapter 5.2.3.

6.2.3 Exergoeconomic analysis

Employing the model introduced in Chapter 4.4.3, the results of the exergoeconomic analysis based on the characteristic operation of PHES systems 1 and 2 in cyclic steady state are presented in the following. The auxiliary equations and boundary conditions necessary to solve the linear system of equations formed by cost balances around each component are listed in Table 6.13.

The results of the exergoeconomic analysis are summarized in Table 6.14 for the heat pump cycle and in Table 6.15 for the heat engine cycle of systems 1 and 2. The specific costs per exergy defined as boundary conditions (Table 6.13) are equal for PHES system 1 and system 2. Because the exergy

Table 6.13: Auxiliary equations and boundary conditions for the exergoeconomic analysis of PHES systems 1 and 2.

auxiliary equations	description
$c_{\mathrm{HP2}} = c_{\mathrm{HP3}}$	constant exergy-specific costs of working fluid passing the HT TES
$c_{\mathrm{HP3}} = c_{\mathrm{HP4}}$	constant exergy-specific costs of working fluid passing the heat pump turbine
$c_{\mathrm{HE3}} = c_{\mathrm{HE4}}$	constant exergy-specific costs of working fluid passing the heat engine turbine
$c_{\mathrm{me3}} = c_{\mathrm{me4}}$	constant exergy-specific costs along the shaft of the heat engine
boundary conditions	**description**
$c_{\mathrm{HE1}} = 0$	no costs attached to the air entering the heat engine
$c_{\mathrm{HE5}} = 0$	no costs (or revenues) attached to the air leaving the heat engine
$c_{\mathrm{el,in}} = 19.66\,€\,(\mathrm{MWh})^{-1}$	specific costs for electrical energy entering the heat engine (Chapter 5.2.3)

Table 6.14: Integrated amounts of exergy, absolute costs and specific costs per exergy passing through working fluid pipes, electrical leads, and mechanical shafts of the heat pump system during the characteristic operation period. The nomenclature of the states follows Figure 6.2 b).

		HP1	HP2	HP3	HP4	el,in	me1	me2
system 1	E in MWh	61.40	126.61	28.23	3.55	50.40	48.05	21.84
	C in €	11 837	17 869	3985	501	991	1051	4243
	c in €(MWh)$^{-1}$	192.78	141.13	141.13	141.13	19.66	21.87	194.33
system 2	E in MWh	52.97	121.72	32.96	3.58	50.40	48.05	25.86
	C in €	11 988	19 273	5219	566	991	1051	5395
	c in €(MWh)$^{-1}$	226.35	158.34	158.34	158.34	19.66	21.87	208.64

Table 6.15: Integrated amounts of exergy, absolute costs and specific costs per exergy passing through working fluid pipes, electrical leads, and mechanical shafts of the heat engine system during the characteristic operation period. The nomenclature of the states follows Figure 6.2 b).

		HE1	HE2	HE3	HE4	HE5	el,out	me3	me4
system 1	E in MWh	0.00	32.64	128.75	64.03	2.43	21.60	60.49	22.50
	C in €	0	8278	22 372	11 126	0	4525	12 005	4466
	c in €(MWh)$^{-1}$	0.00	253.61	173.76	173.76	0.00	209.51	198.47	198.47
system 2	E in MWh	0.00	27.60	112.89	57.06	3.56	18.60	51.87	19.37
	C in €	0	8243	22 398	11 322	0	4474	11 819	4414
	c in €(MWh)$^{-1}$	0.00	298.65	198.40	198.40	0.00	240.56	227.84	227.84

efficiency of the heat pump motor of system 1 equals the corresponding efficiency of system 2, also the exergy-specific costs of shaft work leaving the motor are equal for both systems. All other exergy-specific costs of system 1 are smaller than the corresponding exergy-specific costs of system 2. This result is caused by all exergetic efficiencies of system 1 being larger than the corresponding exergetic efficiencies of system 2 (Table 6.10). Motor and generator form an exception by having equal exergetic efficiencies in systems 1 and 2.

Similar to the specific costs per exergy, most of the absolute costs propagating through PHES system 2 are larger than the corresponding costs of system 1. Noteworthy exceptions arise at the shaft and the electrical energy output of the heat engine. Smaller amounts of exergy leaving the heat engine of PHES system 2 result in smaller absolute costs compared to system 1.

An overview of the most important variables describing the exergoeconomic performance of the PHES systems and its subsystems is given in Table 6.16. The absolute cost difference across a subsystem is equal to the sum of component costs per operation period for that subsystem. As heat pump and heat engine share the same components, the absolute cost differences across these subsystems are equal. Due to a higher exergy destruction at identical component costs, the heat engine has a slightly worse exergoeconomic performance than the heat pump. The TES system has the best exergoeconomic performance among all subsystems, because it is subject to the smallest exergy destruction (caused by the highest exergetic efficiency) in combination with the smallest component costs per operation period.

Being a good indicator for the exergetic performance, the exergetic efficiencies of PHES system 1 and all of its subsystems are larger than those of system 2. The reverse applies to the relation of exergy

Table 6.16: Summary of variables describing the exergoeconomic performance of the PHES systems and its subsystems.

		E_F	E_P	C_F	C_P	c_F	c_P	$\eta_{II,ex}$	E_D	Z^{OP}
		in MWh		in €		in €(MWh)$^{-1}$		-	in MWh	in €
system 1	HP	50.40	40.53	991	2549	19.66	62.89	0.804	9.87	1558
	TES	40.53	34.50	2549	2967	62.89	86.01	0.851	6.03	419
	HE	34.50	21.60	2967	4525	86.01	209.51	0.626	12.90	1558
	PHES	50.40	21.60	991	4525	19.66	209.51	0.429	28.80	3535
system 2	HP	50.40	39.37	991	2632	19.66	66.85	0.781	11.03	1641
	TES	39.37	31.79	2632	2833	66.85	89.13	0.807	7.58	201
	HE	31.79	18.60	2833	4474	89.13	240.56	0.585	13.19	1641
	PHES	50.40	18.60	991	4474	19.66	240.56	0.369	31.8	3484

Table 6.17: Comparison of the investment costs per output power for different electrical energy storage systems.

	PHES system 1	PHES system 2	ADELE adiabatic CAES	pumped hydro storage
investment costs per output power in € $(kW_{el})^{-1}$	3260	3730	1500 - 2400 [85]	470 - 2170 [18]

destruction between system 1 and 2. Consequently, PHES system 1 has a better exergetic performance than system 2.

The specific costs per exergy product c_P are a good indicator of exergoeconomic system performance; the lower these costs, the better is the performance. Therefore, PHES system 1 and all of its subsystems has also a better exergoeconomic performance than PHES system 2 and its corresponding subsystems. Depending on the component costs per operation period, a favorable exergetic performance is not necessarily tied to a favorable exergoeconomic performance.

The propagation of absolute costs though PHES systems 1 and 2 is visualized in the Sankey diagrams in Figures 6.17 and 6.18, respectively. For a complete overview of the PHES system performance, exergy-specific costs are also listed. The Sankey diagrams exemplify that a multiple of the costs entering and leaving with the electrical energy is attached to the exergy propagating through the PHES system. During operation in cyclic steady state, these costs are not entering or leaving the PHES system.

The PHES systems entail at least 30 % higher investment costs per output power than the ADELE adiabatic CAES system or pumped hydro storage systems (Table 6.17). For the PHES systems, the determined investment costs per output power are solely based on the purchased equipment costs (Chapter 4.4.2). If additional cost sources are considered, the difference to the other storage technologies would further increase.

Considering the economic conditions at the day-ahead market of the year 2016, the PHES systems could not be operated profitably. Based on the characteristic operation scenario (Chapter 5.2.3), the average market price during the heat engine operation amounts to 38.42 € $(MWh)^{-1}$ (Table 5.1). With specific prices for electrical energy supplied by the heat engine of 209.51 € $(MWh)^{-1}$ (PHES system 1) and 240.56 € $(MWh)^{-1}$ (PHES system 2), the attainable market price is exceeded by a factor of 5.45 (PHES system 1) and 6.26 (PHES system 2), respectively.

6.2.4 Sensitivity analysis

The chosen approach for the sensitivity analysis is presented in Chapter 4.5.2. The value for the specific costs for electrical energy entering the PHES system during heat pump operation $c_{el,in}$ and the value for the purchased equipment costs of the PHES system Z^{PEC}_{PHES} are each varied between 0 % and 200 %, while the other value stays constant at its initially determined value of 100 %. In a third case, all of which are depicted in Figure 6.19, the identical variation of both input values at a time is considered. Based on the same percentage variation and valid for both PHES systems, the output is approximately 3.5 times more sensitive to the variation of purchased equipment costs than to the variation of specific costs for electrical energy entering the PHES system.

For an economically competitive operation a PHES system would have to supply electrical energy at specific costs lower than 38.42 € $(MWh)^{-1}$ (Table 5.1). Considering PHES system 1, which has a slightly better exergoeconomic performance than system 2, this margin is far from being reached by moderate variations of the input costs (Figure 6.19). The assumption of receiving the electrical energy input free of charge, which might be realistic taking the prediction of an increasing frequency of negative

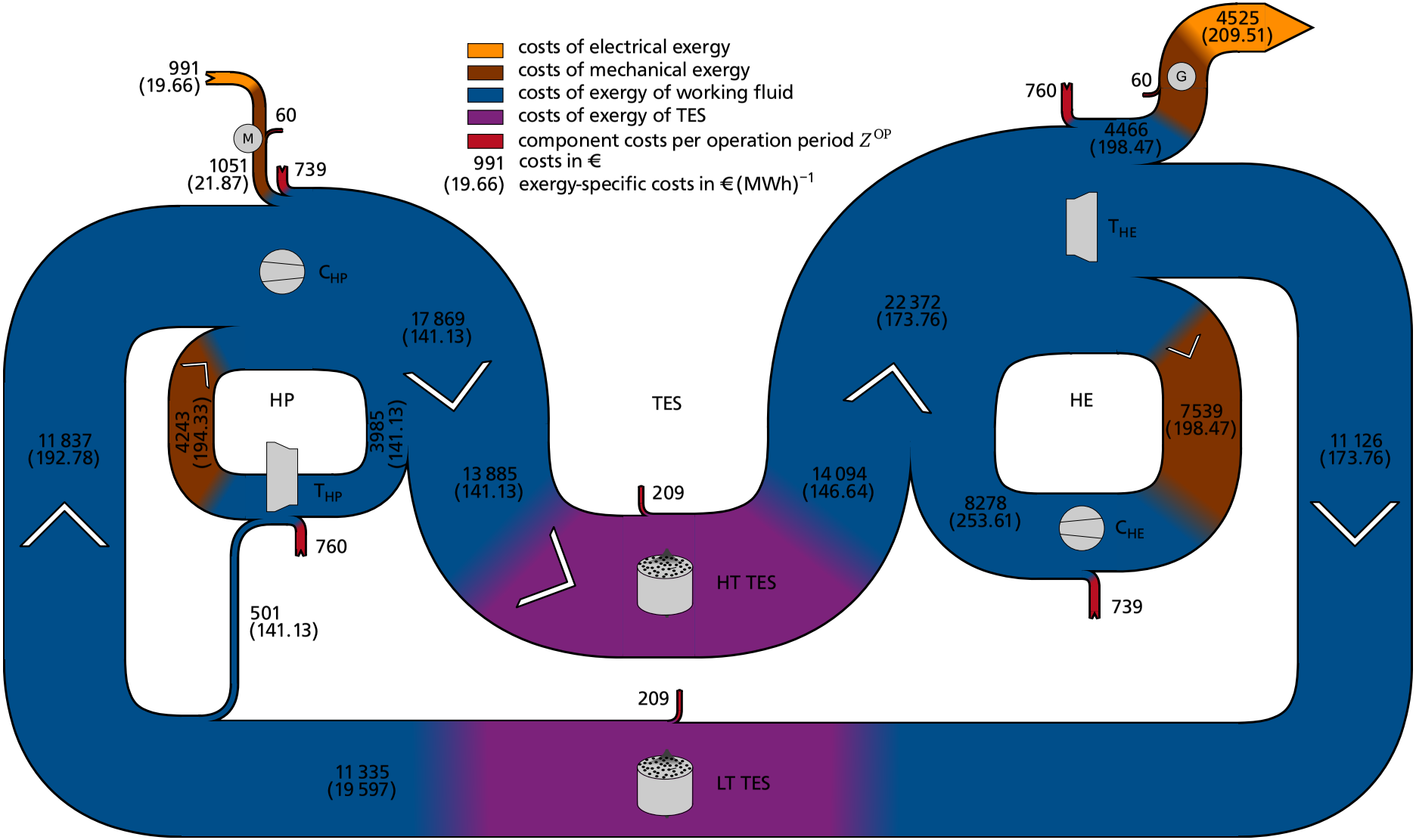

Figure 6.17: Sankey diagram visualizing the propagation of costs through PHES system 1.

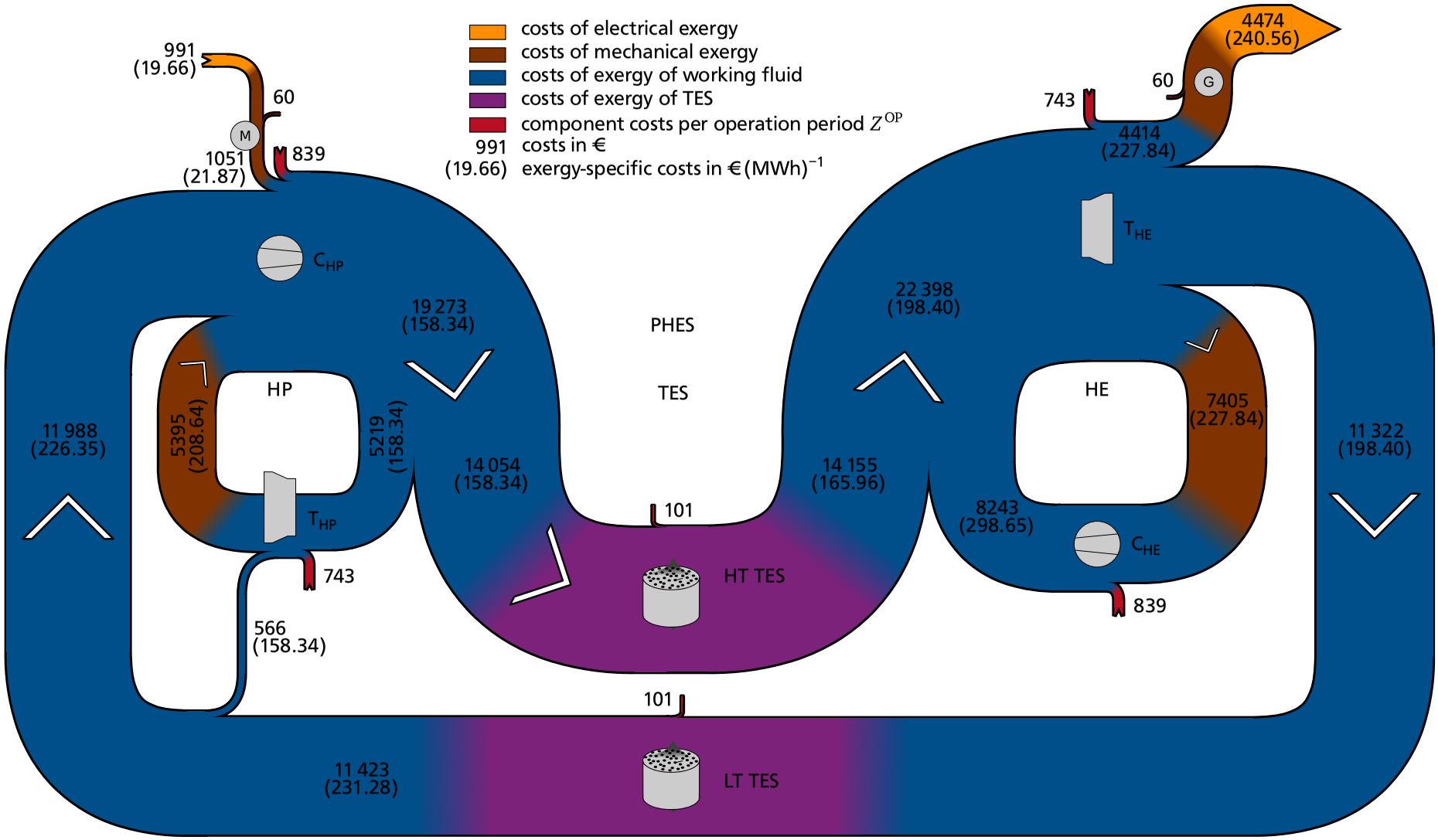

Figure 6.18: Sankey diagram visualizing the propagation of costs through PHES system 2.

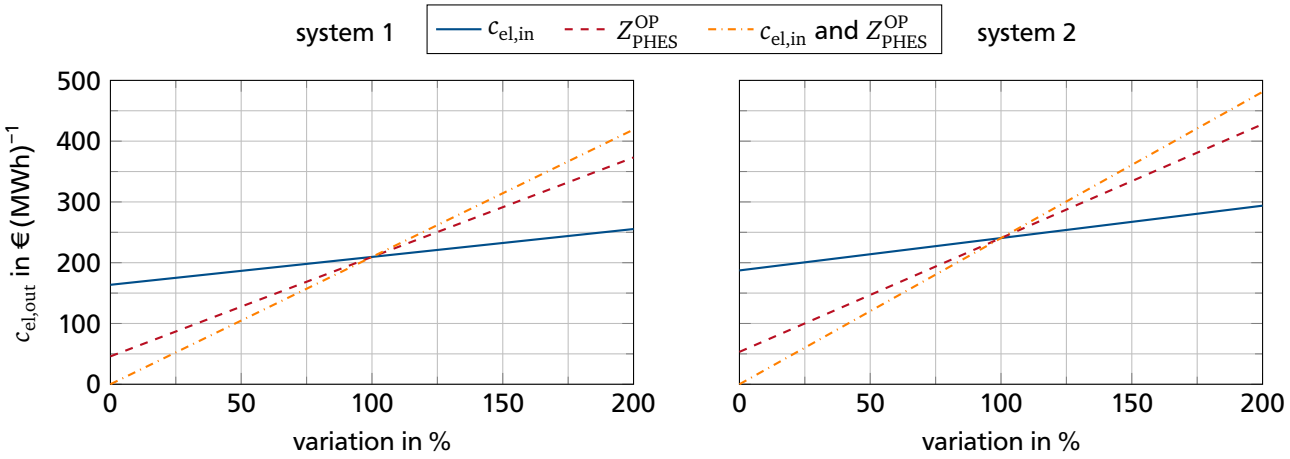

Figure 6.19: Influence of the variation of economic input parameters on the specific costs per exergy released by the PHES system.

energy prices into consideration [37], only slightly lowers the specific costs per electrical energy output to 163.64 €(MWh)$^{-1}$. Reducing the purchased equipment costs by 50 % results in specific costs for the electrical energy output of 127.69 €(MWh)$^{-1}$, which is still more than three times as much as the tolerable market price. Even the entire neglect of the purchased equipment costs, which is hard to justify, only decreases the specific costs for the electrical energy output to 45.87 €(MWh)$^{-1}$, slightly missing the target cost.

6.3 Assessment

Mainly depending on the maximum outlet temperature difference, the analyzed PHES systems reach round-trip efficiencies of 36.9 % and 42.9 %, which is approximately half the efficiency reached by pumped hydro storage systems [18; 102, Chapter 2.4.2] or adiabatic CAES systems [85]. Compared to non-adiabatic CAES systems which are currently in operation, PHES systems have an approximately 10 percentage points lower round-trip efficiency.

Predominantly resulting from high purchased equipment costs, PHES systems have higher power-specific costs than established technologies and can currently not be economically operated at the day-ahead market for Germany and Austria. The latter, however, is at least partly caused by current market conditions, which are unfavorable for the operation of electrical energy storage systems.

Based on the analysis results combined with the independence from geological and topological conditions, PHES systems are assessed as relevant technology to store electrical energy. Research activities on PHES systems should be continued.

7 Analysis of PHES Systems based on Rankine Cycles

In this chapter, design and modeling of PHES systems based on Rankine cycles are presented. First, the selection of the thermodynamic cycles of heat pump and heat engine is illustrated, comprising the selection of a suitable combination of working fluid and phase change material. Second, the design of the TES system is introduced. Afterwards, the process of setting up and challenges of simulating an adequately sized PHES system are described. Finally, a preliminary assessment is presented.

7.1 System design

To achieve high round-trip efficiencies for PHES systems, five design constraints are deduced from the studies published in literature (Chapter 2.2.2). Most of the design constraints are similar to those applied to PHES systems based on Joule cycles.

1. If available, established technology should be employed in order to reduce technological risks.
2. The PHES system layout should be simple, limiting the amount of components to the essentially necessary required for an exergy efficient and cost efficient operation.
3. Heat rejection to the environment should be realized at a small temperature difference in order to minimize the associated exergy loss.
4. In contrast to PHES systems based on Joule cycles, a low temperature TES not necessarily has to be implemented.
5. Also in contrast to PHES systems based on Joule cycles and specifically suggested for PHES systems based on Rankine cycles by Morandin et al. [94] and Mercangöz et al. [89], regenerative heat transfer should be considered. Especially in the absence of a low temperature TES system, regenerative heat transfer can increase the PHES round-trip efficiency.

As additional design constraint, the electrical power consumed and released by the PHES system shall remain constant during operation. Thereby, a beneficial and predictable integration of the PHES system into the electrical grid is enabled.

7.1.1 Selection of thermodynamic cycle

For domestic heating, heat pumps based on Organic Rankine Cycles (ORCs) using organic working fluids are an established technology that is commercially available. However, for heat flows reaching the low megawatt range at supply temperatures exceeding 100 °C, ORC heat pumps are currently not commercially available (Chapter 2.4).

Drawing on commercially available technology, ORC heat engines convert heat at source temperatures between 90 °C and 400 °C into electrical energy at supply powers reaching the low megawatt range [112]. Compared to steam Rankine cycles, ORCs are characterized by a more simple system architecture accompanied by lower system costs (Chapter 2.5).

To account for the technological limitations of heat pump and heat engine, the maximal temperature reached within the PHES system is selected to be in the range of $100\,°C < T_{max} < 150\,°C$. The final value

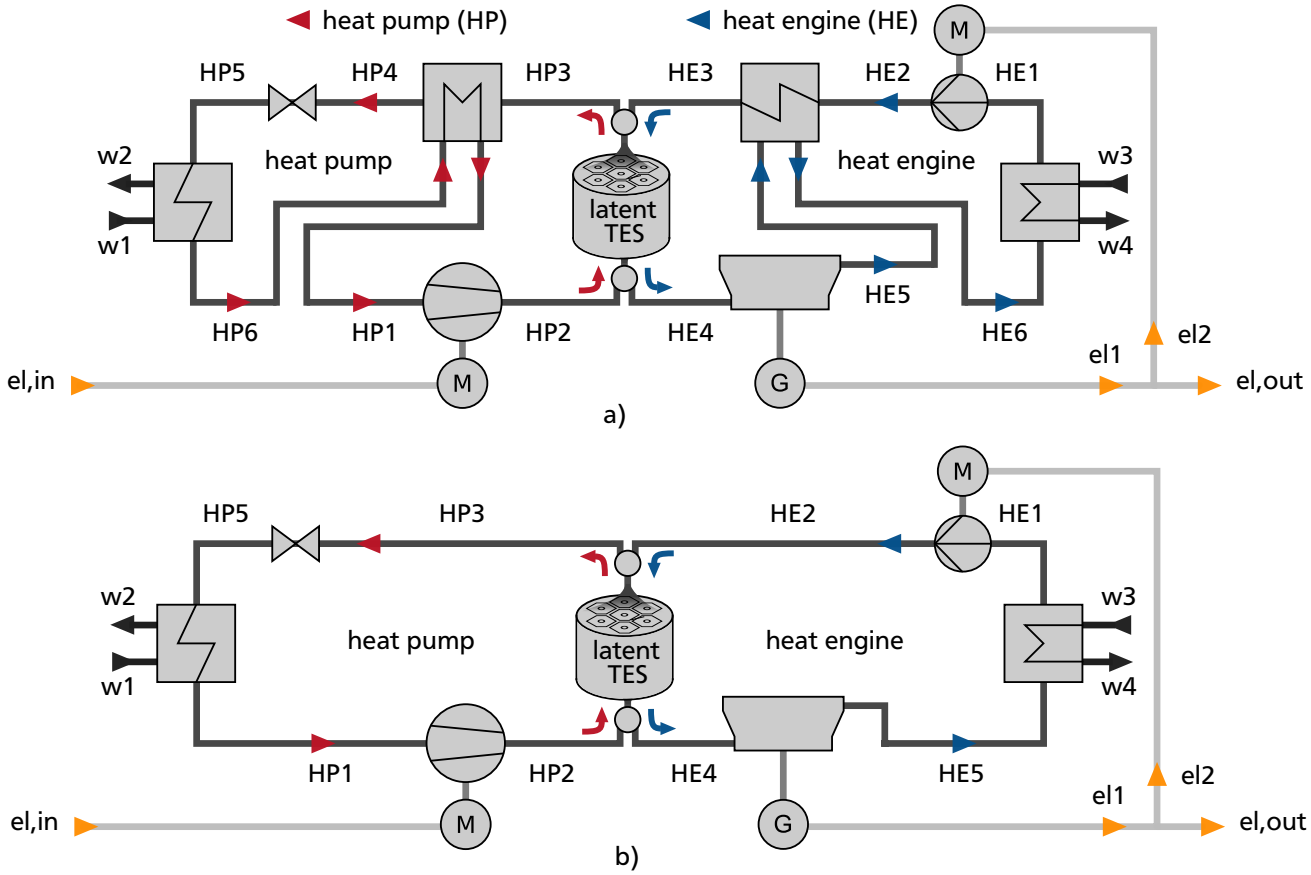

Figure 7.1: Schematics of PHES systems based on OR cycles: a) with internal heat transfer, b) without internal heat transfer.

depends on the organic working fluid and phase change material, the selection of which is described in the following sections. Higher temperatures are not considered, because the required heat pump components are not commercially available. Lower temperatures are not considered, because ORC heat engines can only be operated at significantly reduced efficiencies or cannot be operated at all. Furthermore, maximal temperatures below 100 °C result in large TES systems, because the volume-specific storage capacity to store exergy decreases with storage temperature.

In accordance with the second and fourth design constraint, the low temperature TES system is not implemented and the environment is used as low temperature heat source as well as heat sink. Resulting from the relatively low maximal temperature within the PHES system, the temperature of the working fluid leaving the turbine during heat engine operation is in the order of 40 °C or below. At this temperature the working fluid contains only a small fraction of exergy, the storage of which is exergoeconomically not reasonable. Working fluid turbine outlet temperatures below environmental temperature are not considered, because the required PHES system would violate design constraints one and two. Consequently and for the same reason, a low temperature TES system with temperatures below environmental temperature is not taken into consideration.

The considerations presented in this section result in two cycle layouts for PHES systems based on ORCs, the schematics of which are depicted in Figure 7.1. Cycle layout 1 (Figure 7.1 a)) represents an ORC cycle with internal heat transfer. Regarding the heat pump, the exergy of the working fluid leaving the high temperature TES can be used for superheating the working fluid before entering the compressor. Regarding the heat engine, the exergy of the working fluid leaving the turbine can be used to preheat the working fluid before entering the high temperature TES. Consequently, the incorporation of internal

heat transfer reduces exergy losses. However, the internal heat exchangers increase the complexity of the PHES system and are responsible for additional purchased equipment costs. Moreover, being subject to a varying TES outlet temperature during heat pump operation, the internal heat exchanger causes a varying compressor inlet temperature. This, in turn, might result in higher exergy losses during compression, because the compressor might be operated far from its design point.

Cycle layout 2 (Figure 7.1 b)) represents a basic ORC cycle without internal heat transfer. Consequently, the system is subject to lower purchased equipment costs. Constant compressor inlet temperatures during heat pump operation provide the possibility to operate the compressor close to its design point. However, due to the absence of internal heat transfer, the exergy of the working fluid leaving the high temperature TES system during heat pump operation as well as the turbine during heat engine operation cannot be utilized, which results in higher exergy destruction. Moreover, depending on the ambient conditions and the organic working fluid, an additional component might be necessary in order to superheat the working fluid before entering the compressor. An exergoeconomic analysis of the PHES system during transient operation is necessary to determine which cycle layout yields the better exergoeconomic performance.

Due to a higher stage of development and broader commercial availability, the PHES system is based on subcritical ORCs employing pure working fluids. Trans- or supercritical ORCs and the employment of mixtures of different working fluids are not considered in this work. Therefore, the organic working fluid experiences an (almost) isothermal, liquid-vapor phase change during heat transfer within the high temperature TES system. As a consequence, a PHES system based on ORCs should be combined with a latent heat TES system. Having selected an appropriate phase change material, the latent heat TES system is subject to an isothermal, liquid-solid phase change (Chapter 2.6.2) during heat transfer. Consequently, exergy losses during heat transfer can be minimized due to small temperature differences. Out of the large variety of different organic working fluids and various phase change materials, a suitable combination resulting in high PHES round-trip efficiencies has to be identified.

Selection of working fluid

For a simple system design, heat pump and heat engine are based on the same organic working fluid. Various criteria for ORC working fluid selection are numerously summarized in literature. The criteria are granted different priorities, depending on the objective of the ORC operation, primarily distinguishing between maximizing efficiency, maximizing output power or minimizing equipment costs. Based on the criteria given in [112; 137; 151] and oriented towards high round-trip efficiency and low purchased equipment costs of the PHES system, the following working fluid selection criteria are deduced.

1. High enthalpy of vaporization Δh_v: Provided that a suitable phase change material can be employed, PHES round-trip efficiency increases with increasing latent heat of vaporization, because larger amounts of heat can be transfered at small temperature differences between working fluid and TES.
2. Dry fluids instead of wet fluids: The vapor saturation curve in the T,s-diagram is characterized by a positive slope for dry fluids (Figure 7.2 a)) and a negative slope for wet fluids (Figure 7.2 b)). For both types of fluids, Figure 7.2 also depicts their compression (HP1 - HP2) and heat transfer to the TES system (HP2 - HP3) during heat pump operation. For dry fluids, the efficient and significant transfer of latent heat occurs at a higher condensation temperature T_{cond}, closer to the maximal system temperature T_{max}, which increases the PHES round-trip efficiency. If dry fluids require superheating, this has not to be realized at the high temperature level before the working fluid enters the turbine of the heat engine, but can be realized at the low temperature level before

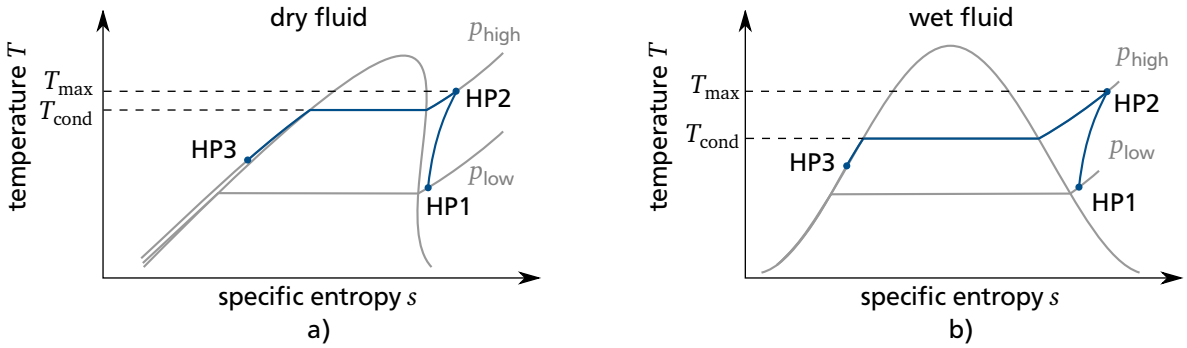

Figure 7.2: Comparison of compression (HP1 - HP2) and heat transfer to the latent heat TES (HP2 - HP3) in T,s-diagrams for dry working fluids (a)) and wet working fluids (b)).

the working fluid enters the compressor of the heat pump. Consequently the superheating of dry working fluids requires less exergy.

3. Critical temperature $T_{crit} > 120\,°C$: Based on a subcritical operation of the PHES system, critical temperatures lower than 120 °C impose a too low upper temperature limit on the PHES system.
4. Lowest system pressure higher than ambient pressure: System pressures higher than ambient pressure are desirable in order to prevent air or water infiltration.
5. Largest system pressure lower than 30 bar: For system pressures lower than 30 bar all components of the heat engine are commercially available, which reduces purchased equipment costs.
6. High density of liquid and vapor phase: Higher densities result in lower volume flow rates which in turn result in smaller components and smaller purchased equipment costs.
7. Melting temperature lower than lowest system temperature: In order to ensure operability of the PHES system, the temperature of the working fluid should not fall below its melting temperature.
8. Low environmental impact: Having an ozone depletion potential larger than 1, working fluids phased out by the Montreal Protocol [123] are neglected. Working fluids with a low global warming potential should preferably be selected.
9. Good safety characteristics with respect to toxicity and flammability.
10. Low costs and good availability.

All working fluids considered in relevant studies on ORCs [112; 137; 138; 151] are examined as potential working fluids for PHES systems. The thermodynamic properties necessary to evaluate these fluids with respect to the selection criteria 1 to 7 are summarized in Appendix A.3. In accordance with selection criterion 1, the working fluids are listed in descending order with respect to their mass-specific enthalpy of vaporization at the temperatures $T = 120\,°C$ and $T = 100\,°C$.

Based on selection criteria 2 and 3, only dry working fluids having a critical temperature $T_{crit} > 120\,°C$ are considered further. Taking selection criterion 4 into consideration, the normal boiling temperature T_{NB} is examined. Being defined as the vaporization temperature at ambient pressure p_{amb}, T_{NB} specifies the lowest acceptable temperature of the working fluid within the PHES system. Therefore, only working fluids having a normal boiling temperature lower than ambient temperature ($T_{NB} \leq T_{min} < T_{amb} = 10\,°C$) are suitable for the PHES system.

Evaluating the thermodynamic properties listed in Appendix A.3, all working fluids that fulfill selection criteria 2 to 4 are identified. Although to a varying degree, these working fluids also fulfill selection criteria 5 to 7. Properties and classifications suitable to evaluate these working fluids with respect to selection criteria 8 to 10 are presented in Table 7.1.

The environmental impact (criterion 8) is evaluated using the ozone depletion potential (ODP) and the global warming potential ($GWP_{100\,a}$), based on a time horizon of 100 years. Having an ozone depletion

Table 7.1: Properties and classifications of working fluids listed in Appendix A.3 that fulfill selection criteria 2 to 7.

working fluid	$\Delta h_{v,120\,°C}$ in kJ (kg)$^{-1}$ [80]	ODP [123]	$GWP_{100\,a}$ [129]	ASHRAE safety group [6]	costs in \$ t^{-1} [92]
butane (R600)	213.4	0	4	A3	750
isobutane (R600a)	150.2	0	3	A3	1290
R236ea	77.0	0	1370	A1	3 028 000
R114	69.9	1	10 000	A1	2 199 000
R236fa	43.6	0	9810	A1	530 000

potential of 1, the working fluid R114 is phased out by the Montreal Protocol [123] and therefore cannot be used in PHES systems. Based on the global warming potential, butane and isobutane have a low environmental impact. Taking into consideration that only a few fluids are rated with a $GWP_{100\,a}$ exceeding 15 000 [129], the environmental impact of R236ea and R236fa is rather high.

Evaluating toxicity and flammability (criterion 9), the classification into ASHRAE safety groups yields a reverse fluid ranking. Butane and isobutane are classified as safety group A3 (lower toxicity, higher flammability), while R236ea and R236fa are classified as safety group A1 (lower toxicity, no flame propagation). A market inquiry reveals that the costs (criterion 10) for butane and isobutane are at least two orders of magnitude smaller than the costs for R236ea and R236fa.

Comparing all characteristics listed in Table 7.1, butane is chosen as working fluid for PHES systems based on Rankine cycles. Butane combines the highest mass-specific enthalpy of vaporization with the lowest fluid costs and is characterized by a low environmental impact. Its ASHRAE safety group classification is acceptable, because it is equal to the classification of Pentane [6], which is commonly employed in commercial ORC installations [112].

Selection of phase change material

Criteria for the selection of suitable PCMs are summarized in Chapter 2.6.2. Most important, the phase change temperature of the PCM has to be close to the phase change temperature of the organic working fluid during evaporation and condensation inside the high temperature TES. As the maximal temperature of the working fluid was selected to be in the range of $100\,°C < T_{max} < 150\,°C$, the phase change temperature of the PCM has to lie within that range. Out of 33 PCMs that have been investigated for and employed in different TES systems [3], only the salt hydrate magnesium chloride hexahydrate ($MgCl_2{\cdot}6H_2O$) and the sugar alcohol erythritol ($C_4H_{10}O_4$) fulfill this requirement. Relevant properties of both PCMs are summarized in Table 7.2. Except for $c_{p,s}$, λ_l, and Δh_f, both PCMs have similar properties. Advantageous for a compact TES system, the mass-specific enthalpy of fusion of erythritol is twice as high as that of magnesium chloride hexahydrate. However, the latter can be acquired for less than 10 %

Table 7.2: Properties of PCMs that can be employed in a PHES system using the working fluid butane.

PCM	T_{PC} in °C	Δh_f in kJ(kg)$^{-1}$	$c_{p,s}$ in kJ(kg K)$^{-1}$	$c_{p,l}$	λ_s in W(m K)$^{-1}$	λ_l	ρ_s in kg m^{-3}	ρ_l	costs in \$ t^{-1} [92]
$MgCl_2{\cdot}6H_2O$ [3]	116.7	168.6	2.25	2.61	0.704	0.570	1570	1450	290
erythritol [2]	117.7	339.8	1.38	2.76	0.733	0.326	1480	1300	4520

of the price for erythritol. As both materials are approved for use as food additives (magnesium chloride hexahydrate: E 511, erythritol: E 968 [149]), they are harmless for humans and the environment.

Like most salt hydrates, magnesium chloride hexahydrate is affected by supercooling and phase segregation during thermal cycling [81; 107]. After 500 charging and discharging cycles, the phase change temperature and the enthalpy of fusion are reduced significantly [81], which makes an application of magnesium chloride hexahydrate within a PHES system impossible. Erythritol shows higher cyclic stability. After 1000 charging and discharging cycles, its phase change temperature and enthalpy of fusion are reduced by approximately 10 °C and 40 kJ $(\mathrm{kg})^{-1}$, respectively [127]. Based on 1000 cycles, the thermal stability of erythritol is acceptable. Studies evaluating the thermal stability for a larger number of cycles are not available. Consequently, erythritol is selected as PCM for the PHES system.

7.1.2 Selection of thermal energy storage system

The layout of the latent heat thermal energy storage system is based on the DLR latent heat TES module [71; 72; 86] introduced in Chapter 4.3.3 (Figure 4.12). A cylindrical container filled with PCM is traversed by heat exchanger pipes equipped with aluminum fins. The detailed design of the TES system is specified by

- the length and the diameter of the storage module,
- the amount and the spacing of the heat exchanger pipes, and
- the spacing of the fins.

The design of the TES system and the operation of heat pump and heat engine influence each other. Consequently, the detailed TES design has to be determined based on transient simulations of the entire PHES system.

For an initial setup, the required mass of the PCM is approximated as follows. In accordance with the characteristic operation scenario (Chapter 5.2.3), the heat engine shall produce an output power of $P_{\mathrm{el,out}} = 4.7\,\mathrm{MW}$ for $\Delta\tau = 4\,\mathrm{h}$ at an estimated energetic efficiency of $\eta_{\mathrm{en,HE}} = 0.15$. Assuming that the required thermal energy is provided by the PCM as latent heat only, the mass of the PCM can be determined to

$$M_{\mathrm{PCM}} = \frac{Q_{\mathrm{HE_in}}}{\Delta h_{\mathrm{f}}} = \frac{P_{\mathrm{el,out}}\Delta\tau}{\Delta h_{\mathrm{f}}\eta_{\mathrm{en,HE}}} = 1330\,\mathrm{t}, \tag{7.1}$$

which corresponds to a volume of $1000\,\mathrm{m}^3$ erythritol. The corresponding cylindrical storage container could be designed with a diameter of 7 m and a length of 28 m. Traversed by pipes having the same spacing as those in the DLR module, 5000 pipes have to be integrated. The optimal design of the TES system regarding pressure drop, transfered heat and storage costs can be determined by an exergoeconomic analysis of the transient PHES system operation.

7.2 System simulation

The PHES systems depicted in Figure 7.1 based on the working fluid butane have been modeled in EBSILON®*Professional*. The developed model of the latent heat TES employing erythritol as PCM has been integrated. In order to simulate the PHES system operation in accordance with the characteristic operation scenario, the TES system has to be sized as described in the previous section, which results in a relatively large TES system.

Simulating a physically large TES system within the model of the entire PHES system proved challenging. Simulation parameters need to be set carefully in order to achieve convergence at acceptable

simulation run times. Moreover, identifying the final design of the TES system that allows the operation of the PHES system in accordance with the characteristic operation scenario is elaborate. For each prospective TES design in the iterative design process, the entire PHES system has to be simulated until the cyclic steady state is reached and can be evaluated. Against all efforts, the identification of a TES design that allows the operation of the PHES system in accordance with the characteristic operation scenario could not be completed in the available time frame of this work. As a consequence, an exergoeconomic analysis of PHES systems based on Rankine cycles combined with latent heat TES systems was not performed and the focus was set to the study of PHES systems based on Joule cycles.

However, within the design calculations several PHES systems were successfully simulated and proved the general applicability of the developed models. For a preliminary potential estimation of the PHES systems introduced in this chapter, the performance of a sample system with internal heat transfer (Figure 7.1 a)) is presented. Based on an averaged heat pump input power of 11.5 MW_{el}, a TES system containing 1585 t erythritol and 6000 heat exchanger pipes allowed for a heat pump and heat engine operation of 4.0 h, each, resulting in a round-trip efficiency of $\eta_{PHES} = 38\,\%$. Because crucial design parameters might change, this efficiency identifies the order of magnitude to expect. Upward or downward deviations are possible.

7.3 Assessment

A final assessment of PHES systems based on Rankine cycles is not yet possible. However, preliminary calculations yield round-trip efficiencies that are similar to those of PHES systems based on Joule cycles. The system design described in this chapter combined with the developed models are a good foundation to finish the parametrization and simulate as well as analyze the Rankine cycle based PHES systems.

8 Summary and Outlook

In this work, numerical models that enable a transient simulation of PHES systems were created using the process simulation software EBSILON®*Professional*. For that purpose, models of a packed bed sensible heat TES system as well as a latent heat TES system were developed and validated. For the simulation and analysis of PHES systems, a characteristic operation scenario focusing on the day-ahead-market was deduced from the European market for electrical energy. Employing commercially available and state-of-the-art technology, PHES systems based on Joule and Rankine cycles were designed, simulated, and analyzed. Consequently, the objectives of this work defined in Chapter 3 were reached. A summary of the results and suggestions for the continuation of this work are presented in the following.

8.1 PHES systems based on Joule cycles

A PHES system based on a Joule cycle combined with a high and a low temperature TES was designed. Heat pump and heat engine share the components compressor, turbine, and motor/generator. The TES systems contain packed beds of basalt chips without quartz content that exchange sensible heat with the working fluid air. The temperature levels of both TESs are above ambient temperature. Due to a lower exergetic and exergoeconomic performance, the implementation of Joule/resistive heating instead of a Joule heat pump is not suggested.

Resulting from the high temperature of the working fluid leaving the turbine of the heat engine, the working fluid contains a large amount of exergy. For a reasonable round-trip efficiency, this exergy should not be rejected to the environment and therefore is stored in a low temperature TES. Employing regenerative heat transfer instead of a low temperature TES is not beneficial. On the one hand, regenerative heat transfer cannot be employed within the heat pump. On the other hand, the heat transfer within an air-air heat exchanger is not as efficient as the heat transfer between air and the packed bed TES material. In the latter case, heat source and heat sink are in direct contact.

Based on several design and process parameters, such as maximum temperature in the heat pump, efficiencies of the turbomachinery, and pressure drop in the TES systems, the maximal pressure in the heat engine resulting in optimal PHES efficiency was determined. System simulations demonstrate that the selection of the maximum outlet temperature difference, the difference in working fluid temperature leaving the high temperature TES between the beginning and the end of the heat pump/heat engine operation, is an influential design parameter. It influences both, the size of the TES systems required to deliver a specific amount of thermal energy and the efficiency of the PHES system. With increasing maximum outlet temperature difference, size and efficiency of the TES system decrease.

For a stable system operation, the inlet temperature of the working fluid entering the high temperature TES system needs to stay constant during heat pump and heat engine operation. Constant inlet temperatures cause the development of a favorable temperature distribution in the high temperature TES system that leads to an operation in cyclic steady state. However, unfavorable temperature distributions can be removed by operating the PHES system with constant inlet temperatures to the high temperature TES.

The operation of two PHES systems with different maximum outlet temperature differences, and hence different sizes of the TES systems, was simulated in accordance with the characteristic operation scenario. The systems reached round-trip efficiencies of 42.9 % and 36.9 % which is approximately half the

efficiency reached by pumped hydro storage systems. The exergoeconomic performance of both PHES systems is rather weak, supplying electrical energy at costs that exceed acceptable market prices by more than a factor of five. Identified by the sensitivity analysis, uncertainties of the purchased equipment costs have a distinct influence on the specific costs for electrical energy leaving the PHES system. Nevertheless, even the complete neglect of purchased equipment costs would not result in an economically profitable system operation.

The weak economic performance is at least partly caused by current conditions at the day-ahead market for Germany and Austria which are unfavorable for the operation of electrical energy storage systems. Considering the analysis results combined with the independence from geological and topological conditions, PHES systems are assessed as relevant technology to store electrical energy. Therefore, research activities on PHES systems should be continued.

8.2 PHES systems based on Rankine cycles

Two PHES systems based on subcritical organic Rankine cycles were designed, one system with, the other without internal heat transfer. The high pressure sections of the thermodynamic cycles are combined with a latent heat TES system to exchange high temperature heat with the working fluid. Having temperatures close to ambient temperature, the exergy of the working fluid within the low pressure sections of the thermodynamic cycles is negligible. Consequently, the employment of a low temperature TES is not reasonable. However, to prevent the condensation of the working fluid within the turbomachinery, superheating might be required. By employing regenerative heat transfer, superheating can be achieved without consuming additional electrical energy.

Evaluating more than 35 potential working fluids with respect to working fluid selection criteria, butane was selected for the employment in PHES systems with a maximal temperature in the range of $100\,^{\circ}\mathrm{C} < T_{\max} < 150\,^{\circ}\mathrm{C}$. Increasing the round trip efficiency, PHES systems should be based on isentropic or dry working fluids. Adapted to the range of the maximal temperature, erythritol was identified as suitable PCM out of 33 materials investigated for and employed in different TES systems. With larger dimensions, the layout of the cylindrical TES system traversed by heat exchanger pipes is based on a test module developed by the DLR.

The entire PHES system was modeled, including the model of the latent heat TES also developed in the course of this work. The final design of the TES system that allows the operation of the PHES system in accordance with the characteristic operation scenario is elaborate and requires the simulation of several PHES systems, each until the cyclic steady state is reached. The required simulations could not be completed in the available time frame of this work. Consequently, an exergoeconomic analysis of PHES systems based on Rankine cycles combined with latent heat TES systems is still pending. However, demonstrating the general applicability of the developed models, preliminary calculations indicate expected round-trip efficiencies in the order of 38 %.

8.3 Outlook

Research activities should be continued by identifying the design of the latent heat TES system that allows the operation of the Rankine cycle based PHES systems in accordance with the characteristic operation scenario. The models developed in this work provide a sound scientific foundation for the required simulations. Subsequently, a complete exergoeconomic analysis of the Rankine cycle based PHES systems should be performed. Further, it would be of interest to compare the exergoeconomic analysis results

of the Joule and Rankine cycle based PHES systems. The system with the highest exergoeconomic performance should be identified and could be designed in an even higher level of detail.

To increase the validity of the simulation results, two measures are suggested which, however, might be difficult to realize. First, instead of empirical correlations, operational data of real TES systems should be employed to determine influential model parameters of the TES systems, as convective heat transfer coefficient, thermal conductivity and pressure drop. Second, the determination of purchased equipment costs should be based on actual vendor information instead of cost functions.

Last but not least, the analysis method could be enhanced by conducting a complete regression based sensitivity analysis. Thereby, the simplified approach realized in this work could be replaced and a larger number of input factors could be considered.

Bibliography

[1] AG Energiebilanzen. Share of renewable energy sources in gross electrical energy production in Germany from 1990 to 2015. Statista - Statistik Portal, 2015.

[2] F. Agyenim, P. Eames, and M. Smyth. Experimental study on the melting and solidification behaviour of a medium temperature phase change storage material (Erythritol) system augmented with fins to power a LiBr/H2o absorption cooling system. *Renewable Energy*, 36(1):108–117, Jan. 2011.

[3] F. Agyenim, N. Hewitt, P. Eames, and M. Smyth. A review of materials, heat transfer and phase change problem formulation for latent heat thermal energy storage systems (LHTESS). *Renewable and Sustainable Energy Reviews*, 14(2):615–628, Feb. 2010.

[4] O. Akpinar. *Exergoökonomische Analyse von Strom-Wärme-Strom (SWS) Speichersystemen*. Master Thesis, TU Darmstadt, Mar. 2015.

[5] V. Alexiades and A. D. Solomon. *Mathematical Modeling of Melting and Freezing Processes*. Hemisphere Publishing Corporation, Washington, 1993.

[6] American Society of Heating, Refrigerating and Air-Conditioning Engineers. Designation and Safety Classification of Refrigerants. ASHRAE STANDARD, Atlanta, June 2008.

[7] H. D. Baehr and S. Kabelac. *Thermodynamik Grundlagen und technische Anwendungen*. Springer-Lehrbuch. Springer Vieweg, Berlin, Heidelberg, 15 edition, 2012.

[8] O. Balli, H. Aras, and A. Hepbasli. Exergoeconomic analysis of a combined heat and power (CHP) system. *International Journal of Energy Research*, 32(4):273–289, 2008.

[9] T. Bauer, D. Laing, and R. Tamme. Characterization of Sodium Nitrate as Phase Change Material. *International Journal of Thermophysics*, 33(1):91–104, 2012.

[10] Bauzentrum Beckmann. Costs of basalt chips. Website, http://www.beckmann-bauzentrum.de/naturstein-keramik/zierkiessplittgeroell/zier-uwegesplitt.html, Mar. 2017.

[11] A. Bejan, G. Tsatsaronis, and M. Moran. *Thermal Design and Optimization*. Wiley-Interscience, New York, 1996.

[12] J. F. Belmonte, P. Eguía, A. E. Molina, J. A. Almendros-Ibáñez, and R. Salgado. A simplified method for modeling the thermal performance of storage tanks containing PCMs. *Applied Thermal Engineering*, 2016.

[13] J. Bonin. *Handbuch Wärmepumpen - Planung und Projektierung*. Beuth Verlag, Berlin, 2 edition, 2012.

[14] Bundesministerium für Wirtschaft und Energie (BMWi). Ein Strommarkt für die Energiewende. Report, Berlin, Oct. 2014.

[15] Chemical Engineering Plant Cost Index. Economic Indicators. *Chemical Engineering*, (3):92, 2017.

[16] H. Chen, D. Y. Goswami, and E. K. Stefanakos. A review of thermodynamic cycles and working fluids for the conversion of low-grade heat. *Renewable and Sustainable Energy Reviews*, 14(9):3059–3067, Dec. 2010.

[17] J. P. Coutier and E. A. Farber. Two applications of a numerical approach of heat transfer process within rock beds. *Solar Energy*, 29(6):451–462, Jan. 1982.

[18] J. P. Deane, B. P. Ó Gallachóir, and E. J. McKeogh. Techno-economic review of existing and new pumped hydro energy storage plant. *Renewable and Sustainable Energy Reviews*, 14(4):1293–1302, May 2010.

[19] T. Desrues, J. Ruer, P. Marty, and J. F. Fourmigué. A thermal energy storage process for large scale electric applications. *Applied Thermal Engineering*, 30(5):425–432, Apr. 2010.

[20] Deutscher Bundestag. Gesetz zur Einführung von Ausschreibungen für Strom aus erneuerbaren Energien und zu weiteren Änderungen des Rechts der erneuerbaren Energien, EEG, July 2016.

[21] Deutscher Wetterdienst. Temperatur im Jahr 2015 nach Bundesländern. Statista - Statistik Portal, 2016.

[22] Deutscher Wetterdienst. Temperatur im Jahr 2016 nach Bundesländern. Statista - Statistik Portal, 2017.

[23] A. Dietrich, F. Dammel, and P. Stephan. Exergoeconomic Analysis of a Pumped Heat Electricity Storage System with Concrete Thermal Energy Storage. *International Journal of Thermodynamics*, 19(1):43–51, Mar. 2016.

[24] Y. Dutil, D. R. Rousse, N. B. Salah, S. Lassue, and L. Zalewski. A review on phase-change materials: Mathematical modeling and simulations. *Renewable and Sustainable Energy Reviews*, 15(1):112–130, Jan. 2011.

[25] S. Ergun. Fluid flow through packed columns. *Chemical Engineering Progress*, 48(2):89–94, 1952.

[26] European Energy Exchange. EEX. Website, https://www.eex.com, Jan. 2017.

[27] European Power Exchange. EPEX SPOT SE. Website, https://www.epexspot.com, Jan. 2017.

[28] European Power Exchange. EPEX SPOT SE: Day-Ahead Auction. Website, https://www.epexspot.com/en/market-data/dayaheadauction, Jan. 2017.

[29] N. Fisch, M. Bodmann, L. Kühl, C. Saße, and H. Schnürer. *Wärmespeicher*. BINE - Informationspaket. TÜV-Verlag, Köln, 4 edition, 2005.

[30] C. A. Frangopoulos. Comparison of Thermoeconomic and Thermodynamic Optimal Designs of a Combined-Cycle Plant. In *Proceedings of the International Conference on the Analysis of Thermal and Energy Systems*, 1991.

[31] C. Fraunholz. *Exergoökonomische Analyse von Strom-Wärme-Strom Speichersystemen angelehnt an adiabate Druckluftspeicher*. Master Thesis, TU Darmstadt, Apr. 2016.

[32] H. U. Frutschi. *Closed-cycle gas turbines: operating experience and future potential*. ASME Press, New York, 2005.

[33] A. Gil, M. Medrano, I. Martorell, A. Lázaro, P. Dolado, B. Zalba, and L. F. Cabeza. State of the art on high temperature thermal energy storage for power generation. Part 1 - Concepts, materials and modellization. *Renewable and Sustainable Energy Reviews*, 14(1):31–55, Jan. 2010.

[34] V. Gnielinski. Fluid-Particle Heat Transfer in Flow Through Packed Beds of Solids (G9). In VDI e. V., editor, *VDI Heat Atlas*, pages 743–744. Springer-Verlag, Berlin, Heidelberg, 2 edition, 2010.

[35] V. Gnielinski. Heat Transfer in Pipe Flow (G1). In VDI e. V., editor, *VDI Heat Atlas*, pages 691–700. Springer-Verlag, Berlin, Heidelberg, 2 edition, 2010.

[36] V. Gorris and A. Jacob. BWP-Branchenstudie 2013 - Daten zum Wärmepumpenmarkt bis 2012 und Prognosen bis 2030. Report, Bundesverband Wärmepumpe (BWP) e.V., Berlin, 2013.

[37] P. Götz, J. Henkel, T. Lenck, and K. Lenz. Negative Strompreise: Ursachen und Wirkungen. Report, Agora Energiewende, Berlin, June 2014.

[38] K. M. Guthrie. Data and Techniques for Preliminary Capital Cost Estimating. *Chemical Engineering*, pages 114–142, 1969.

[39] K. M. Guthrie. *Process plant estimating, evaluation, and control*. Craftsman Book Co. of America, Los Angeles, 1974.

[40] M. Hänchen, S. Brückner, and A. Steinfeld. High-temperature thermal storage using a packed bed of rocks – Heat transfer analysis and experimental validation. *Applied Thermal Engineering*, 31(10):1798–1806, July 2011.

[41] N. Hartmann, O. Vöhringer, C. Kruck, and L. Eltrop. Simulation and analysis of different adiabatic Compressed Air Energy Storage plant configurations. *Applied Energy*, 93:541–548, May 2012.

[42] A. Hauer, S. Hiebler, and M. Reuß. *Wärmespeicher*. BINE-Fachbuch. Fraunhofer IRB Verlag, Stuttgart, 5 edition, 2012.

[43] F. Heberle and D. Brüggemann. Thermodynamische Grundlagen des ORC und aktuelle Forschungsaktivitäten. In *Jahrestagung des ORC-Fachverbandes e.V.*, Bayreuth, 2012.

[44] M. Hecht, O. Polach, and U. Kleemann. Schienenfahrzeuge. In K.-H. Grote and J. Feldhusen, editors, *Dubbel*, pages 1181–1212. Springer-Verlag, Berlin, Heidelberg, 24 edition, 2014.

[45] R. Heidelck, H. Kruse, and H.-J. Laue. Wärmepumpen in Gewerbe und Industrie - Ein Überblick. Report, Informationszentrum Wärmepumpen und Kältetechnik e.V., Hannover, 2000.

[46] L. Heller and P. Gauché. Modeling of the rock bed thermal energy storage system of a combined cycle solar thermal power plant in South Africa. *Solar Energy*, 93:345–356, July 2013.

[47] J. Hemrle, L. Kaufmann, and M. Mercangoez. Thermoelectric energy storage system having two thermal baths and method for storing thermoelectric energy. European Patent EP2241737 A1, ABB Research Ltd., Oct. 2010.

[48] J. Hemrle, L. Kaufmann, and M. Mercangoez. Thermoelectric energy storage system with an intermediate storage tank and method for storing thermoelectric energy. European Patent EP2275649 A1, ABB Research Ltd., Jan. 2011.

[49] J. Hemrle, L. Kaufmann, and M. Mercangoez. Thermoelectric energy storage system with an intermediate storage tank and method for storing thermoelectric energy. European Patent EP2275649 B1, ABB Research Ltd., Sept. 2012.

[50] J. Hemrle, L. Kaufmann, and M. Mercangoez. Energy storage system with an intermediate storage tank and method for storing thermoelectric energy. European Patent EP2554804 A2, ABB Research Ltd., Feb. 2013.

[51] J. Hemrle, L. Kaufmann, and M. Mercangoez. Energy storage system with an intermediate storage tank and method for storing thermoelectric energy. European Patent EP2554804 A3, ABB Research Ltd., Mar. 2015.

[52] J. Hemrle, L. Kaufmann, and M. Mercangoez. Thermoelectric energy storage system having two thermal baths and method for storing thermoelectric energy. European Patent EP2241737 B1, ABB Research Ltd., June 2015.

[53] J. Hemrle, L. Kaufmann, M. Mercangoez, and C. Ohler. Thermoelectric energy storage system and method for storing thermoelectric energy. European Patent EP2390473 A1, ABB Research Ltd., Nov. 2011.

[54] D. Hering. *Numerische Simulation eines Latentwärmespeichers für ein Strom-Wärme-Strom Speichersystem*. Master Thesis, TU Darmstadt, Apr. 2015.

[55] J. S. Howes. Concept and Development of a Pumped Heat Electricity Storage Device. *Proceedings of the IEEE*, 100(2):493–503, 2012.

[56] J. S. Howes and J. Macnaghten. Apparatus for use as a heat pump. European Patent EP1872069 B1, Isentropic Ltd., Nov. 2010.

[57] J. S. Howes and J. Macnaghten. Energy storage apparatus and method for storing energy. European Patent EP2220343b1, Isentropic Ltd., June 2013.

[58] IKZ-FACHPLANER. Wärmepumpen für Industrie und Gewerbe - Marktübersicht sowie mögliche Anwendungsgebiete und Potenziale von Groß-Wärmepumpen in Deutschland. *IKZ-FACHPLANER*, (4):7–12, 2009.

[59] International Monetary Fund. Annually averaged US-Dollar - Euro exchange rates from 1999 to 2016. Report, Mar. 2017.

[60] K. A. R. Ismail and R. Stuginsky Jr. A parametric study on possible fixed bed models for pcm and sensible heat storage. *Applied Thermal Engineering*, 19(7):757–788, July 1999.

[61] R. Jakobs, D. Cibis, and H.-J. Laue. Status And Outlook: Industrial Heat Pumps. In *International Refrigeration and Air Conditioning Conference*, Purdue, 2010.

[62] S. Kabelac, F. Flohr, and C. Stadtländer. Entwicklung eines Arbeitsfluids für Hochtemperaturwärmepumpen. *KI. Luft- und Kältetechnik*, 42(6):234–240, 2006.

[63] G. Kasparek. Insulations Materials (D6.5). In VDI e. V., editor, *VDI Heat Atlas*, pages 591–594. Springer-Verlag, Berlin, Heidelberg, 2 edition, 2010.

[64] W. Kast and H. Nirschl. Pressure Drop in Flow Through Pipes (L1.2). In VDI e. V., editor, *VDI Heat Atlas*, pages 1057–1064. Springer-Verlag, Berlin, Heidelberg, 2010.

[65] Y.-M. Kim, D.-G. Shin, S.-Y. Lee, and D. Favrat. Isothermal transcritical CO2 cycles with TES (thermal energy storage) for electricity storage. *Energy*, 49:484–501, Jan. 2013.

[66] M. Krüger, M. Schwarzenbart, and S. Zunft. Verfahrensentwicklung für dezentrale adiabate Druckluftspeicherkraftwerke (Mini-CAES). In *Thermodynamik-Kolloquium 2014*, Stuttgart, Sept. 2014.

[67] D. Laing. Wärmespeichertechnologien für Energieeffizienz in Industrieanwendungen. In *Energie Speicher Symposium*, Stuttgart, 2012.

[68] D. Laing, C. Bahl, T. Bauer, M. Fiss, N. Breidenbach, and M. Hempel. High-Temperature Solid-Media Thermal Energy Storage for Solar Thermal Power Plants. *Proceedings of the IEEE*, 100(2):516–524, Feb. 2012.

[69] D. Laing, C. Bahl, T. Bauer, D. Lehmann, and W.-D. Steinmann. Thermal energy storage for direct steam generation. *Solar Energy*, 85(4):627–633, Apr. 2011.

[70] D. Laing, T. Bauer, N. Breidenbach, B. Hachmann, and M. Johnson. Development of high temperature phase-change-material storages. *Applied Energy*, 109:497–504, Sept. 2013.

[71] D. Laing, T. Bauer, D. Lehmann, and C. Bahl. Development of a Thermal Energy Storage System for Parabolic Trough Power Plants With Direct Steam Generation. *Journal of Solar Energy Engineering*, 132(2):021011–021011, May 2010.

[72] D. Laing, T. Bauer, W.-D. Steinmann, and D. Lehmann. Advanced high temperature latent heat storage system - design and test results. In *11th International Conference on Thermal Energy Storage - EffStock*, Stockholm, June 2009.

[73] D. Laing, D. Lehmann, and C. Bahl. Concrete Storage for Solar Thermal Power Plants and Industrial Process Heat. In *Third International Renewable Energy Storage Conference (IRES 2008)*, Berlin, Nov. 2008.

[74] D. Laing, D. Lehmann, M. Fiß, and C. Bahl. Test Results of Concrete Thermal Energy Storage for Parabolic Trough Power Plants. *Journal of Solar Energy Engineering*, 131(4):0410071–0410076, Sept. 2009.

[75] D. Laing, W.-D. Steinmann, R. Tamme, and C. Richter. Solid media thermal storage for parabolic trough power plants. *Solar Energy*, 80(10):1283–1289, Oct. 2006.

[76] D. Laing, W. D. Steinmann, P. Viebahn, F. Gräter, and C. Bahl. Economic Analysis and Life Cycle Assessment of Concrete Thermal Energy Storage for Parabolic Trough Power Plants. *Journal of Solar Energy Engineering*, 132(4):041013–041013, Oct. 2010.

[77] D. Laing, R. Tamme, A. Wörner, W. Platzer, P. Schossig, and A. Hauer. Thermische Energiespeicher - Neueste Entwicklungen und Anwendungen. In *Jahrestagung 2012 des Forschungsverbunds Erneuerbare Energien*, Berlin, Deutschland, 2012.

[78] J. Lambauer, U. Fahl, M. Ohl, M. Blesl, and A. Voß. Industrielle Großwärmepumpen - Potenziale, Hemmnisse und Best-Practice Beispiele. Report, IER – Institut für Energiewirtschaft und Rationelle Energieanwendung, Stuttgart, 2008.

[79] C. Lechner and J. Seume, editors. *Stationäre Gasturbinen*. Springer, Berlin, Heidelberg, 2 edition, 2010.

[80] E. W. Lemmon, M. L. Huber, and M. O. McLinden. NIST Standard Reference Database 23: Reference Fluid Thermodynamic and Transport Properties-REFPROP. Version 9.1, National Institute of Standards and Technology, Standard Reference Data Program, Gaithersburg, 2013.

[81] Y. T. Li, D. J. Yan, Y. F. Guo, S. Q. Wang, and T. L. Deng. Studies on Magnesium Chloride Hexahydrate as Phase Change Materials. *Applied Mechanics and Materials*, 71-78:2598–2601, 2011.

[82] F. Marguerre. Ueber ein neues Verfahren zur Aufspeicherung elektrischer Energie. *Mitteilungen der Vereinigung der Elektrizitätswerke*, 354(55):27–35, 1924.

[83] F. Marguerre. Verfahren und Vorrichtung zur Aufspeicherung von Energie. German Patent DE388121a, Jan. 1924.

[84] F. Marguerre. Verfahren zur Aufspeicherung von Energie. German Patent DE388122a, Jan. 1924.

[85] R. Marquardt, P. Moser, C. Niklasch, P.-M. Mayer, S. Freund, M. Bieber, K. Götz, and J. Milleder. Adiabate Druckluftspeicher für die Elektrizitätsversorgung – Status des Projektes ADELE-ING –. In M. Beckmann and A. Hurtado, editors, *Kraftwerkstechnik - Sichere und nachhaltige Energieversorgung*, volume 5, pages 803–819. TK-Verlag, Neuruppin, 2013.

[86] C. Martin, T. Bauer, and H. Müller-Steinhagen. An experimental study of a non-eutectic mixture of KNO3 and NaNO3 with a melting range for thermal energy storage. *Applied Thermal Engineering*, 56(1–2):159–166, July 2013.

[87] J. D. McTigue, A. J. White, and C. N. Markides. Parametric studies and optimisation of pumped thermal electricity storage. *Applied Energy*, 137:800–811, Jan. 2015.

[88] A. Meier, C. Winkler, and D. Wuillemin. Experiment for modelling high temperature rock bed storage. *Solar Energy Materials*, 24(1):255–264, Dec. 1991.

[89] M. Mercangöz, J. Hemrle, L. Kaufmann, A. Z'Graggen, and C. Ohler. Electrothermal energy storage with transcritical CO2 cycles. *Energy*, 45(1):407–415, Sept. 2012.

[90] N. Mertens, F. Alobaid, L. Frigge, and B. Epple. Dynamic simulation of integrated rock-bed thermocline storage for concentrated solar power. *Solar Energy*, 110:830–842, Dec. 2014.

[91] Mobau Bauzentrum GmbH. Costs of basalt chips, 20-40mm. Website, https://www.kiesundco.de/garten/kies/glas-steinbrocken/1000kg-bigbag-gabionen-steine-basaltbruch-anthrazit-20-40mm/a-8865/, Mar. 2017.

[92] MOLBASE. Chemical B-2-B E-Commerce Platform. Website, http://www.molbase.com/, Apr. 2017.

[93] M. Morandin, S. Henchoz, and M. Mercangöz. Thermo-electrical energy storage: a new type of large scale energy storage based on thermodynamic cycles. In *World Engineers Convention*, Geneva, Switzerland, 2011.

[94] M. Morandin, F. Maréchal, M. Mercangöz, and F. Buchter. Conceptual design of a thermo-electrical energy storage system based on heat integration of thermodynamic cycles – Part A: Methodology and base case. *Energy*, 45(1):375–385, Sept. 2012.

[95] M. Morandin, F. Maréchal, M. Mercangöz, and F. Buchter. Conceptual design of a thermo-electrical energy storage system based on heat integration of thermodynamic cycles – Part B: Alternative system configurations. *Energy*, 45(1):386–396, Sept. 2012.

[96] M. Morandin, M. Mercangöz, J. Hemrle, F. Maréchal, and D. Favrat. Thermoeconomic design optimization of a thermo-electric energy storage system based on transcritical CO2 cycles. *Energy*, 58:571–587, Sept. 2013.

[97] D. R. Morris and F. R. Steward. Exergy analysis of a chemical metallurgical process. *Metallurgical and Materials Transactions B*, 15(4):645–654, Dec. 1984.

[98] M. D. Morris. Factorial Sampling Plans for Preliminary Computational Experiments. *Technometrics*, 33(2):161–174, May 1991.

[99] P. Moser. Status der Entwicklung des adiabaten Druckluftspeichers ADELE. In *Leopoldina-Symposium*, Halle, Feb. 2014.

[100] N-ERGIE Aktiengesellschaft. Wahrzeichen der Energiewende - Der Wärmespeicher der N-ERGIE. information flyer, N-ERGIE Aktiengesellschaft, Nürnberg, July 2015.

[101] M. Neubronner and T. Bodmer. Thermodynamic Properties of Pure Metals and Metal Alloys (D6.1). In VDI e. V., editor, *VDI Heat Atlas*, pages 551–565. Springer-Verlag, Berlin, Heidelberg, 2 edition, 2010. DOI: 10.1007/978-3-540-77877-6_26.

[102] U. Neupert, T. Euting, T. Kretschmer, C. Notthoff, K. Ruhlig, and B. Weimert. *Energiespeicher - Technische Grundlagen und energiewirtschaftliches Potenzial*. Fraunhofer IRB Verlag, Stuttgart, 2009.

[103] Next Kraftwerke GmbH. Day-Ahead-Handel - was ist das? Website, https://www.next-kraftwerke.de/wissen/strommarkt/day-ahead-handel, Dec. 2016.

[104] F. Ni and H. S. Caram. Analysis of pumped heat electricity storage process using exponential matrix solutions. *Applied Thermal Engineering*, 84:34–44, June 2015.

[105] K. Ochsner. *Wärmepumpen in der Heizungstechnik: Praxishandbuch für Installateure und Planer*. C. F. Müller, Heidelberg, 2007.

[106] T. Paanu, S. Niemi, and P. Rantanen. Waste Heat Recovery – Bottoming Cycle Alternatives. In *Proceedings of the University of Vaasa*, Vaasa, 2012.

[107] R. Pilar, L. Svoboda, P. Honcova, and L. Oravova. Study of magnesium chloride hexahydrate as heat storage material. *Thermochimica Acta*, 546:81–86, Oct. 2012.

[108] M. Platt, S. Exner, and R. Bracke. Analyse des deutschen Wärmepumpenmarktes, Bestandsaufnahme und Trends. Report, GeothermieZentrum Bochum, Bochum, 2010.

[109] W. H. Press, B. P. Flannery, S. A. Teukolsky, and W. T. Vetterling. *Numerical Recipes in Pascal: The Art of Scientific Computing*. Cambridge University Press, Cambridge, New York, 1 revised edition, 1989.

[110] W. H. Press, S. A. Teukolsky, W. T. Vetterling, and B. P. Flannery. *Numerical Recipes: The Art of Scientific Computing*. Cambridge University Press, Cambridge, New York, 3 edition, 2007.

[111] M. Profumo. *Exergoeconomic Analysis of Pumped Heat Electricity Storage Systems with Latent Heat Thermal Energy Storage*. Master Thesis, TU Darmstadt, July 2016.

[112] S. Quoilin, M. V. D. Broek, S. Declaye, P. Dewallef, and V. Lemort. Techno-economic survey of Organic Rankine Cycle (ORC) systems. *Renewable and Sustainable Energy Reviews*, 22:168–186, June 2013.

[113] S. Quoilin and V. Lemort. Technological and Economical Survey of Organic Rankine Cycle Systems. In *5th European Conference on Economics and Management of Energy in Industry*, Vilamoura, 2009.

[114] Z. Rant. Exergie, ein neues Wort für "technische Arbeitsfähigkeit". *Forschung auf dem Gebiet des Ingenieurwesens*, 22(1):33–37, Mar. 1956.

[115] H. Rietschel and K. Fitzner, editors. *Raumklimatechnik: Raumluft- und Raumkühltechnik*, volume 2. Springer, Berlin, 16 edition, 2008.

[116] F. Rockmann. Pläne zum Druckluftspeicher eingestellt. *Volksstimme Magdeburg*, Mar. 2015.

[117] A. Rudek. *Numerische Simulation und Exergieanalyse von Latentwärmespeichern*. Master Thesis, TU Darmstadt, Darmstadt, 2013.

[118] J. Ruer. Installation and method for storing and returning electrical energy. US Patent US8627665 B2, Saipem S.A., Jan. 2014.

[119] P. M. Rundel, R. Daschner, S. Binder, and A. Hornung. Schüttgutspeicher zur Effizienzsteigerung von Druckluftspeicherkraftwerken. In *13. Symposium Energieinnovation*, pages 1–9, Graz, Austria, Feb. 2014.

[120] P. M. Rundel, B. Meyer, M. Meiller, I. Meyer, R. Daschner, M. Jakuttis, M. Franke, S. Binder, and A. Hornung. Speicher für die Energiewende. Report, Fraunhofer-Institut für Umwelt-, Sicherheits- und Energietechnik UMSICHT, Sulzbach-Rosenberg, Sept. 2013.

[121] A. Saltelli, M. Ratto, T. Andres, F. Campolongo, J. Cariboni, D. Gatelli, M. Saisana, and S. Tarantola. *Global Sensitivity Analysis: The Primer*. Wiley, Chichester, 2008.

[122] A. Saltelli, S. Tarantola, F. Campolongo, and M. Ratto. *Sensitivity Analysis in Practice: A Guide to Assessing Scientific Models*. Wiley, Chichester, 2004.

[123] K. M. Sarma and G. M. Bankobeza, editors. *Montreal Protocol on Substances that Deplete the Ozone Layer*. Ozone Secretariat, United Nations Environment Programme, Nairobi, Kenya, 2000.

[124] A. Schuster, S. Karellas, and R. Aumann. Efficiency optimization potential in supercritical Organic Rankine Cycles. *Energy*, 35(2):1033–1039, Feb. 2010.

[125] E. Sciubba and G. Wall. A brief Commented History of Exergy From the Beginnings to 2004. *International Journal of Thermodynamics*, 10(1):1–26, Mar. 2007.

[126] A. Sharma, V. V. Tyagi, C. R. Chen, and D. Buddhi. Review on thermal energy storage with phase change materials and applications. *Renewable and Sustainable Energy Reviews*, 13(2):318–345, Feb. 2009.

[127] A. Shukla, D. Buddhi, and R. L. Sawhney. Thermal cycling test of few selected inorganic and organic phase change materials. *Renewable Energy*, 33(12):2606–2614, Dec. 2008.

[128] S. Sobotta. *Praxis Wärmepumpe: Technik, Planung, Installation*. Solarpraxis AG, Berlin, 2008.

[129] S. Solomon, D. Qin, and M. Manning, editors. *Climate Change 2007: The Physical Science Basis: Contribution of Working Group I to the Fourth Assessment Report of the Intergovernmental Panel on Climate Change*. Cambridge University Press, Cambridge ; New York, 2007.

[130] STEAG GmbH. EBSILON Professional. Process Simulation Software. Release 12.03, 2016.

[131] J. Stefan. Über einige Probleme der Theorie der Wärmeleitung. *Sitzungber., Wien, Akad. Mat. Natur*, 98:473–484, 1889.

[132] W. D. Steinmann. The CHEST (Compressed Heat Energy STorage) concept for facility scale thermo mechanical energy storage. *Energy*, 69:543–552, May 2014.

[133] W.-D. Steinmann. Thermo-mechanical concepts for bulk energy storage. *Renewable and Sustainable Energy Reviews*, 75:205–219, Aug. 2017.

[134] P. Stephan, K. Schaber, K. Stephan, and F. Mayinger. *Thermodynamik - Grundlagen und technische Anwendungen: Einstoffsysteme*, volume 1 of *Springer-Lehrbuch*. Springer-Verlag, Berlin, Heidelberg, 17 edition, 2006.

[135] K. Strauß. *Kraftwerkstechnik: zur Nutzung fossiler, nuklearer und regenerativer Energiequellen*. VDI. Springer, Berlin, 6 edition, 2013. OCLC: 823316579.

[136] J. Szargut. Anwendung der Exergie zur angenäherten wirtschaftlichen Optimierung. *Brennstoff Wärme Kraft - BWK*, 23(12):516 – 519, 1971.

[137] B. F. Tchanche, G. Lambrinos, A. Frangoudakis, and G. Papadakis. Low-grade heat conversion into power using organic Rankine cycles – A review of various applications. *Renewable and Sustainable Energy Reviews*, 15(8):3963–3979, Oct. 2011.

[138] B. F. Tchanche, G. Papadakis, G. Lambrinos, and A. Frangoudakis. Fluid selection for a low-temperature solar organic Rankine cycle. *Applied Thermal Engineering*, 29(11–12):2468–2476, Aug. 2009.

[139] A. Thess. Thermodynamic Efficiency of Pumped Heat Electricity Storage. *Physical Review Letters*, 111(11):110602, 2013.

[140] G. P. Towler and R. K. Sinnott. *Chemical Engineering Design: Principles, Practice, and Economics of Plant and Process Design*. Butterworth-Heinemann, Boston, MA, 2 edition, 2013.

[141] G. Tsatsaronis. Thermoeconomic analysis and optimization of energy systems. *Progress in Energy and Combustion Science*, 19(3):227–257, 1993.

[142] E. Tsotsas. Heat and Mass Transfer in Packed Beds with Fluid Flow (M7). In VDI e. V., editor, *VDI Heat Atlas*, pages 1327–1342. Springer-Verlag, Berlin, Heidelberg, 2 edition, 2010.

[143] E. Tsotsas. Thermal Conductivity of Packed Beds (D6.3). In VDI e. V., editor, *VDI Heat Atlas*, pages 570–580. Springer-Verlag, Berlin, Heidelberg, 2 edition, 2010.

[144] R. Turton, R. C. Bailie, W. B. Whiting, J. A. Shaeiwitz, and D. Bhattacharyya. *Analysis, synthesis, and design of chemical processes*. Pearson, Upper Saddle River, 4th edition, 2013.

[145] G. D. Ulrich. *A guide to chemical engineering process design and economics*. John Wiley & Sons, New York, 1984.

[146] A. Valero, M. A. Lozano, L. Serra, G. Tsatsaronis, J. Pisa, C. Frangopoulos, and M. R. von Spakovsky. CGAM problem: Definition and conventional solution. *Energy*, 19(3):279–286, Mar. 1994.

[147] J. P. van Buijtenen. The Tri-O-Gen organic Rankine cycle: development and perspectives. *Power Engineer: Journal of the IDGTE (The Institution of Diesel and Gas Turbine Engineers)*, 13(3):4–12, 2009.

[148] Verband deutscher Pfandbriefbanken. Annual percentage rate for mortgage loans in Germany from 1994 to 2016. Report, Mar. 2017.

[149] VERBRAUCHER INITIATIVE e.V. Informationen zu Lebensmittelzusatzstoffen. Website, http://www.zusatzstoffe-online.de, Apr. 2017.

[150] P. Verma, Varun, and S. K. Singal. Review of mathematical modeling on latent heat thermal energy storage systems using phase-change material. *Renewable and Sustainable Energy Reviews*, 12(4):999–1031, May 2008.

[151] J. Vivian, T. Morosuk, G. Manente, and A. Lazzaretto. Thermodynamic criteria to select working fluid and configuration of Organic Rankine Cycles for low to medium temperature heat sources. In *Proceedings of the 27th International Conference on Efficiency, Cost, Optimization, Simulation and Environmental Impact of Energy Systems*, pages 237.1 – 237.22, Turku, June 2014.

[152] Y. Wang, A. Amiri, and K. Vafai. An experimental investigation of the melting process in a rectangular enclosure. *International Journal of Heat and Mass Transfer*, 42:3659–3672, 1999.

[153] A. J. White. Thermodynamic analysis of the reverse Joule–Brayton cycle heat pump for domestic heating. *Applied Energy*, 86(11):2443–2450, Nov. 2009.

[154] A. J. White, G. Parks, and C. N. Markides. Thermodynamic analysis of pumped thermal electricity storage. *Applied Thermal Engineering*, 53(2):291–298, May 2013.

[155] J. Winterling. *Exergoökonomische Analyse eines Strom-Wärme-Strom-Speichersystems*. Master Thesis, TU Darmstadt, Apr. 2014.

[156] K.-E. Wirth. Pressure Drop in Fixed Beds (L1.6). In VDI e. V., editor, *VDI Heat Atlas*, pages 1106–1110. Springer-Verlag, Berlin, Heidelberg, 2 edition, 2010.

[157] R. Zahoransky, editor. *Energietechnik - Systeme zur Energieumwandlung*. Vieweg + Teubner, Wiesbaden, 5 edition, 2010.

[158] S. Zunft. Adiabatic CAES: The ADELE-ING project. In *SCCER Heat & Electricity Storage Symposium*, Villingen, Switzerland, May 2015.

[159] S. Zunft, M. Krüger, V. Dreißigacker, P.-M. Mayer, C. Niklasch, and C. Bertsch. Adiabate Druckluftspeicher für die Elektrizitätsversorgung – der ADELE-Wärmespeicher. In M. Beckmann and A. Hurtado, editors, *Kraftwerkstechnik - Sichere und nachhaltige Energieversorgung*, volume 4, pages 749–757. TK-Verlag, Neuruppin, 2012.

[160] S. Zunft, M. Krüger, R. Marquardt, F. Buschsieweke, P. Moser, M. Bieber, K. E. Colombo, C. Niklasch, P.-M. Mayer, M. Klafki, and A. Bannach. Adiabate Druckluftspeicher für die Elektrizitätsversorgung. In M. Beckmann and A. Hurtado, editors, *Kraftwerkstechnik - Sichere und nachhaltige Energieversorgung*, volume 3, pages 579–590. TK-Verlag, Neuruppin, 2011.

List of Figures

List of Tables

A Appendix

A.1 Coefficients and parameters of the packed bed sensible heat TES system

System 1

Table A.1: Heat transfer coefficients and model parameters of the packed bed sensible heat TES systems.

	operation mode	α_R in W (m^2 K)$^{-1}$	λ_M in W (m K)$^{-1}$	$\lambda_{M,still}$ in W (m K)$^{-1}$	Bi	α_M in W (m^2 K)$^{-1}$	$d_{i,M}$ in m	$d_{o,M} - d_{i,M}$ in mm
HT TES	HP	81.88	10.076	-	0.723	345.27	1354.863	21.084
	idle after HP	-	-	0.295	-	345.27	1354.863	21.084
	HE	80.21	9.842	-	0.708	334.29	1370.898	20.837
	idle after HE	-	-	0.292	-	334.29	1370.898	20.837
LT TES	HP	75.31	9.833	-	0.665	313.72	1371.476	20.828
	idle after HP	-	-	0.268	-	313.72	1371.476	20.828
	HE	74.90	9.636	-	0.661	308.87	1385.482	20.618
	idle after HE	-	-	0.270	-	308.87	1385.482	20.618

System 2

Table A.2: Heat transfer coefficients and model parameters of the packed bed sensible heat TES systems.

	operation mode	α_R in W (m^2 K)$^{-1}$	λ_M in W (m K)$^{-1}$	$\lambda_{M,still}$ in W (m K)$^{-1}$	Bi	α_M in W (m^2 K)$^{-1}$	$d_{i,M}$ in m	$d_{o,M} - d_{i,M}$ in mm
HT TES	HP	87.62	7.941	-	0.644	328.00	1831.407	15.598
	idle after HP	-	-	0.299	-	328.00	1831.407	15.598
	HE	82.69	7.440	-	0.608	299.64	1892.013	15.098
	idle after HE	-	-	0.290	-	299.64	1892.013	15.098
LT TES	HP	79.07	7.704	-	0.581	291.53	1859.364	15.363
	idle after HP	-	-	0.267	-	291.53	1859.364	15.363
	HE	78.11	7.296	-	0.574	280.26	1910.650	14.951
	idle after HE	-	-	0.273	-	280.26	1910.650	14.951

A.2 Thermodynamic states of the working fluid within Joule cycle PHES systems

System 1

Table A.3: Thermodynamic states of the working fluid within the PHES system at different heat pump and heat engine operation durations τ. The nomenclature of the states follows Figure 6.2 b).

		HP1	HP2	HP3	HP4	HE1	HE2	HE3	HE4	HE5
$\tau = 0\,\mathrm{h}$	T in °C	422.5	600.0	114.2	55.6	10.0	114.2	600.0	444.0	105.9
	h in kJ (kg)$^{-1}$	435.8	630.3	115.1	56.0	10.0	115.1	630.3	458.9	106.7
	p in bar	1.000	2.064	2.039	1.041	1.000	2.530	2.509	1.043	1.000
	s in kJ (kg K)$^{-1}$	7.740	7.781	6.928	6.956	6.817	6.866	7.725	7.761	7.111
	e in kJ (kg)$^{-1}$	164.4	347.3	73.5	6.6	0.0	91.1	363.2	181.6	13.4
$\tau = 1\,\mathrm{h}$	T in °C	437.2	600.0	114.2	60.6	10.0	114.2	600.0	444.0	78.8
	h in kJ (kg)$^{-1}$	451.7	630.3	115.1	61.0	10.0	115.1	630.3	458.9	79.3
	p in bar	1.000	1.945	1.915	1.048	1.000	2.530	2.509	1.043	1.000
	s in kJ (kg K)$^{-1}$	7.763	7.798	6.946	6.969	6.817	6.866	7.725	7.761	7.036
	e in kJ (kg)$^{-1}$	173.8	342.5	68.4	7.9	0.0	91.1	363.1	181.6	7.3
$\tau = 2\,\mathrm{h}$	T in °C	440.1	600.0	117.3	64.3	10.0	114.2	599.4	443.5	66.7
	h in kJ (kg)$^{-1}$	454.7	630.3	118.2	64.7	10.0	115.1	629.6	458.4	67.1
	p in bar	1.000	1.924	1.892	1.050	1.000	2.530	2.509	1.043	1.000
	s in kJ (kg K)$^{-1}$	7.767	7.801	6.958	6.979	6.817	6.866	7.724	7.760	7.000
	e in kJ (kg)$^{-1}$	175.7	341.6	68.3	8.7	0.0	91.1	362.7	181.2	5.0
$\tau = 3\,\mathrm{h}$	T in °C	422.1	600.0	143.2	78.0	10.0	114.2	593.1	437.8	67.3
	h in kJ (kg)$^{-1}$	435.3	630.3	144.5	80.5	10.0	115.1	622.6	452.3	67.7
	p in bar	1.000	2.075	2.048	1.044	1.000	2.534	2.513	1.044	1.000
	s in kJ (kg K)$^{-1}$	7.739	7.779	7.000	7.027	6.817	6.866	7.715	7.751	7.002
	e in kJ (kg)$^{-1}$	164.1	347.7	82.5	11.0	0.0	91.2	358.1	177.7	5.0
$\tau = 4\,\mathrm{h}$	T in °C	382.9	600.0	200.0	112.6	10.0	114.2	572.0	418.7	82.9
	h in kJ (kg)$^{-1}$	393.4	630.3	202.5	113.4	10.0	115.1	599.1	431.7	83.4
	p in bar	1.000	2.465	2.444	1.034	1.000	2.549	2.525	1.048	1.000
	s in kJ (kg K)$^{-1}$	7.677	7.730	7.080	7.119	6.817	6.864	7.687	7.721	7.047
	e in kJ (kg)$^{-1}$	139.7	361.7	118.0	17.9	0.0	91.7	342.8	165.8	8.1

Table A.4: Thermodynamic states of the working fluid within the PHES system at different heat pump and heat engine operation durations τ. The nomenclature of the states follows Figure 6.2 b).

		HP1	HP2	HP3	HP4	HE1	HE2	HE3	HE4	HE5
$\tau = 0\,\mathrm{h}$	T in °C	370.9	600.0	108.4	33.8	10.0	108.4	600.0	451.3	168.8
	h in kJ (kg)$^{-1}$	380.7	630.3	109.2	33.9	10.0	109.2	630.3	466.9	170.5
	p in bar	1.000	2.571	2.564	1.013	1.000	2.387	2.378	1.019	1.000
	s in kJ (kg K)$^{-1}$	7.658	7.718	6.847	6.894	6.817	6.868	7.740	7.778	7.267
	e in kJ (kg)$^{-1}$	132.6	365.1	90.6	2.0	0.0	84.8	358.8	184.6	33.1
$\tau = 1\,\mathrm{h}$	T in °C	431.5	600.0	108.4	51.3	10.0	108.4	600.0	451.3	100.6
	h in kJ (kg)$^{-1}$	445.4	630.3	109.2	51.6	10.0	109.2	630.3	466.9	101.3
	p in bar	1.000	1.993	1.979	1.025	1.000	2.387	2.378	1.019	1.000
	s in kJ (kg K)$^{-1}$	7.754	7.791	6.921	6.947	6.817	6.868	7.740	7.778	7.096
	e in kJ (kg)$^{-1}$	170.1	344.4	69.6	4.8	0.0	84.8	358.8	184.6	12.1
$\tau = 2\,\mathrm{h}$	T in °C	443.0	600.0	115.1	60.5	10.0	108.4	599.4	450.8	66.8
	h in kJ (kg)$^{-1}$	457.9	630.3	116.0	60.9	10.0	109.2	629.6	466.3	67.2
	p in bar	1.000	1.905	1.889	1.029	1.000	2.387	2.378	1.019	1.000
	s in kJ (kg K)$^{-1}$	7.771	7.804	6.952	6.974	6.817	6.868	7.739	7.778	7.001
	e in kJ (kg)$^{-1}$	177.6	340.8	67.6	6.4	0.0	84.8	358.4	184.2	5.1
$\tau = 3\,\mathrm{h}$	T in °C	384.1	600.0	193.7	105.9	10.0	108.4	585.0	437.6	66.1
	h in kJ (kg)$^{-1}$	394.7	630.3	196.0	106.7	10.0	109.2	613.5	452.1	66.5
	p in bar	1.000	2.453	2.443	1.019	1.000	2.394	2.385	1.020	1.000
	s in kJ (kg K)$^{-1}$	7.679	7.731	7.066	7.105	6.817	6.867	7.720	7.757	6.999
	e in kJ (kg)$^{-1}$	140.5	361.3	115.3	14.9	0.0	85.0	347.8	175.7	5.0
$\tau = 4\,\mathrm{h}$	T in °C	279.5	600.0	345.0	180.5	10.0	108.4	496.3	356.4	133.2
	h in kJ (kg)$^{-1}$	284.6	630.3	358.5	182.5	10.0	109.2	515.7	365.4	134.4
	p in bar	1.000	4.149	4.141	1.014	1.000	2.449	2.434	1.030	1.000
	s in kJ (kg K)$^{-1}$	7.497	7.580	7.215	7.289	6.817	6.860	7.594	7.625	7.181
	e in kJ (kg)$^{-1}$	82.0	404.0	235.8	38.6	0.0	86.9	285.7	126.5	21.1

Table A.5: Overview of organic working fluids considered during working fluid selection. Thermodynamic properties based on [80].

						$T = 100\,°C$				$T = 120\,°C$			
working fluid	type	T_{crit} in °C	p_{crit} in bar	T_{NB} in °C	T_{tr} in °C	Δh_v in kJ (kg)$^{-1}$	p in bar	ρ_l in kg m^{-3}	ρ_v in kg m^{-3}	Δh_v in kJ (kg)$^{-1}$	p in bar	ρ_l in kg m^{-3}	ρ_v in kg m^{-3}
methanol	wet	239.45	81.035	64.482	−97.54	1022.1	3.5373	710.95	4.0421	966.15	6.4081	687.29	7.2359
ethanol	wet	241.56	62.68	78.42	−114.15	810.92	2.2417	714.02	3.5214	768.09	4.273	690.78	6.5663
ammonia	wet	132.25	113.33	−33.327	−77.655	715.63	62.553	456.63	56.117	480.31	91.125	385.49	100.07
benzene	dry	288.87	49.073	80.069	5.524	378.54	1.8016	791.1	4.7804	362.51	3.0002	767.32	7.7357
toluene	dry	318.6	41.263	110.6	−95.15	367.57	0.742 46	789.93	2.2791	354.43	1.3137	769.4	3.892
cyclohexane	dry	280.45	40.805	80.715	6.32	342.84	1.7473	699.54	5.0166	327.9	2.8824	678.07	8.0532
octane	dry	296.17	24.97	125.62	−56.78	319.17	0.468 24	635.45	1.7816	306.03	0.864 23	617.43	3.178
heptane	dry	266.98	27.36	98.38	−90.6	315.71	1.0623	612.67	3.63	300.58	1.836	593.03	6.1182
hexane	dry	234.67	30.34	68.71	−95.32	309.7	2.4629	580.6	7.5214	291.35	3.9976	558.16	12.059
pentane	dry	196.55	33.7	36.06	−129.68	296.4	5.9265	537.42	16.247	271.14	9.0671	510	25.179
isopentane	dry	187.2	33.78	27.83	−160.5	274.78	7.2214	527.93	20.31	248.48	10.864	498.63	31.22
butane	dry	151.98	37.96	−0.49	−138.26	258.26	15.259	467.12	39.352	213.35	22.131	425.88	61.935
MM	dry	245.6	19.39	100.25	−68.22	193.48	1.0058	681.68	5.6435	182.37	1.7455	658.18	9.6023
R141b	dry	204.35	42.12	32.05	−103.47	184.82	6.773	1072.5	29.678	170.57	10.331	1020.9	45.443
MDM	dry	290.94	14.15	152.51	−85.95	174.74	0.199 74	736.87	1.5571	166.58	0.395 82	714.27	2.9735
MD2M	dry	326.25	12.27	194.36	−67.95	161.54	0.046 046	772.97	0.465 19	155.08	0.104 29	751.87	1.0078
isobutane	dry	134.66	36.29	−11.749	−159.42	211.03	19.865	429.64	56.697	150.2	28.366	371.96	94.741
R365mfc	dry	186.85	32.66	40.15	−34.15	154.04	5.8705	1075.5	33.202	139.35	9.2605	1014.4	53.43
R245ca	dry	174.42	39.407	25.262	−81.65	154.66	9.3079	1171.3	49.459	136.66	14.388	1096.3	79.295
R123	dry	183.68	36.618	27.823	−107.15	134.01	7.8553	1246.9	46.996	120.53	11.99	1174.4	73.471
R113	dry	214.06	33.922	47.585	−36.22	125.41	4.3664	1368.7	29.86	116.61	6.8074	1308	46.471
R245fa	dry	154.01	36.51	15.14	−102.1	134.48	12.646	1093.3	72.777	111.77	19.275	999.17	119.53
HFE-7000	dry	164.55	24.762	34.199	−23.15	100.78	6.822	1162.3	55.913	86.738	10.597	1074.1	91.731
R236ea	dry	139.29	34.2	6.172	−103.15	102.32	15.748	1125.2	110.87	76.996	23.693	991.64	190.82
R114	dry	145.68	32.57	3.591	−92.52	88.133	14.197	1170.3	109.12	69.904	20.8	1051.9	177.49
novec 649	dry	168.66	18.69	49.052	−108.15	70.38	4.4729	1338.9	55.842	61.314	7.1165	1245.6	92.785
R236fa	dry	124.92	32	−1.49	−93.55	83.597	19.358	1016.2	153.61	43.57	28.974	803.08	312.74

Table A.5 (continued): Overview of organic working fluids considered during working fluid selection. Thermodynamic properties based on [80].

						$T = 100\,°C$				$T = 120\,°C$			
working fluid	type	T_{crit} in °C	p_{crit} in bar	T_{NB} in °C	T_{tr} in °C	Δh_v in kJ (kg)$^{-1}$	p in bar	ρ_l in kg m^{-3}	ρ_v in kg m^{-3}	Δh_v in kJ (kg)$^{-1}$	p in bar	ρ_l in kg m^{-3}	ρ_v in kg m^{-3}
R152a	wet	113.26	45.168	−24.023	−118.59	132.69	35.05	618.54	145.75	-	-	-	-
R1234ze	dry	109.36	36.349	−18.973	−104.53	70.358	30.26	777.25	225.01	-	-	-	-
R12	wet	111.97	41.361	−29.752	−157.05	64.019	33.399	903.78	252.58	-	-	-	-
RC318	dry	115.23	27.775	−5.975	−39.8	51.533	20.514	1059.6	234.35	-	-	-	-
R134a	wet	101.06	40.593	−26.074	−103.3	34.385	39.724	651.18	373.01	-	-	-	-
R227ea	dry	101.75	29.25	−16.34	−126.8	26.802	28.216	786.76	397.24	-	-	-	-
propane	wet	96.74	42.512	−42.114	−187.63	-	-	-	-	-	-	-	-
R1234yf	dry	94.7	33.822	−29.45	−53.15	-	-	-	-	-	-	-	-
R407C	wet	86.195	46.317	−43.63	−73.15	-	-	-	-	-	-	-	-
R32	wet	78.105	57.82	−51.651	−136.81	-	-	-	-	-	-	-	-
R125	wet	66.023	36.177	−48.09	−100.63	-	-	-	-	-	-	-	-

Publications

Peer-reviewed journal and conference contributions

A. Dietrich, F. Dammel, P. Stephan. *Exergoeconomic Analysis of a Pumped Heat Electricity Storage System with Concrete Thermal Energy Storage*. International Journal of Thermodynamics. 19(1):43–51. 2016.

A. Dietrich, F. Dammel, P. Stephan. *Exergoeconomic Analysis of a Pumped Heat Electricity Storage System with Concrete Thermal Energy Storage*. 28th International Conference on Efficiency, Cost, Optimization, Simulation and Environmental Impact of Energy Systems. France. June 30 - July 3, 2015.

A. Dietrich, F. Dammel, P. Stephan. *A Statistical Costing Approach for Exergoeconomic Analyses Applied to a Heat Pump*. 3rd International Exergy, Life Cycle Assessment, and Sustainability Workshop & Symposium. Greece. July 7 - 9, 2013.

Non-peer-reviewed conference contributions

A. Dietrich, C. Fraunholz, F. Dammel, P. Stephan. *Exergoeconomic Analysis of Concepts for Pumped Heat Electricity Storage Systems*. Joint Conference on Thermal Energy Storage – Perspectives and Applications in an Industrial Environment. Frankfurt am Main. May 3, 2016.

D. Hering, F. Dammel, A. Dietrich, P. Stephan. *Numerische Simulation eines Latentwärmespeichers für ein Strom-Wärme-Strom Speichersystem*. Thermodynamik-Kolloquium. Bochum. October 5 - 7, 2015.

A. Dietrich, J. Winterling, F. Dammel, P. Stephan. *Modeling and Analysis of Pumped-Heat-Electricity-Storage Systems using EBSILON Professional*. EBSILON User Conference. Wiesbaden. September 29 - 30, 2014.

A. Dietrich, J. Winterling, F. Dammel, P. Stephan. *Exergoeconomic Analysis of Concepts for Pumped-Heat-Electricity-Storage Systems*. Thermodynamik-Kolloquium. Stuttgart. September 22 - 24, 2014.

A. Dietrich, F. Dammel, P. Stephan. *Ein statistischer Kostenansatz zur exergoökonomischen Analyse von Energiewandlungssystemen*. Thermodynamik-Kolloquium. Hamburg. October 7 - 9, 2013.

Curriculum Vitae

Persönliches

Axel Dietrich

geboren am 26. April 1986

in Berlin

Berufliche Tätigkeit

seit 2011	Wissenschaftlicher Mitarbeiter am Institut für Technische Thermodynamik, TU Darmstadt

Akademische Ausbildung

2009 - 2011	Masterstudium Maschinenbau, TU Darmstadt
2008 - 2009	Bachelorstudium Maschinenbau, Virginia Polytechnic Institute and State University
2006 - 2008	Bachelorstudium Maschinenbau, TU Darmstadt

Schulische Ausbildung

1999 - 2006	Theodor-Fontane-Gymnasium Strausberg
1998 - 1999	Stadtschule Altlandsberg, Gundschulteil
1993 - 1998	20. Grundschule Berlin Marzahn